Politecnico di Milano
Scuola di Ingegneria Industriale e dell'Informazione
Corso di Laurea Magistrale in Ingegneria Aeronautica

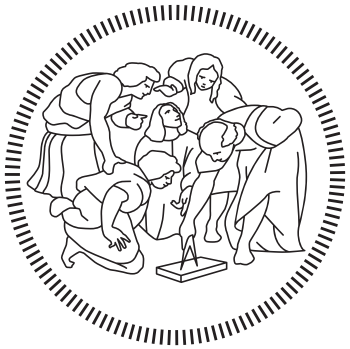

Aerodynamics, propulsion and testing of an eVTOL drone

Advisor: Prof. Marco LOVERA
Co-Advisor: Eng. Nicolò BATTAINI
Eng. Elia MARTINELLI

Thesis by:
Karim BARA Matr. 966354

Academic Year 2022–2023

Alle Donne della mia famiglia.

Acknowledgments

Abstract

Unmanned Aerial Vehicles (UAVs) have drawn increasing attention due to their diverse applications and economic benefits. Ranging from infrastructure monitoring to law enforcement, their utility is vast. A recent development is the rise of electric Vertical Take-Off and Landing (eVTOL) UAVs, merging vertical agility with the efficiency and endurance of fixed-wing aircraft. As UAV research progresses, the limitations of traditional configurations become apparent: while multirotors struggle with flight endurance, fixed-wing UAVs lack vertical take-off capabilities. The solution lies in VTOL UAVs, seamlessly integrating vertical and horizontal capabilities, making them ideal for applications like parcel delivery, aerial mapping, and reconnaissance.

The purpose of the thesis is to upgrade the hardware, then conduct a comprehensive flight test campaign on an electric VTOL (eVTOL) designed and built in three previous master theses within the *Aerospace Systems and Control Laboratory* (ASCL) of *Politecnico di Milano*. Specifically, in [1] the drone has been designed, in [2] it has been built and integrated, and finally in [3] a custom controller has been developed, installed and tested indoor. The resulting vehicle features both vertical and forward flight, has an approximate take-off mass of 6 kg, and with its wide 2.25 m wingspan it is expected to have an endurance of about 100 minutes. Being the first one ever to be completely designed and produced within the *Department of Aerospace Science and Technology* (DAER), and being its first outdoor flight test campaign, this experimental activity posed countless stimulating challenges and as many opportunities to learn and improve.

During the flight test campaign, the progressive encountering of aerodynamic, structural and propulsive limitations encouraged the upgrade to various parts of the aircraft. First, the wing and tail have been redesigned, increasing their size and improving the manufacturing technique to include a glass-fiber cladding which provided significantly enhanced structural stiffness. Then, the forward flight propellers have been changed with a better performing model which underwent also wind tunnel tests to obtain an accurate in-flight thrust estimation model. Finally the aircraft has been tested; the transition and backtransition phases have been progressively tuned and validated, and the fixed-wing portion of flight has been explored yielding to key performance such as stall speed, specific excess power curve and drag polar. The findings from this work constitute a foundation

for further testing, and provide several insight on key improvements for future development of the eVTOL project.

Sommario

Gli aeromobili a pilotaggio remoto (APR, o UAV - *Unmanned Aerial Vehicles* - in inglese) hanno attirato sempre più attenzione grazie ai numerosi casi applicativi e vantaggi economici. Dal monitoraggio delle infrastrutture al supporto alle forze dell'ordine, la loro utilità è vasta. Uno sviluppo recente è la diffusione degli UAV elettrici a decollo e atterraggio verticale (eVTOL - dall'inglese *electrical Vertical Take-Off and Landing*), che uniscono la flessibilità del volo verticale con l'efficienza e l'autonomia degli aerei ad ala fissa. Con il progredire della ricerca sugli UAV, i limiti delle configurazioni tradizionali diventano sempre più evidenti. Mentre i multirotori hanno limitazioni sull'autonomia e quindi sulle distanze percorribili, gli UAV ad ala fissa non hanno i vantaggi del decollo verticale. La soluzione risiede negli UAV VTOL, che integrano perfettamente capacità verticali e orizzontali, rendendoli ideali per applicazioni come consegne a lunga distanza, mappature aeree e ricognizione.

L'obiettivo principale di questa tesi è quello di condurre una campagna completa di prove di volo su un VTOL elettrico (eVTOL) progettato e interamente costruito durante tre precedenti tesi magistrali all'interno dell'*Aerospace Systems and Control Laboratory* (ASCL) del *Politecnico di Milano*. Nello specifico, in [1] il drone è stato progettato, in [2] è stato costruito e integrato e infine in [3] è stato sviluppato un sistema di controllo, poi installato a bordo e testato all'interno del laboratorio. Il velivolo risultante è in grado di volare sia verticalmente come multirotore che in volo avanzato come ala fissa, ha una massa al decollo di circa 6 kg e con la sua ampia apertura alare di 2,25 m ha un'autonomia stimata di circa 100 minuti. Essendo il primo in assoluto ad essere completamente progettato e costruito all'interno del *Dipartimento di Scienza e Tecnologia Aerospaziale* (DAER), ed essendo la prima campagna di prove di volo all'aperto a cui è sottoposto, questa attività sperimentale ha presentato innumerevoli stimolanti sfide e altrettante opportunità di apprendere e migliorare.

Durante la campagna di prove di volo, il progressivo incontro con limitazioni aerodinamiche, strutturali e propulsive ha spinto all'aggiornamento di varie parti del velivolo. Innanzitutto, l'ala e la coda sono state riprogettate, aumentandone le dimensioni e migliorandone la tecnica produttiva, includendo un rivestimento in fibra di vetro che ha portato migliori caratteristiche strutturali. Successivamente, le eliche per il volo avanzato sono state sostituite con un modello dalle prestazioni

migliori che è stato sottoposto anche a test in galleria del vento per ottenere un modello di stima della spinta accurato. Infine il velivolo è stato testato: le fasi di transizione in avanti e all'indietro sono state progressivamente messe a punto e validate; la fase di volo in ala fissa è stata poi studiata ottenendo prestazioni fondamentali come la velocità di stallo, la curva di eccesso di potenza specifica e la curva polare. I risultati di questo lavoro costituiscono una base per ulteriori prove e forniscono numerosi spunti per miglioramenti durante lo sviluppo futuro del progetto eVTOL.

Contents

List of Figures

List of Tables

Introduction

Unmanned Aerial Vehicles (UAVs) have witnessed significant advancements in recent years, challenging the conventional perception associated with drones. The typical image of a small and inexpensive quad-rotor, often associated with entertainment purposes, no longer encapsulates the full spectrum of UAVs. This spectrum extends from small pocket-sized drones, exemplified by the DJI Mavic Mini 2 (Figure 1a), to large-scale vehicles like the Piaggio P1.HH Hammerhead (Figure 1b). Given the broad applicability of these aircraft in both civil and military sectors, addressing the limitations of short flight times in multicopters and the spatial requirements for take-off and landing in fixed-wing UAVs became imperative.

The Vertical Take-Off and Landing (VTOL) configuration has emerged as a solution to bridge the capabilities of both multicopters and fixed-wing UAVs. This innovative design eliminates the need for runways, allowing for vertical take-off and landing while also providing the efficiency of covering extensive distances with wings.

The potential applications of fixed-wing VTOL UAVs are vast and diverse, encompassing areas such as infrastructure monitoring, agriculture, environmental protection, emergency response, police operations, and logistics. This versatile design opens up new possibilities for UAV utilization across various sectors.

(a) DJI Mavic Mini 2 (source [11]) (b) Piaggio P.1HH Hammehead (source [12])

Figure 1: Different categories and scales of UAVs

Background

This thesis constitutes the fourth phase of a project dedicated to the development of an electric Vertical Take-Off and Landing (eVTOL) Unmanned Aerial Vehicle (UAV) designed and built at the *Politecnico di Milano, Department of Aerospace Science and Technology* (DAER). The initial conceptual and preliminary design, starting from the basic requirements, is detailed in [1]. The subsequent stages involved the production and integration of components, including the development of a simulator, as outlined in [2]. Finally, a custom control system was designed in Simulink, installed onboard, and tested within the controlled environment of the *Aerospace System and Control Laboratory* (ASCL) by [3]. This current work builds upon the foundation laid in the preceding theses. The aircraft under consideration is an electric Vertical Takeoff and Landing (eVTOL) with a maximum take-off mass (MTOM) of 6.4 kg. The multirotor phase of the aircraft has undergone extensive indoor testing, utilizing both the stock PX4 controller and a custom controller developed in Simulink ([3]). Figure 2 illustrates the aircraft at the beginning of this work.

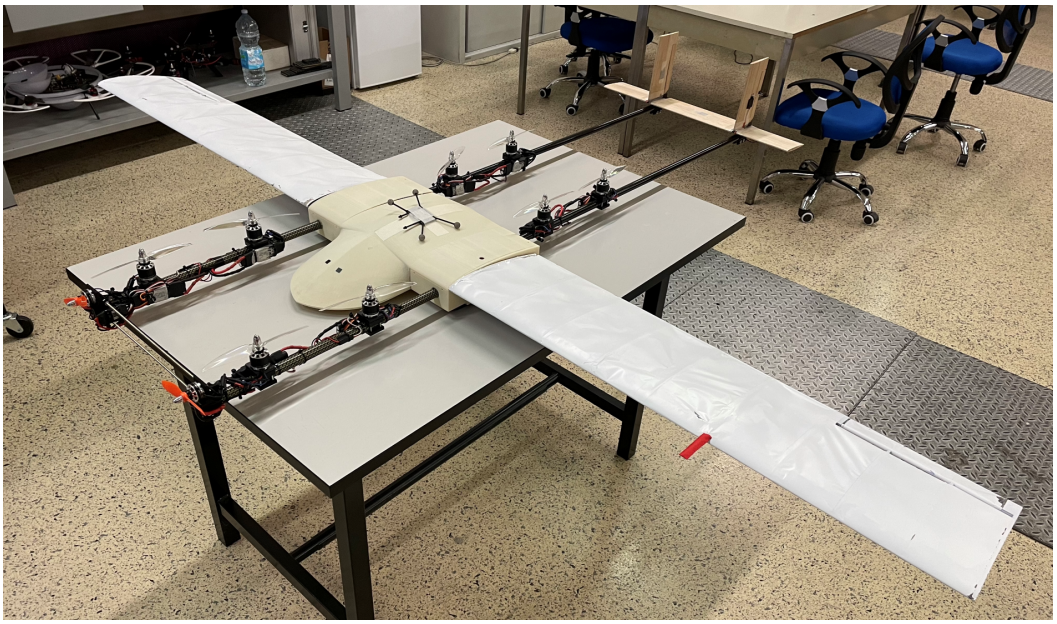

Figure 2: eVTOL UAV developed at *Politecnico di Milano* (source [3])

Thesis objectives

The primary objective of this thesis is to conduct a comprehensive flight test campaign on the studied eVTOL drone. The goal is to extract key performance metrics for comparison with the original design, as well as with simulation and

numerical results obtained in prior research. Additionally, the aim is to gather valuable insights into the behavior and characteristics of the drone, providing essential groundwork for future design developments.
To accomplish this objective, it was essential to address several limitations identified in the previous theses and encountered during testing. This involved enriching the process through hardware modifications, upgrades, incident investigations, and conducting experiments of a nature different from actual flight tests. These ventures contribute to a more thorough understanding of the eVTOL drone's capabilities and limitations, enhancing the overall quality of the flight test campaign.

Structure of the thesis

The thesis is organized as follows:

- Chapter 1 presents an overview of the conventions, notation, and the model describing the dynamics of a VTOL drone. It introduces the flight test campaign, discusses the airfield location, and outlines the procedures involved in organizing and executing a flight test day. Additionally, the chapter delves into the onboard instrumentation, providing details on the sources of key quantities and their filtering process.

- Chapter 2 discusses in detail the aerodynamic and aeroelastic limitations encountered during the flight test campaign. To address these challenges, the wing and tail underwent a resizing process, accompanied by a redesign that transitioned the structure from a carbon fiber spar, 3D printed ribs, and Mylar outer skin to a carbon fiber spar with hot-wire-cut foam wing. The redesign was further enhanced by incorporating a glass-fiber cladding to the wing, leading to a significant improvement in torsional stiffness and aerodynamic characteristics. Structural tests performed in the laboratory validated these enhancements.

- Chapter 3 is dedicated to the progressive upgrades made to the propulsive system, focusing specifically on the forward flight propellers, which underwent two substitutions during the flight test campaign. Alongside these substitutions, wind tunnel tests were conducted, contributing to the development of thrust estimation model for both forward and vertical flight motors and propellers.

- Chapter 4 analyzes the multirotor flight mode tests, starting with the investigation of a parameter for rejecting external disturbances to hover position accuracy and endurance. It then delves into the complex dynamics of the forward transition phase, examining the behavior of the aircraft and performance metrics. The chapter concludes with an analysis of the backtransition phase, tracing its evolution from the early stages to the end of the campaign.

- Chapter 5 is focused on the fixed-wing part of the tests and covers fundamental performance aspects such as stall speed, drag polar, associated parasitic drag coefficient, and maximum airspeed. Given the challenges in stabilizing the aircraft within the limited airspace available, the chapter provides insights into corrections applied to different data-processing methods to enhance the obtained results.

Chapter 1

VTOL: hardware and software

In this Chapter, a comprehensive overview regarding the conventions, notation, and the model that governs the dynamics of a VTOL drone is provided. Additionally, attention is directed towards the essential element of the flight test campaign and the accompanying onboard instrumentation.
The opening section presents the employed reference frames, establishing a framework for subsequent discussions. Following this, the second section discusses the rotation formalism used to orient vectors across distinct reference frames. The third section outlines the dynamic equations governing the VTOL, covering both kinematic and dynamic aspects.
Transitioning to the fourth section, insights are provided into the flight test campaign, including details about the setup and the instrumentation employed for data collection. Lastly, the final section analyzes the various flight control modes employed throughout the testing phase.

1.1 Reference frames

In describing the motion of an aircraft, it is crucial to establish reference frames to derive the equations of motion. Considering that the UAV operates near the ground, both indoors and outdoors, the Earth is assumed to be flat and non-rotating. The reference frames outlined below are illustrated in Figure 1.1.

Navigation frame $\overline{\mathcal{N}}$

The navigation frame has origin in a generic point O_N on Earth's surface, usually aligned with the aircraft's position. The first unit vector $\overline{\mathbf{n}}_\mathbf{1}$ is directed towards the local North pole, $\overline{\mathbf{n}}_\mathbf{2}$ points towards the local East and $\overline{\mathbf{n}}_\mathbf{3}$ is aligned with the gravity vector, pointing downward. With the hypothesis of flat and non-rotating Earth, the $\overline{\mathcal{N}}$ frame can be considered as an inertial frame.

Local vertical reference frame (NED) $\mathcal{N}$

The local vertical reference frame, also referred to as NED (North-East-Down), has its origin at the aircraft's center of gravity. In this frame, $\mathbf{n_1}$ denotes the direction towards the local North pole, $\mathbf{n_2}$ aligns with the local East, and $\mathbf{n_3}$ points towards the center of the Earth.

Body frame $\mathcal{B}$

The body frame has origin in the centre of gravity of the aircraft and rotates in conjunction with it. Within this frame, the unit vector $\mathbf{b_1}$ lies in the plane of symmetry of the aircraft and points towards the nose, $\mathbf{b_2}$ is normal to the plane of symmetry and points to the right-hand side wingtip, and $\mathbf{b_3}$ points downward.

Stability frame $\mathcal{S}$

The stability frame has origin in the centre of gravity of the aircraft; its first unit vector $\mathbf{s_1}$ points forward, towards the nose of the aircraft, and is aligned with the projection of the relative wind velocity in the plane of symmetry of the aircraft; $\mathbf{s_2}$ is aligned with $\mathbf{b_2}$ and $\mathbf{s_3}$ forms a right-hand triad with $\mathbf{s_1}$ and $\mathbf{s_2}$.

Wind frame $\mathcal{W}$

The wind frame has origin in the centre of gravity of the aircraft. The unit vector $\mathbf{w_1}$ is aligned with the relative wind speed, with a positive verse in the direction of motion, $\mathbf{w_3}$ lies within the aircraft's longitudinal plane of symmetry and is perpendicular to $\mathbf{w_1}$, pointing downwards; $\mathbf{w_2}$ forms a right-hand triad with $\mathbf{w_1}$ and $\mathbf{w_3}$.

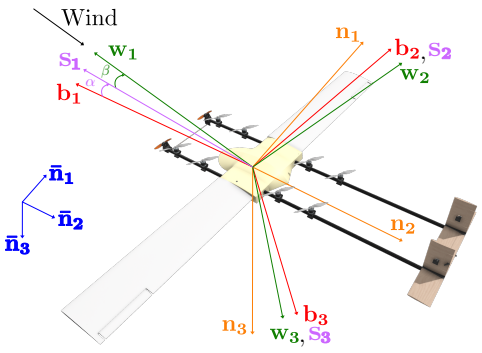

Figure 1.1: Reference frames

1.2 Rotation formalism

Euler angles

Euler angles, denoted as roll (ϕ), pitch (θ), and yaw (ψ), are three independent angular parameters used to characterize the 3D orientation of an object. These angles are defined with respect to two sets of reference frames: an inertial Earth-fixed frame and a body frame rigidly attached to the object. The Euler angles facilitate the transformation of vector components between these frames. Given a vector v_A in the initial reference frame A, its rotation into the reference frame B is achieved using the rotation matrix R_A^B, as expressed by the equation:

$$v_B = R_A^B v_A \,. \tag{1.1}$$

Any arbitrary attitude is achieved through a sequential application of three rotations around each axis of an orthogonal frame. The rotation around the x-axis is represented by the matrix $R_x(\phi)$:

$$R_x(\phi) = \begin{bmatrix} 1 & 0 & 0 \\ 0 & \cos\phi & \sin\phi \\ 0 & -\sin\phi & \cos\phi \end{bmatrix} . \tag{1.2}$$

Similarly, rotations around the y and z axes are described by matrices $R_y(\theta)$ and $R_z(\psi)$:

$$R_y(\theta) = \begin{bmatrix} \cos\theta & 0 & -\sin\theta \\ 0 & 1 & 0 \\ \sin\theta & 0 & \cos\theta \end{bmatrix} , \tag{1.3}$$

$$R_z(\psi) = \begin{bmatrix} \cos\psi & \sin\psi & 0 \\ -\sin\psi & \cos\psi & 0 \\ 0 & 0 & 1 \end{bmatrix} . \tag{1.4}$$

In aircraft dynamics, the generic attitude of the vehicle is described using the so-called rotation sequence 321: the attitude of the body axes $\mathcal{B}$ (always aligned with the aircraft) with respect to a non-rotating NED $\mathcal{N}$ reference frame, is obtained by a first rotation about the z-axis of an angle ψ, then a rotation about the y-axis of an angle θ, and finally a rotation about the x-axes of an angle ϕ. The final rotation matrix from $\mathcal{N}$ to $\mathcal{B}$ is obtained by the ordered multiplication of the previous rotation matrices; it is called Euler rotation matrix and is defined as follows:

$$T_N^B(\phi,\theta,\psi) = \begin{bmatrix} C_\theta C_\psi & C_\theta S_\psi & -S_\theta \\ S_\phi S_\theta C_\psi - C_\phi S_\psi & S_\phi S_\theta S_\psi + C_\phi C_\psi & S_\phi C_\theta \\ C_\phi S_\theta C_\psi + S_\phi S_\psi & C_\phi S_\theta S_\psi - S_\phi C_\psi & C_\phi C_\theta \end{bmatrix} , \tag{1.5}$$

where, $C_\alpha = \cos(\alpha)$ and $S_\alpha = \sin(\alpha)$ for brevity. The roll angle (ϕ), pitch angle (θ), and yaw angle (ψ) collectively form the Euler angles vector (α_e), providing

a unique representation of the aircraft's orientation in space with respect to the NED reference frame ($\mathcal{N}$):

$$\alpha_e = \begin{bmatrix} \phi \\ \theta \\ \psi \end{bmatrix} . \tag{1.6}$$

The angular rates measured in body frame ω_B are the roll rate p, pitch rate q and yaw rate r:

$$\omega_B = \begin{bmatrix} p \\ q \\ r \end{bmatrix} . \tag{1.7}$$

The rate of change of Euler angles is related to the angular velocity in the body frame by the following equation:

$$\dot{\alpha_e} = E^{-1}\omega_B \, , \tag{1.8}$$

where E^{-1} is the inverse of matrix E, whose expressions are given by:

$$E(\phi,\theta) = \begin{bmatrix} 1 & 0 & -\sin\theta \\ 0 & \cos\phi & \cos\theta\sin\phi \\ 0 & -\sin\phi & \cos\theta\cos\phi \end{bmatrix} , E^{-1}(\phi,\theta) = \begin{bmatrix} 1 & \sin\phi\tan\theta & \cos\phi\tan\theta \\ 0 & \cos\phi & -\sin\phi \\ 0 & \sin\phi/\cos\theta & \cos\phi/\cos\theta \end{bmatrix} . \tag{1.9}$$

It can be seen that matrix E^{-1} is singular for pitch angles of $\pm 90°$; this singularity is the so-called gimbal lock and can be avoided with the employment of quaternions.

Quaternions

Quaternions, denoted as q, provide a parameterization of the four-dimensional unit sphere and serve as a representation for the orientation of a rigid body or coordinate frame in three-dimensional space ([13]). The quaternion is defined as:

$$q = \begin{bmatrix} q_0 \\ q_1 \\ q_2 \\ q_3 \end{bmatrix} , \quad ||q|| = 1 \, . \tag{1.10}$$

The quaternion elements generate a rotation matrix, analogous to the one expressed in Equation (1.5) in terms of Euler angles:

$$T_N^B = \begin{bmatrix} q_0^2+q_1^2-q_2^2-q_3^2 & 2(q_1q_2+q_0q_3) & 2(q_1q_3-q_0q_2) \\ 2(q_1q_2-q_0q_3) & q_0^2-q_1^2+q_2^2-q_3^2 & 2(q_2q_3+q_0q_1) \\ 2(q_1q_3+q_0q_2) & 2(q_2q_3-q_0q_1) & q_0^2-q_1^2-q_2^2+q_3^2 \end{bmatrix} . \tag{1.11}$$

The Euler angles ϕ, θ, and ψ can be derived from the quaternion elements expressing the aircraft's orientation with respect to a non-rotating frame through the following equations:

$$\begin{aligned} \phi &= \tan^{-1}\left(\frac{2q_3q_4 - 2q_1q_2}{2q_1^2 - 1 + 2q_4^2}\right), \\ \theta &= -\sin^{-1}\left(2q_2q_4 + 2q_1q_3\right), \\ \psi &= \tan^{-1}\left(\frac{2q_2q_3 - 2q_1q_4}{2q_1^2 - 1 + 2q_2^2}\right). \end{aligned} \tag{1.12}$$

The quaternion conjugate, denoted by $(\cdot)^*$, swaps the frames described by an orientation. For example, the orientation of frame B with respect to frame A is represented by the quaternion q_{AB}, and its conjugate q_{AB}^* describes the orientation of frame A relative to frame B (q_{BA}) through the equation:

$$q_{AB}^* = q_{BA} = \begin{bmatrix} q_0 \\ -q_1 \\ -q_2 \\ -q_3 \end{bmatrix}. \tag{1.13}$$

The quaternion product, denoted as $(\otimes)$, describes successive rotations and is determined using the Hamilton rule, as expressed in equation (1.14). The quaternion product is not commutative.

$$q_{AC} = q_{BC} \otimes q_{AB} = \begin{bmatrix} a_0 \\ a_1 \\ a_2 \\ a_3 \end{bmatrix} \otimes \begin{bmatrix} b_0 \\ b_1 \\ b_2 \\ b_3 \end{bmatrix} = \begin{bmatrix} a_1b_1 - a_2b_2 - a_3b_3 - a_4b_4 \\ a_1b_2 + a_2b_1 + a_3b_4 - a_4b_3 \\ a_1b_3 - a_2b_4 + a_3b_1 + a_4b_2 \\ a_1b_4 + a_2b_3 - a_3b_2 + a_4b_1 \end{bmatrix}. \tag{1.14}$$

A three-dimensional vector can be rotated by a quaternion using Equation (1.15) by appending a zero as the first element of the vector to make it dimensionally consistent with quaternions:

$$v_B = q_{AB} \otimes v_A \otimes q_{AB}^* \ , \tag{1.15}$$

where v_A and v_B are the same vector described in frame A and frame B, respectively..

Finally, the quaternion derivative describing the rate of change of orientation of the Earth frame relative to the body frame can be calculated by the equation:

$$\dot{q}_{BE} = \frac{1}{2} q_{BE} \otimes \omega \quad \text{where} \ \ \omega = \begin{bmatrix} 0 \\ \omega_B \end{bmatrix}. \tag{1.16}$$

Resolving equation (1.16) leads to

$$\begin{bmatrix} \dot{q}_1 \\ \dot{q}_2 \\ \dot{q}_3 \\ \dot{q}_4 \end{bmatrix} = \frac{1}{2} \begin{bmatrix} 0 & -p & -q & -r \\ p & 0 & r & -q \\ q & -r & 0 & p \\ r & q & -p & 0 \end{bmatrix} \begin{bmatrix} q_1 \\ q_2 \\ q_3 \\ q_4 \end{bmatrix}. \tag{1.17}$$

1.3 Flight dynamics equations

1.3.1 Kinematic equations

In the context of a generic inertial frame $\mathcal{I}$ and the non-inertial body frame $\mathcal{B}$, with the convention that the velocity (or acceleration) of a point P with respect to a frame $\mathcal{I}$ is denoted as $v_{P/\mathcal{I}}$, the velocity of a generic point Q belonging to the aircraft, measured with respect to the inertial frame $\mathcal{I}$, can be expressed as:

$$v_{Q/\mathcal{I}} = v_{P/\mathcal{I}} + \boldsymbol{\omega}_{\mathcal{B}/\mathcal{I}} \times r_{PQ}\,, \tag{1.18}$$

where point P is another generic point belonging to the aircraft, and r_{PQ} is the vector between points P and Q.
The acceleration of point Q measured in the inertial frame $\mathcal{I}$ is found by computing the derivative of Equation (1.18) with respect to time:

$$a_{Q/\mathcal{I}} = \frac{^{\mathcal{I}}\mathrm{d}v_{Q/\mathcal{I}}}{\mathrm{d}t} = \frac{^{\mathcal{I}}\mathrm{d}v_{P/\mathcal{I}}}{\mathrm{d}t} + \frac{^{\mathcal{I}}\mathrm{d}\boldsymbol{\omega}_{\mathcal{B}/\mathcal{I}}}{\mathrm{d}t} \times r_{PQ} + \boldsymbol{\omega}_{\mathcal{B}/\mathcal{I}} \times \frac{^{\mathcal{I}}\mathrm{d}r_{PQ}}{\mathrm{d}t}\,, \tag{1.19}$$

where $\frac{^{\mathcal{I}}\mathrm{d}(\cdot)}{\mathrm{d}t}$ represents the derivative in the reference frame $\mathcal{I}$. By expressing the derivatives in the body frame $\mathcal{B}$ using the moving axes theorem[1] and assuming that the aircraft is a rigid body, one obtains:

$$a_{Q/\mathcal{I}} = \frac{^{\mathcal{B}}\mathrm{d}v_{P/\mathcal{I}}}{\mathrm{d}t} + \boldsymbol{\omega}_{\mathcal{B}/\mathcal{I}} \times v_{P/\mathcal{I}} + \frac{^{\mathcal{B}}\mathrm{d}\boldsymbol{\omega}_{\mathcal{B}/\mathcal{I}}}{\mathrm{d}t} \times r_{PQ} + \boldsymbol{\omega}_{\mathcal{B}/\mathcal{I}} \times \left(\boldsymbol{\omega}_{\mathcal{B}/\mathcal{I}} \times r_{PQ}\right)\,. \tag{1.20}$$

1.3.2 Dynamic equations

Translational motion

Integrating the first cardinal equation for a particle of mass $\mathrm{d}m$ located at a generic point Q over the entire aircraft volume $\mathcal{V}$ yields the equation for translational motion for the entire aircraft:

$$\int_{\mathcal{V}} \mathrm{d}F_Q = \int_{\mathcal{V}} a_{Q/\mathcal{I}}\ \mathrm{d}m\,. \tag{1.21}$$

By substituting Equation (1.20) into Equation (1.21) results in the sum of all external forces F acting on the aircraft:

$$F = \int_{\mathcal{V}} \left[\frac{^{\mathcal{B}}\mathrm{d}v_{P/\mathcal{I}}}{\mathrm{d}t} + \boldsymbol{\omega}_{\mathcal{B}/\mathcal{I}} \times v_{P/\mathcal{I}} + \frac{^{\mathcal{B}}\mathrm{d}\boldsymbol{\omega}_{\mathcal{B}/\mathcal{I}}}{\mathrm{d}t} \times r_{PQ} + \boldsymbol{\omega}_{\mathcal{B}/\mathcal{I}} \times \left(\boldsymbol{\omega}_{\mathcal{B}/\mathcal{I}} \times r_{PQ}\right)\right] \mathrm{d}m\,. \tag{1.22}$$

[1] The moving axes theorem states that for any two frames of reference $\mathcal{I}$ and $\mathcal{J}$, using the notation previously introduced, for any generic vector b the following holds true:

$$\frac{^{\mathcal{I}}\mathrm{d}b}{\mathrm{d}t} = \frac{^{\mathcal{J}}\mathrm{d}b}{\mathrm{d}t} + \boldsymbol{\omega}_{\mathcal{J}/\mathcal{I}} \times b\,.$$

Taking point P coincident with the center of gravity G of the aircraft simplifies several terms, leading to:

$$F = m\,\dot{v}_G + \boldsymbol{\omega} \times m\,v_G\,. \tag{1.23}$$

Here, v_G is the velocity of the center of gravity measured with respect to the inertial frame, $\boldsymbol{\omega}$ is the angular velocity measured in the inertial frame, and m is the total mass of the aircraft, calculated as:

$$m = \int_{\mathcal{V}} \mathrm{d}m\,. \tag{1.24}$$

Rotational motion

The *second cardinal equation* states that for a particle of mass located at point Q, with moments taken with respect to point P, the following equation holds true:

$$\mathrm{d}M_P = r_{PQ} \times \mathrm{d}F_Q = \mathrm{d}m\; r_{PQ} \times a_{Q/\mathcal{I}}\,. \tag{1.25}$$

Integrating equation (1.25) over the entire aircraft's volume $\mathcal{V}$ and substituting the expression of $a_{Q/\mathcal{I}}$ (Equation (1.20)) leads to:

$$M_P = \int_{\mathcal{V}} \mathrm{d}m\; r_{PQ} \times \left[\frac{{}^{\mathcal{B}}\mathrm{d}v_{P/\mathcal{I}}}{\mathrm{d}t} - r_{PQ} \times \frac{{}^{\mathcal{B}}\mathrm{d}\boldsymbol{\omega}_{\mathcal{B}/\mathcal{I}}}{\mathrm{d}t} + \boldsymbol{\omega}_{\mathcal{B}/\mathcal{I}} \times \left(v_{P/\mathcal{I}} - r_{PQ} \times \boldsymbol{\omega}_{\mathcal{B}/\mathcal{I}} \right) \right]\,. \tag{1.26}$$

By considering, as mentioned, P coincident with G, one obtains:

$$M_G = J_G\,\dot{\boldsymbol{\omega}} + \boldsymbol{\omega} \times J_G\,\boldsymbol{\omega}\,, \tag{1.27}$$

Here, $\boldsymbol{\omega}$ is the angular velocity measured in the inertial frame, and J is the inertia matrix defined as follows:

$$J_G = \begin{bmatrix} J_{xx} & -J_{xy} & -J_{xz} \\ -J_{xy} & J_{yy} & -J_{yz} \\ -J_{xz} & -J_{yz} & J_{zz} \end{bmatrix}\,, \tag{1.28}$$

where

$$J_{xx} = \int_{\mathcal{V}} \left(y^2 + z^2\right) dm\,, \quad J_{yy} = \int_{\mathcal{V}} \left(x^2 + z^2\right) dm\,, \quad J_{zz} = \int_{\mathcal{V}} \left(x^2 + y^2\right) dm\,,$$
$$J_{xy} = \int_{\mathcal{V}} (xy)\, dm\,, \quad J_{xz} = \int_{\mathcal{V}} (xz)\, dm\,, \quad J_{yz} = \int_{\mathcal{V}} (yz)\, dm\,.$$

Hence, the 6-degrees-of-freedom equations of motion with respect to the center of gravity are as follows:

$$\begin{cases} F = m\,\dot{v}_G + \boldsymbol{\omega} \times m\,v_G \\ M_G = J_G\,\dot{\boldsymbol{\omega}} + \boldsymbol{\omega} \times J_G\,\boldsymbol{\omega}. \end{cases} \tag{1.29}$$

It is important to remark that since no assumption on the flight mode of the aircraft (multicopter, transition flight, and fixed-wing) has been made, Equation (1.29) is true for all modes. The difference between flight modes is related to external forces and moments acting on the vehicle, which will be defined in the next Section.

1.4 Flight test campaign

The flight test campaign took place between March and October 2023 and was conducted with progressively more focused tests. These tests provided insights ranging from the basic functioning of all the drone systems to the specific performance aspects under investigation. The author was responsible, as flight test engineer, for planning the tests, drafting flight test cards and analyzing collected data; the co-supervisors served as test pilot (Eng. Elia Martinelli) and flight test engineer at the ground control station (Eng. Nicolò Battaini). This involved managing parameters and providing telemetry data support to the pilot during the execution of the tests.

Flight test cards

The flight test cards were designed to be schematic, clear, and comprehensive, guiding the team through the entire process. This included decisions on tools to bring, pre-flight briefings, test execution, and subsequent data analysis. Each flight test card incorporated critical information:

- names of the tests scheduled for the specific day;
- objective of each test;
- expected behaviour of the aircraft and potential safety-critical aspects;
- parameters to be modified and monitored for the specific tests;
- procedure for executing the tests;
- necessary data to be extracted for post-processing and the validity constraints of the test points.

Given the comprehensive data recording capabilities of the onboard Pixhawk system, which logs information from all sensors throughout the flight, this data specification primarily facilitates post-flight analysis rather than in-flight operations. Additionally, blank spaces are available to note weather conditions, the name of each flight log with associated comments, or other relevant information.

Flight test location

The flights have been conducted in the airspace of an hobbyist airfield located in Castellazzo di Bollate, Milan. Figure 1.2 illustrates the airfield from a top view, measuring 410 m in length and 315 m in width. It provides two airstrips in a cross configuration, enabling take-off and landing from all four directions. Given the VTOL nature of the studied aircraft, the extremities of these airstrips were utilized as home points for executing the transition phase, maximizing headwind, as discussed in detail in Chapter 4.

Figure 1.2: Top view of the airfield of Castellazzo di Bollate, Milan

The dimensions of the airfield presented a significant challenge, as later elaborated in Chapter 5, due to limited space for proper aircraft stabilization, rendering some tests susceptible to high variability of parameters.

1.4.1 Flight test setup

The process involved in conducting a successful flight test day is structured and has been precisely followed to minimize unexpected events. The execution of each

specific test is discussed in the associated Chapters. In addition to that, the following steps were followed:

- **objective setting**: definition of the goals of the tests and the researched insights or performance metrics;
- **equipment checklist**: ensuring the presence and operational readiness of requisite equipment, from tools needed for aircraft assembly to battery chargers and auxiliary gear for potential on-site repairs;
- **environment analysis**: providing a brief summary highlighting ambient conditions such as wind velocity, direction, air temperature, and other environmental elements that might affect the test outcomes;
- **assembly of the drone**: reattachment of the wings, which are disassembled for ease of transportation, and check electronic cable connections.
- **pre-flight briefing**: a comprehensive review of the test cards, the procedural details for successful test execution and potential critical events;
- **pre-flight checks**: ground tests to verify the integrity of electronic components, inspect vertical and forward-flight motors, control surfaces, calibrate sensors, and cross-check related test parameters.
- **execution of the test**: following the procedure outlined in the flight test cards and the indications resulting from the pre-flight briefing;
- **preliminary data analysis**: annotation of data log details, assessing data quality, determining if further tests are needed, and noting any anomalous behaviours observed before carrying on subsequent tests.

1.4.2 Data collection

As previously mentioned, the Pixhawk board serves as a comprehensive data collection hub, gathering information about the aircraft, including altitude, attitude, accelerations, speed, and system status. The sensor suite, integrated into the board and externally fitted, comprises:

- **inertial measurement units (IMU)**: encompassing a 3-axis accelerometer for precise linear acceleration measurements and a gyroscope to determine angular velocities;
- **integrated magnetometer**: a tool for estimating the aircraft's heading by sensing Earth's magnetic field;
- **barometer**: an instrument to estimate altitude based on atmospheric pressure readings;

- **GPS module**: a dual-purpose component providing both positional information via its GPS unit and offering a supplementary compass as a redundancy measure to the internal magnetometer;
- **Pitot tube**: crucial for acquiring airspeed data.

Table 1.1 outlines the main parameters used during the post-processing and analysis of the tests discussed in Chapters 4 and 5; additionally, the table reports their source and their sampling frequency.

Quantity	Source	Sampling frequency [Hz]
V [m/s]	Pitot tube	10
V_{ground} [m/s]	GPS	5
ROC [m/s]	GPS	5
H [m]	GPS	5
ϕ, θ, ψ [rad]	IMU	225
p, q, r [rad/s]	IMU	225
a_x, a_y, a_z [m/s^2]	IMU	225

Table 1.1: Quantities processed during tests' analisis and their source

Additionally, QGroundControl is employed as a versatile open-source ground control station (GCS) software, providing comprehensive flight control and mission planning for MAVLink-enabled drones [14]. Smooth communication between the drone and QGroundControl, operating on a computer, is achieved using the Holybro SiK Telemetry Radio [15], a MAVLink protocol-compatible module ideally suited for Pixhawk controllers. This telemetry setup not only simplifies the calibration and configuration of the drone's hardware and software but also provides real-time feedback on vital metrics, from battery status and airspeed to altitude and positional data mapped onto a localized field representation.

1.4.3 Data filtering

Due to the high frequency of data collection, a filtering process is essential to minimize noise, retaining only significant information for analysis, and smoothing data representation.
A Butterworth filter, implemented in Matlab scripts using the built-in *filtfilt* function, as described in [16], has been employed. This function is chosen for its zero-phase filtering process, involving filtering the data in both the forward and reverse directions [17]. The filter is implemented in Matlab as follows:

$$[b,a] = \text{butter}(filter\_order,\omega_n)\,,$$
$$\text{filt\_signal} = \text{filtfilt}(b,a,\text{raw\_signal})\,.$$

Here,

- b and a are arrays containing the numerator and denominator coefficients of the Butterworth filter transfer function, respectively;
- $filter\_order$ is the order of the filter;
- ω_n is the normalized cut-off frequency defined as

$$\omega_n = \frac{f_C}{f_S/2}\,.$$

The terms f_C and f_S are the desired cut-off frequency and the sampling frequency (reported in Table 1.1), respectively.
The order of the filter affects its ability to capture peaks in the signal given a certain cut-off frequency. While a lower order filter may eliminate valuable information, a higher order can increase computational cost for little improvement in the filtered signal. Through a trial-and-error approach, the order of the filter has been selected for all the signals as reported in Table 1.2.
The cut-off frequency has been chosen through the analysis of the single-sided spectrum of the signal obtained using the Fast Fourier Transform (FFT) built-in function in Matlab.
A sample of the filtering of an acceleration is illustrated in Figure 1.3, and the cut-off frequencies selected for each of the filtered data is reported in Table 1.2.

Quantity	Cut-off frequency [Hz]	Filter order
V [m/s]	0.01	4
V_d [m/s]	0.007	4
a_x [m/s^2]	1	5
a_z [m/s^2]	0.4	5

Table 1.2: Cut-off frequencies and filter order for all the filtered quantities

1.5 PX4 flight modes

The PX4 autopilot system offers a diverse range of flight modes catering to various degrees of autonomy. This section provides an overview of these modes, categorizing them based on flight phases for VTOL-type aircraft.
The interested reader can refer to Appendix A of [3] for a more detailed description of the flight modes.

1.5.1 Multirotor flight modes

The following flight modes, specifically described in the context of MR flight, are presented in an increasingly heavier pilot workload order and include only the modes that have been employed during the current work.

Position mode

The position mode is an easy-to-fly mode in which the right stick controls acceleration over ground in all directions, while the left stick up-down movement controls the ascent and descent speed; during these maneuvers the velocity control loop is active. This flight mode represents the safest option: when the sticks are released and centered the aircraft stops and hovers in place by activating the position loop.

Altitude mode

The altitude mode is relatively easy to pilot too. In this mode, the roll and pitch stick controls the roll angle ϕ and the pitch angle θ, respectively; the throttle stick controls the yaw rate $\dot{\psi}$ (left-right movement) and the ascent/descent speed (up-down movement). Differently from the position mode, when the sticks are centered the aircraft will level and maintain the current altitude but will not hold a fixed position, having active only the attitude and altitude loop; if moving in the horizontal plane or subject to external disturbances, the aircraft will continue moving until aerodynamic resistance dissipates momentum.

Manual mode

The manual mode is the least assisted and most challenging mode deployed during the campaign. The right stick controls the roll angle ϕ and the pitch angle θ, while the left stick's left-right movement controls the yaw rate $\dot{\psi}$. The challenge of this flight mode is the throttle stick; the up-down movement of the throttle stick controls directly the throttle of the motors. Only the attitude loop is active; when sticks are centered the aircraft levels and stops, but maintaining altitude and position requires continuous pilot intervention. Any external force or unbalance will cause the aircraft to drift and require pilot intervention to regain control.

1.5.2 Fixed-wing flight modes

Similar to the multirotor flight modes, the fixed-wing flight modes presented here are in an increasing difficulty order and provide an overview of the deployed modes.

Altitude mode

In altitude mode, the right stick controls the roll angle ϕ with its left-right movement, while it controls climb/descent rate $\dot{H}$ with its up-down movement. The

left stick controls the rudder deflection δ_r with its left-right movement and the forward speed V with the up-down. Centering the sticks maintains current altitude and speed with the TECS controller and attitude loop active. However, the aircraft's course is not actively held against the wind.

Stabilized mode mode

Stabilized mode for fixed-wing aircraft involves the right stick controlling roll and pitch angles. The left-right movement of the left stick manages rudder deflection, and the up-down movement controls motors throttle. Altitude control relies on a combination of throttle and pitch angle commands. Only the attitude loop is active, and when the right stick is centered, the aircraft levels but does not actively maintain course against the wind.

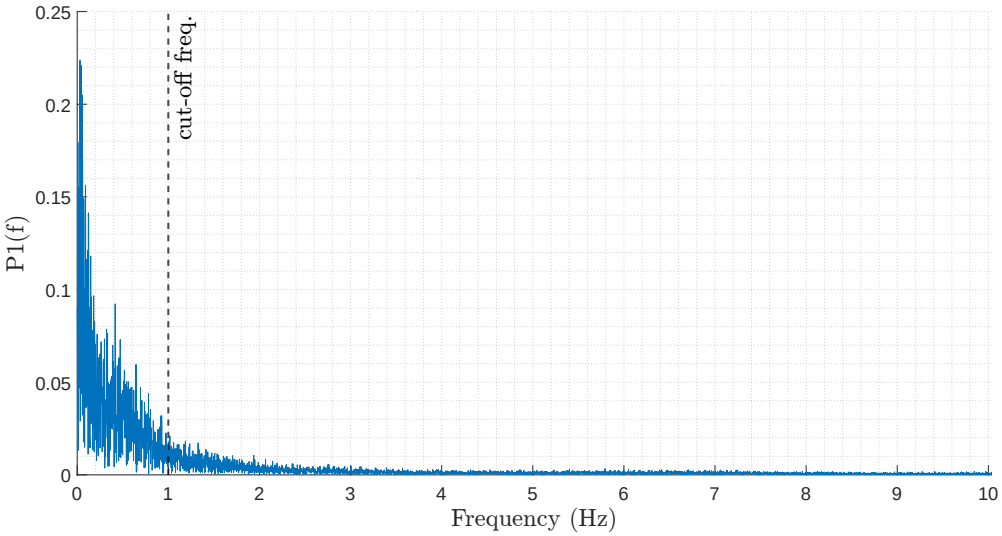

(a) Single-sided spectrum amplitude of the stability x-axis acceleration.

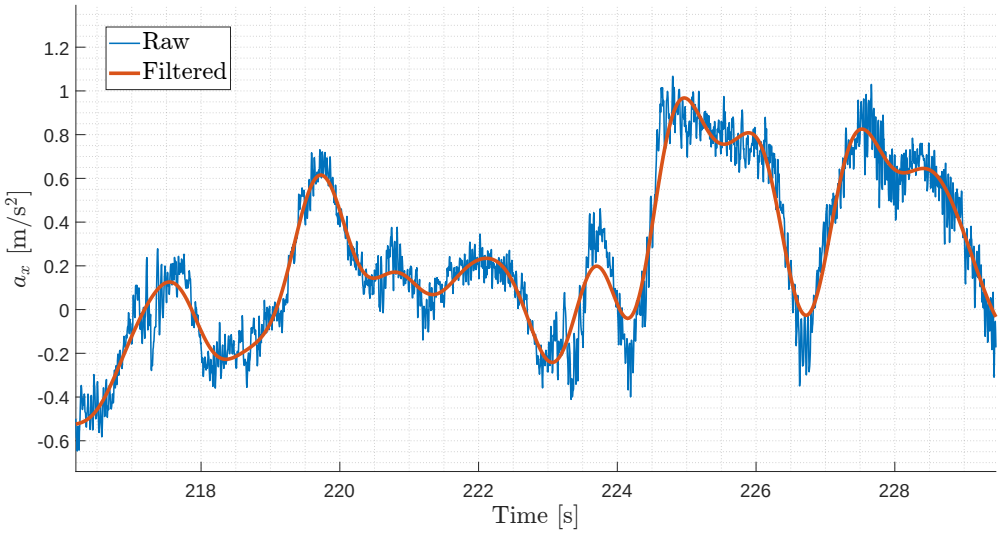

(b) Filtering comparison of the stability x-axis acceleration.

Figure 1.3: Sample of the filtering process applied the acceleration of the aircraft

Chapter 2

Wing and tail redesign, manufacturing and testing

Throughout the evolution of the project, the weight of the drone gradually increased, raising the necessity of a reevaluation of its aerodynamics which have not been modified since the original design. During the outdoor flight testing campaign, it has been quickly confirmed that the lifting surfaces were no longer suited and upgrades were needed to face the issues.

This chapter explains how these problems have been tackled and resolved. First, the adjustments to the size of both the wing and tail to better fit the change in weight of the drone during its development will be discussed. After that, the analysis performed with the support of OpenVSP ([18]), an open source tool developed by NASA for parametric geometry analysis, is showed to double-check the new design. In the third section, the new sizes of the control surfaces are presented and the ability of the servo motors to produce the required maximum torque is discussed. Lastly, in the fourth and fifth sections, the aeroelastic problems occurred during the flight test campaign are studied and the improvements done to the wing to overcome them are presented with the associated experimental tests.

2.1 Wing and tail resizing

From the beginning of the project, the geometry of the VTOL drone remained unchanged. However, during its evolution, it underwent many modifications: new parts were introduced, motors and propellers were upgraded, electronic components were altered, and sections of the fuselage were replaced with carbon fiber plates, among other changes. These adjustments inevitably increased the weight, deviating from the original design expectations.
A crash occurred during the flight test campaign (March 23rd, 2023) prompted an investigation carried out using the available data log and the on-site recordings.

This analysis revealed that the wing could not generate sufficient lift to support the drone during its fixed-wing flight phase and the assumed main reasons were:

- the chosen manufacturing technique led to difficulties in maintaining the intended airfoil shape across the wing span. This inconsistency caused the wing to behave more like a flat plate in certain sections, further diminishing its lift capability.
- The wing area was undersized because it had been designed following the conventional methods which presumed an aerodynamically efficient fuselage in which the wing's central portion is buried. This did not properly apply to the case at hand instead, in which the shape of the fuselage is quite bluff and interferes significantly with the flow.

The main resizing steps are shown below while the solution to the airfoil's shape issue is explored in detailed in Section 2.5.

Wing

The design aimed for a maximum lift coefficient $C_{Lmax} = 1.10$. This choice was slightly conservative, being reduced from the original design value of 1.15 to account for possible manufacturing and assembly imperfections. Additionally, the target stall speed was set at $V_s = 12\,m/s$. Three fundamental constraints guided the design:

- a wing's pitch angle $i_w = 4.9°$ dictated by the wing's spar attachment points on the fuselage that could not be changed;
- a mean aerodynamic chord $MAC \leq 0.3$ m to ensure the wing's trailing edge did not extend beyond the fuselage's rear, mitigating vortex effects and aerodynamic interference;
- a maximum wing span $b \leq 3$ m to facilitate transport and to use the existing carbon fiber tubes as spars without compromising structural integrity.

Given the fuselage's non-ideal aerodynamic profile, calculations were focused on the effective lift-generating wing area, S_{eff}. The vertical forces equilibrium equation

$$W = \frac{1}{2}\rho V^2 S C_L\,,$$

leads to

$$S_{eff} = \frac{2\,W}{\rho V_s^2 C_{L_{max}}}\,. \tag{2.1}$$

In this equation, ρ is the air density, W is the weight of the aircraft, V_s is the stall speed, and $C_{L_{max}}$ is the maximum lift coefficient. The required effective wing surface results in $S_{eff} = 0.6471$ m^2.
By setting $MAC = 0.26$ m, maximum allowed margin to reach exactly the fuselage rear wall, the required wing span, inclusive of the fuselage width, was

$$b = \frac{S_{eff}}{MAC} + 0.42\,, \tag{2.2}$$

with resulting value $b = 2.91$ m, thus rounded it to 3 m to facilitate design and manufacturing. Consequently, also the aspect ratio, defined as

$$AR = \frac{b^2}{S_{tot}}\,,$$

changed from 9.00 to 11.54. The results of the sizing are summarized in Table 2.1.

Parameter	Previous value	New value
MAC [m]	0.25	0.26
b [m]	2.25	3.00
S_{tot} [m^2]	0.562	0.780
S_{eff} [m^2]	0.457	0.671
AR [-]	9.00	11.54

Table 2.1: Wing resizing results

Tail

Similarly to the wing modifications, the tail was also resized following the method presented in [1]. The main steps of this process are presented below starting from the horizontal and vertical tail surfaces, respectively S_h and S_v, calculated as

$$S_h = \frac{V_h\, MAC\, S}{x_{opt}}\,, \tag{2.3}$$

$$S_v = \frac{V_v\, b\, S}{x_{opt}}\,, \tag{2.4}$$

where V_h and V_v are respectively the horizontal and vertical tail volumes, and x_{opt} is the tail arm (distance between the wing aerodynamic centre and the tail aerodynamic centre) [1]. Taking the wing's revised dimensions from Table 2.1 and keeping the values $V_h = 0.5$, $V_v = 0.03$ and $x_{opt} = 1.08$ m since the tail booms and fuselage dimensions are unchanged from the original design, the resulting surface areas are computed to be $S_h = 0.094\,\text{m}^2$ and $S_v = 0.065\,\text{m}^2$. To simplify the

manufacturing effort, the chord of both vertical and horizontal tail surfaces are set equal, leading to $MAC_h = MAC_v = 0.13$ m.
After deciding the dimensions of the tail surfaces, the incidence angle of the horizontal surface has to be calculated to ensure the moment equilibrium during the cruise phase, ideally without any elevator deflection, being the wing incidence constrained. The procedure adopted, as presented in [1] and [4], is summarized here, focusing on the main steps.
Considering a conventional two-surface aircraft, the moment equilibrium with respect to the center of gravity can be derived. This is then normalized by the term $\frac{1}{2}\rho v^2 S$ and results in

$$C_{M_{ac}}^{wf} MAC + C_L d - \gamma \sigma C_L^h l = 0\,, \tag{2.5}$$

where C_{Mac}^{wf} symbolizes the pitching moment generated by the combined effects of the wing and fuselage, CL_L and C_L^h represent respectively the wing's lift coefficient and the horizontal surface's lift coefficient; the distances d and l correspond to the span between the wing's aerodynamic center and the aircraft CG, and from the aircraft CG to the tail's aerodynamic center, respectively, as illustrated in Figure 2.1. Meanwhile, γ represents the ratio of the tail's dynamic pressure to that of the wing, and σ represents the surface area ratio of tail to wing.

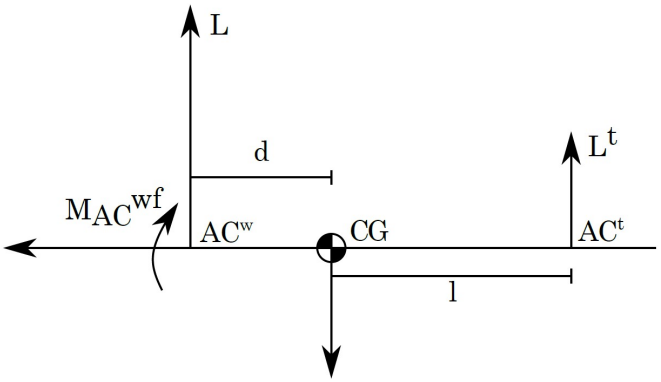

Figure 2.1: Simplified moment equilibrium scheme for tail incidence computation (source [1])

Given the wing airfoil's moment coefficient C_m and wing sweep angle Λ, this value is estimated as:

$$C_{M_{ac}}^{wf} = C_m \frac{AR \cos \Lambda^2}{AR + 2\cos \Lambda}\,. \tag{2.6}$$

From the moment equilibrium shown in Equation (2.5), defining $\bar{d} = d/MAC$ and rearranging, the horizontal tail's lift coefficient becomes

$$C_L^h = \frac{C_{M_{ac}}^{wf} + \bar{d} C_L}{\gamma V_h}\,. \tag{2.7}$$

This allows the calculation of the tail's angle of attack (AoA) as

$$\alpha_h = \frac{C_L^h}{C_{L_\alpha}^h}\,, \tag{2.8}$$

where $C_{L_\alpha}^h$ represents the tail lift curve slope. The next term to be defined for the calculation of the tail incidence is the downwash, ϵ, caused by the wing to the airflow seen by the tail. The adopted model accounts for a constant term, ϵ_0, and a term proportional to the wing AoA, α, as

$$\varepsilon = \varepsilon_0 + \frac{\partial \varepsilon}{\partial \alpha}\alpha\,, \tag{2.9}$$

and according to [4], the two coefficients can be computed as:

$$\varepsilon_0 = \frac{2C_L^w}{\pi AR}\,; \tag{2.10}$$

$$\frac{\partial \varepsilon}{\partial \alpha} = \frac{2C_{L_\alpha}^w}{\pi AR}\,. \tag{2.11}$$

Finally, the horizontal tail incidence i_h is

$$i_h = \alpha_h + \varepsilon\,, \tag{2.12}$$

The resulting value is $i_h = 5.6°$. The comprehensive tail resizing outcomes are summarized in Table 2.2.

Parameter	Previous value	New Value
MAC_h [m]	0.10	0.13
b_h [m]	0.61	0.72
S_h [m^2]	0.0610	0.0939
AR_h [-]	6.10	5.54
i_h [deg]	3.0	5.6
MAC_v [m]	0.10	0.13
b_v [m]	0.18	0.25
S_v [m^2]	0.0183	0.0325
AR_v [-]	1.83	1.92

Table 2.2: Tail resizing results

2.2 Control surfaces and servomotors

After resizing the wing and the tail, also the control surfaces had to be upgraded, and the servomotors capabilities checked against the increased hinge moments

they are expected to withstand. The reader should note that the reported procedures contain only the main steps, since this chapter covers a resizing, and the complete design approach is well explained in [1] with references to [4].

Ailerons

Ailerons play a crucial role in an aircraft's lateral dynamics. Their design involves defining the span, chord, and spanwise position on the wing. After establishing these parameters, the design quality has been assessed against the roll performance requirements of the MIL F 8785 C regulation for flight qualities ([19]). This regulation, meant for military manned aircraft, served as a reference due to the absence of handling qualities regulations for UAVs. This methodology has been used also by researchers from University of Southampton [6].
As in [1], the aileron's span was set at 20% of the semi-wing span, resulting in $b_a = 0.3$ m. To maintain the aileron effectiveness τ_a at its original design value of 0.4, Figure 2.2 indicates that the chord of the aileron should be $MAC_a = 20\%MAC$. Hence $MAC_a = 0.052$ m. Finally, the outboard position of the aileron has been assumed to reach the tip of the wing. This placement maximizes the moment arm between the aileron and roll axis, making the ailerons more effective.

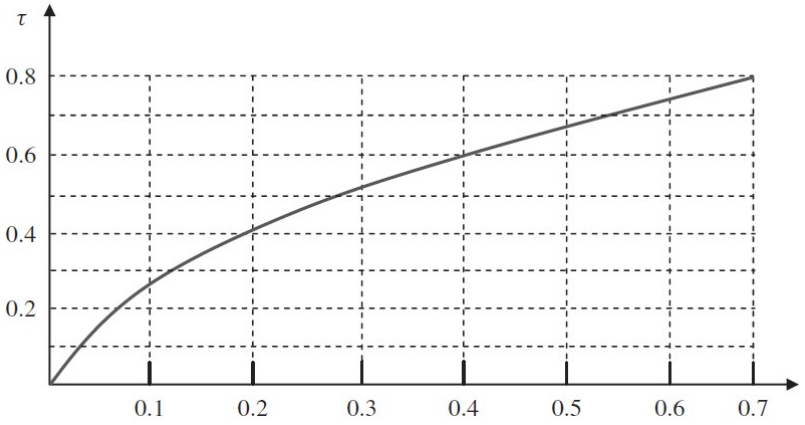

Figure 2.2: Graph illustrating the control surface effectiveness τ as a function of the control surface-to-lifting surface chord ratio on the x-axis (source [4])

For structural purposes, the outboard position of the aileron has been adjusted to be 0.1 m inwards and to be conservative with the sizing, the dimensions of the aileron has been slightly increased to $b_a = 0.4$ m and $MAC_a = 0.055$ m, which are the final values used during the manufacturing discussed in Section 2.5. The roll performance was then evaluated in accordance with the military standard mentioned previously. This standard specifies the time needed to achieve a bank angle of $\phi_{required} = 45°$ depending on the aircraft class and flight phase. The considered UAV falls under class 1, denoting small and light aircraft with low

maneuverability and the selected flight phase, B, encompasses climb, cruise, loiter, descent, and aerial delivery. This results in the following requirements:

- Level 2: $t_{req} < 2.5$ s
- Level 1: $t_{req} < 1.7$ s.

To account for the wider wings, the value of the inertia around the roll axis previously obtained from CAD estimation has been increased by 50%. The resulting time required is $t_{req} = 0.47$ s which largely meets the Level 1 standard.

Elevator

The typical elevator design procedure is centered on the rotation at take-off, which is its most demanding condition for a general aviation aircraft. Being this aircraft a VTOL drone, thus not requiring a conventional take-off, the elevator's design procedure is simplified and based on common values suggested by [4]. This led to the span staying the same, since it was determined by the distance between the two motor booms of the aircraft, and to the chord increasing proportionally to the increase in the horizontal surface chord:

- $b_e = 0.264$ m;
- $MAC_e = 35\%\, MAC_h = 0.045$ m.

Rudder

As for the elevator, also the rudder is designed by selecting the most demanding flight condition the aircraft will operate in between asymmetric thrust due to one-engine-inoperative, crosswind landing or spin recovery. Since the nature of the aircraft allows it to take-off and land vertically, crosswind is not of concern. Its low maneuverability also means we can overlook spins, leaving the one-engine-inoperative condition as the most critical scenario.

To begin, the suggestion made in [4] is followed to set the ratio between rudder and vertical tail span to $\frac{b_r}{b_v} = 0.7$; then, the asymmetric flight condition is studied to determine the ratio between chords $\frac{MAC_r}{MAC_v}$. The first step is the definition of the distance between the forward flight (FF) motors and the x-axis of the aircraft as indicated in Figure 2.3, $y_T = 0.174$ m, and the maximum thrust produced by the FF motor and propeller $\mathcal{T}_L$. The information about the maximum thrust produced by the motor is obtained from wind tunnel data, better discussed in Chapter 3. The resulting value is $\mathcal{T}_L = 7\,\mathrm{N}$, at stall speed and full throttle. The asymmetry of thrust generates a yawing moment about the aircraft's CG equal to

$$\mathcal{N}_a = -\mathcal{T}_L y_T\,, \tag{2.13}$$

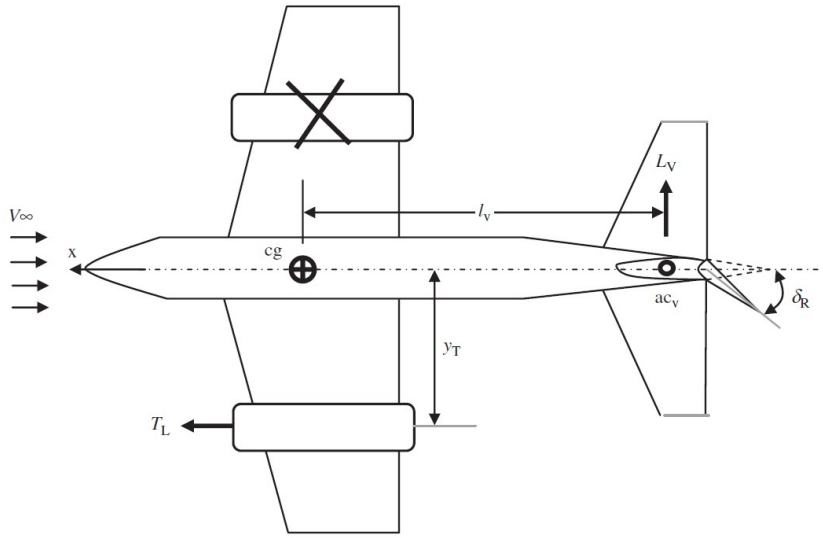

Figure 2.3: One-engine-inoperative moments balance scheme (source [4])

which the rudder has to be able to counteract with an opposite moment. Some assumptions are made to simplify the equilibrium equation, such as: symmetric aircraft about the xz-plane, straight flight with no sideslip $\beta = 0$ deg and no aileron deflection $\delta_a = 0$ deg, leading to

$$\mathcal{N}_a = \frac{1}{2}\rho v^2 SbC_{n_{\delta_r}}\delta_r \,, \tag{2.14}$$

that can then be inverted to obtain the value of the yawing moment coefficient derivative with respect to rudder deflection $C_{n_{\delta_r}}$ given that all the other terms are known and the deflection δ_r is arbitrary. Then, considering that the control derivative can also be written as a function of the tail parameters as

$$C_{n_{\delta_r}} = -C^v_{L_\alpha} V_v \gamma \tau_r \frac{b_r}{b_v} \,, \tag{2.15}$$

the rudder's effectiveness τ_r can be obtained. Through Figure 2.2, the ratio $\frac{MAC_r}{MAC_v}$ can be finally determined: the resulting values are $\tau_r = 0.43$ and $\frac{MAC_r}{MAC_v} = 0.25$, leading to $MAC_r = 0.0325$ m rounded to 0.035 m during the manufacturing process with span $b_r = 0.19$ m. A summary of the control surfaces final dimensions is shown in Table 2.3.

Servomotors

In concluding the resizing process, it is important to assess the maximum torque provided by the servomotors against the maximum hinge moment they are expected to encounter. For this analysis, XFOIL, a tool that employs a combination

Parameter	Previous value	New Value
MAC_a [cm]	5.0	5.5
b_a [cm]	22.5	40.0
MAC_e [cm]	3.0	4.5
b_e [cm]	26.4	26.4
MAC_r [cm]	2.5	3.5
b_r [cm]	11	19

Table 2.3: Control surfaces resizing results

of potential flow theory and boundary layer methods to predict the aerodynamic performance of subsonic isolated airfoils, was used. XFOIL was developed in the late 1980s by Professor Mark Drela of the Massachusetts Institute of Technology (MIT) ([20]).

An analysis was conducted under the most adverse conditions, specifically at an airspeed $V = 22$ m/s and with maximum deflections of $\delta_a = \delta_e = 20°$ to derive the hinge moment coefficient C_H for both the wing and tail airfoil. After determining the hinge moment coefficient for the aileron and elevator, the hinge moment can be computed using

$$M_H = \frac{1}{2}\rho V^2 MAC^2 b_{mov} C_H K_s \,. \tag{2.16}$$

In this context, b_{mov} represents the span of the moving surface. The safety factor K_s is set to 1.7, a value specifically adopted from the original design, as detailed in [1]. The resulting hinge moment coefficient values per unit length were $C_{H_a} = 0.013$ and $C_{H_e} = 0.025$, leading to $M_{H_a} = 0.177$ Nm and $M_{H_e} = 0.0563$ Nm. The connection between the servomotors and the moving surfaces involves a mechanism consisting of two horns, one attached to the moving surface and the other to the servomotor, and a connecting pushrod. This configuration introduces a hinge moment and motor torque relationship that is determined by the horn lengths, in this case $L_{servo} = 12$ mm and $L_{mobile} = 8$ mm. The servomotor's torque is given by

$$M_{servo} = \frac{L_{servo}}{L_{control}} M_H \,, \tag{2.17}$$

resulting in $M_{servo_{max}} = 0.2658$ Nm. Given that the installed servomotors, the Corona 939 Metal Gear from [21], can produce a peak torque of 0.27 Nm, and considering the horn arm ratio adopted represents the most unfavorable scenario, these motors were considered still appropriate for the modifications.

2.3 OpenVSP analysis

A Vortex Lattice Method (VLM) simulation of the obtained geometry has been performed in OpenVSP to validate it. The main objectives of the analysis were the prediction of the drag polar curve with the new lifting surfaces, and the validation of the elevator's sizing by checking its deflection at various trim conditions. Additionally, an approach to correctly account for the wing-fuselage interaction within the VLM method has been researched. During preliminary design phases of conventional aircraft with slender and aerodynamically efficient fuselages, this interaction is typically incorporated into the drag coefficient through correction coefficients.

Alongside VSPAero, the aerodynamic solver of OpenVSP, a MATLAB routine was developed in [2] to maximize the solver's capabilities and allow the automation of the analysis by compensating the lack of some features, *e.g.,* the calculation of the trim state, namely the values of AoA and elevator deflection, for any given aircraft weight and flight condition in which the aircraft is in equilibrium. Figure 2.4 shows the flow chart of the three main routines, further detail can be found in Chapter 1 of [2].

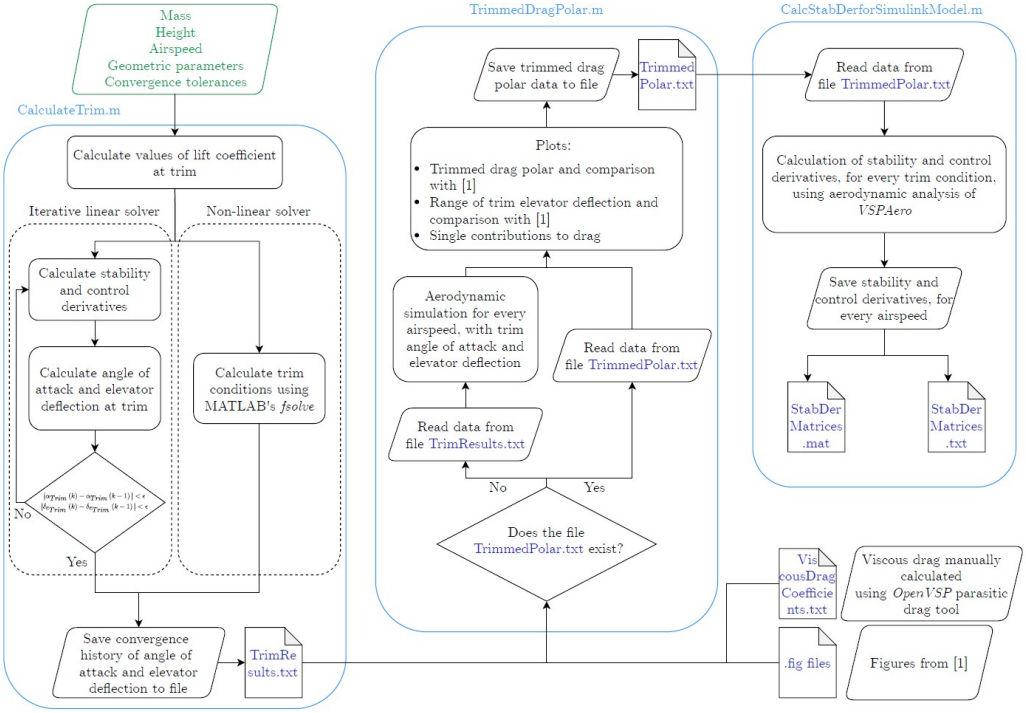

Figure 2.4: Aerodynamic analysis routine flowchart (source [2])

The model of the aircraft is shown in Figure 2.5: it includes the main wing, horizontal and vertical tail, fuselage, engine booms and control surfaces. The tail's supports, the motors and the propellers are not modeled in it because they are

neglected during the analyses since VLM solvers do not generally attach trailing wakes to bluff bodies, and therefore, they do not contribute to lift and induced drag in the adopted software.

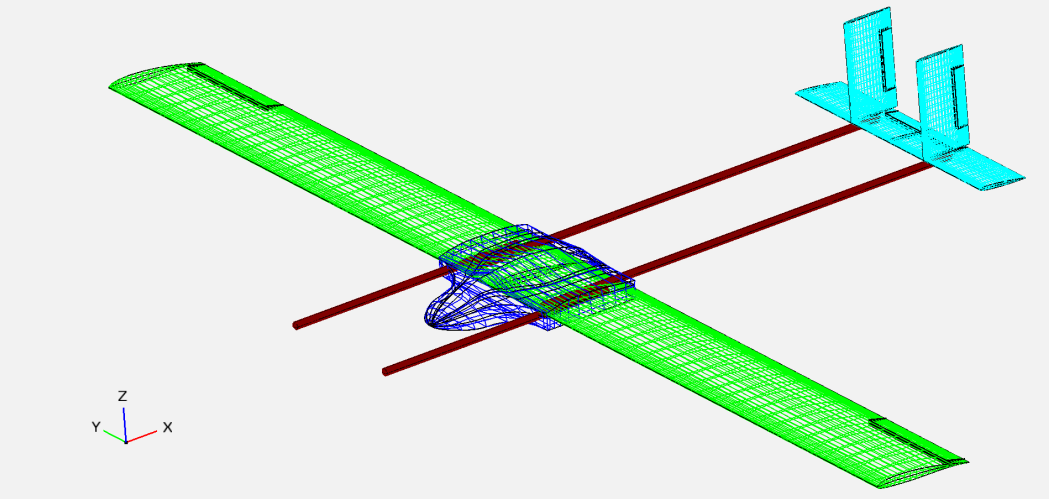

Figure 2.5: OpenVSP model of the UAV

2.3.1 Wing-fuselage interaction method research

Before starting the analyses, some research has been done looking for approaches and considerations about the presence of the fuselage, to correct any overestimation that might be caused by neglecting the portion of wing buried in it. The concern was caused by the previously mentioned incident occurred in March that raised the question of weather the results used to carry on the design of the aircraft were too optimistic and needed correction. The approach proposed in Chapter 9 of [5], originally intended for Prandtl's Lifting Line Method, is based on the observation that the lift coefficient is significantly reduced in the portion of wing where the fuselage is present.
It has to be noted that VSPAero does not completely neglect the presence of the fuselage but, as mentioned above for the motors and tail's supports, it is modeled by the tool as two neutral flat plates, as shown in Figure 2.6. These flat plates do not have an associated wake and consequently do not contribute to aerodynamic forces. This makes the fuselage's effect limited to a deflection of the airflow around the wing, effect that would be better captured by more advanced Computational Fluid Dynamics (CFD) simulations rather than a VLM solution.
The previously mentioned approach, as proposed by Gudmundsson [5], is grounded in two fundamental assumptions:

- the lift is entirely generated by the exposed wing panels, with the lift coefficients over the fuselage portion assumed to be zero;

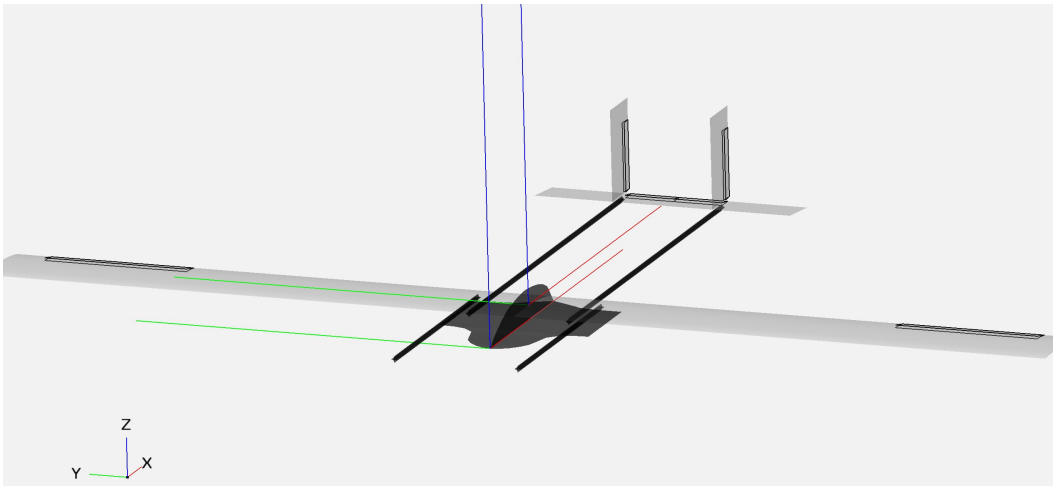

Figure 2.6: Degenerate geometry of the model for VSPAero solver

- the fuselage acts as a wall, allowing the application to the wing geometry of the reduction shown in Figure 2.7.

The wingspan $b = 3$ m will then be reduced by the width of the fuselage $w_{fus} = 0.42$ m leading to the reduced span $b_R = 2.58\,\text{m}$ found as

$$b_R = b - w_{fus}\,; \tag{2.18}$$

therefore, being the wing straight with no taper, the reduced wing area $S_R = 0.6708$ m is found as

$$S_R = S - MACw_{fus} \tag{2.19}$$

and the reduced aspect ratio $AR_R = 9.92$ as

$$AR_R = \frac{b_R^2}{S_R}\,. \tag{2.20}$$

So, rather than analyzing the complete wing, its reduced wing span and reduced area should be used in the model, and the expected result is that the wing will now require a higher AoA in order to generate the lift coefficient necessary for a given flight condition, correcting any possible overestimation.

Despite the exhaustive search, no additional approach tailored specifically to a VLM solver was identified to address the aforementioned concern. The absence of dedicated studies on this matter implies that a comprehensive analysis of the fuselage's impact is more appropriately conducted through CFD simulations rather than relying solely on a VLM solution. In light of these findings, the present study continued with the original model, with the addition of comparisons with this methods solutions when possible. However, it is strongly advised that future

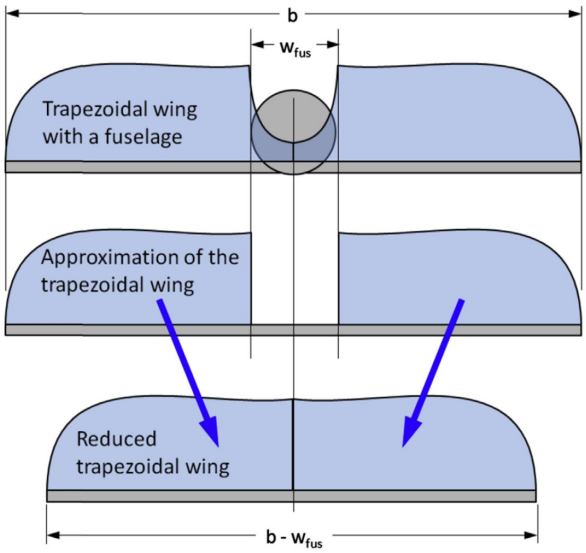

Figure 2.7: Reduced wing span to account for fuselage presence in lifting line method (source [5])

stages of this project consider the adoption of more sophisticated aerodynamic simulation software to enhance the accuracy of the analyses.

2.3.2 Analysis results

Below, the main results are summarized and shown, starting from a comparison between the trimmed drag polar in Figure 2.8: the model with $b = 3$ m and maximum take-off mass (MTOM) = 5.6 kg is the UAV with redesigned wings; the model with $b = 2.25$ m and MTOM = 6.4 kg is the previous version (geometry as in [2] and MTOM updated in [3]). It is clearly seen that the drag coefficient is slightly reduced, which is due to the higher wing aspect ratio.

Figure 2.9 illustrates the elevator's deflection at trim condition for airspeeds ranging from 10 m/s to 22 m/s; this covers the entire estimated fixed-wing flight envelope. The displayed deflection validates both the horizontal tail incidence angle, as computed in Section 2.1, and the resizing of the elevator, as outlined in Section 2.2. The design objective was to achieve zero deflection at the design cruise airspeed of 15 m/s, and the solution approximates a deflection of around 1 deg at this speed. Furthermore, the deflection required to trim the aircraft at any airspeed is quite limited, allowing a wide margin for maneuvering and making the resizing satisfactory.

Lastly, a comparison of the lift coefficient at trim against AoA is shown in Figure 2.10 for three cases: new wing with 3 m span, new wing but with the reduced span correction applied to consider the presence of the fuselage and previous model as defined above. As expected, between the model with full span

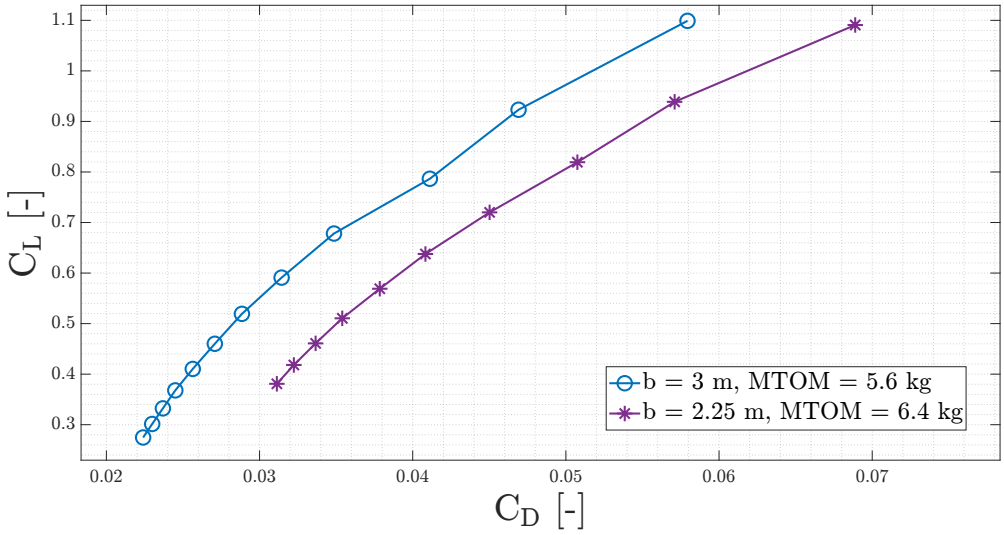

Figure 2.8: Trimmed drag polar comparison

and the one with reduced span, there is an increase in the required AoA to be able to produce the necessary lift coefficient at trim; however, the difference is not significant enough to justify the adoption of such approach, specially at higher airspeed where the two lines go to convergence. Also between the new larger wing and the previous wing the difference is not noticeable, with less than half a degree throughout the flight envelope, indicating the robustness of the design and raising no concerns about the new aerodynamic setup of the aircraft.

2.4 Aeroelastic analysis

The process of resizing the wing presented a suitable moment to re-evaluate and refine the construction methodologies. Up to that point, the design had relied on carbon fiber tubes for the spars, 3D printed ribs, and a Mylar sheet as skin. This setup had its issues, especially when it came to maintaining the desired airfoil shape. In an initial modification, as depicted in Figure 2.11, the carbon fiber tubes remained unchanged, but they were paired with hot wire cut foam for the aerodynamic shape of both the wing and the tail, which previously was made out of balsa wood. This approach was inspired by the original design methodology in [1]. However, the decision to exclude cladding proved ineffective and caused the onset of aeroelastic phenomena which led to an other incident on June 2023. This section focuses on the data analysis from that flight and the conclusions derived from it.

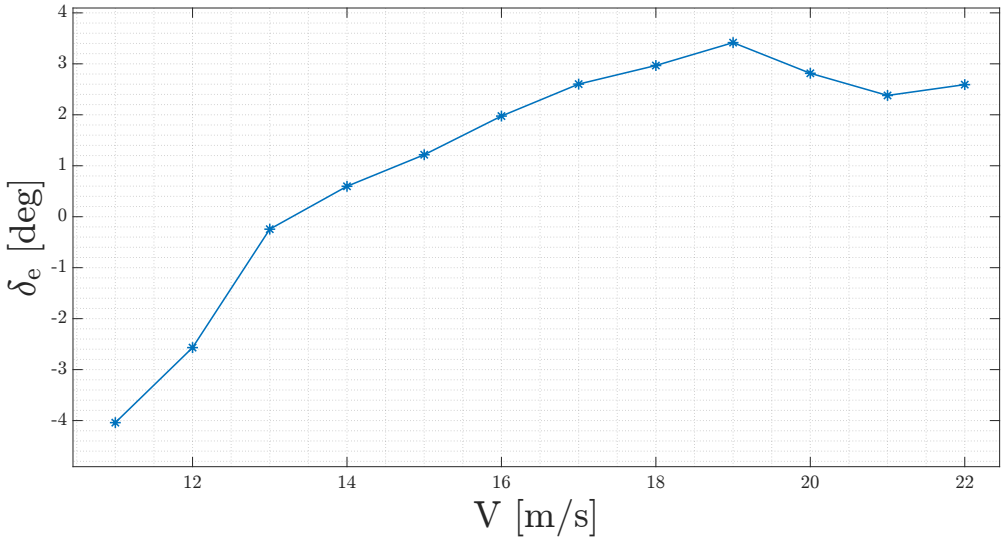

Figure 2.9: Elevator deflection at trim condition

2.4.1 Crash investigation

The flight date was June 12th. After the multi-rotor take-off, the aircraft successfully performed the transition to fixed-wing mode and flew for about 130 seconds in manual control mode with permanent stabilization, before crashing unexpectedly. Two frames from the recording of the crash are shown in Figure 2.12.

The investigation aimed to identify potential causes, such as:

- inadequate control action;
- electronic or mechanical failure;
- aeroelastic phenomena.

After thorough examination, all but the aeroelastic phenomena were ruled out as contributors to the event. Evidence has been found of the attempt of the pilot to roll back and pitch up to recover from the dangerous attitude assumed by the unresponsive aircraft; also the controller's set-points were consistent with an attempt to prevent the vehicle from crashing, the electronics did not present any malfunctioning from aftermath testing and none of the physical damage suffered pointed to anything that could have happened in flight.

Defined as a method of controlling the amount of power delivered to a device, Pulse Width Modulation (PWM) is commonly employed to control actuators. In this context, special attention has been given to comparing the aircraft's attitude with the PWM signals sent to the control surfaces. This comparison is critical since direct feedback on control surface deflection is unavailable. Additionally, the aircraft's attitude has been evaluated against the controller's set-points, providing

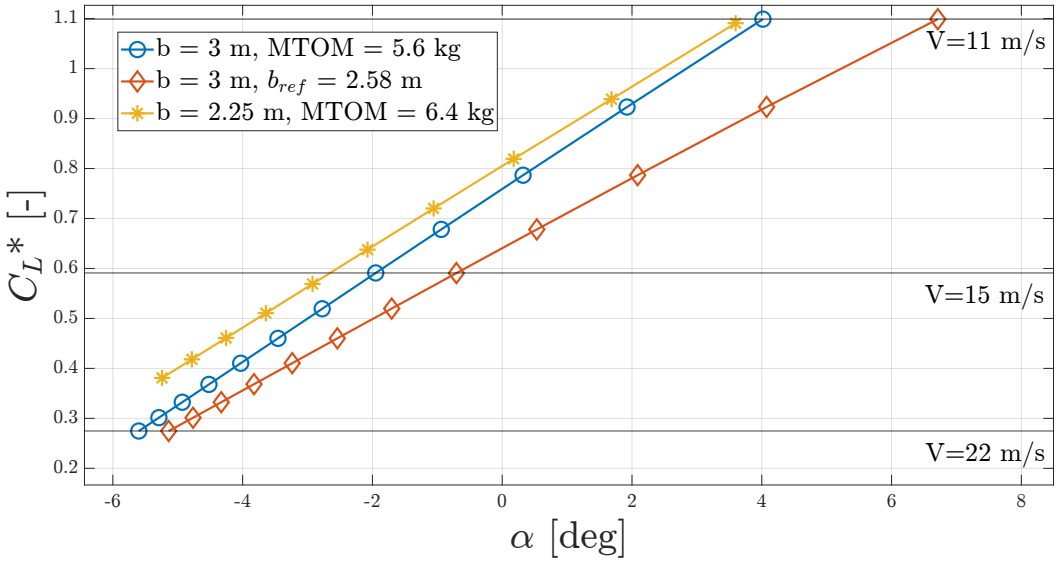

Figure 2.10: Lift coefficient at trim (C_L*) with respect to AoA; the horizontal lines represent notable airspeeds for comparison

valuable insights into its behavior. Notably, several observations emerge from this comparative analysis:

1. the aircraft presents a tendency to roll left on its own, tendency already highlighted by [2] through Simulink simulations, and associated with the slightly unstable spiral mode. Figure 2.12 shown the attitude of the aircraft instants before the crash and the extreme left bank angle is clearly visible. Figure 2.13, instead, shows the data that confirmed the idea: 1500 PWM is the neutral value for zero deflection of the ailerons, $PWM > 1500$ indicates a deflection to roll left, and $PWM < 1500$ indicates a deflection to roll right. It is easily seen that the mean value is around 1400 PWM, meaning there is a permanent slight deflection of the ailerons to counteract the tendency to roll left.

2. The tendency to roll left is also seen through an asymmetry in control effectiveness. An example can be seen from Figure 2.14a, that shows a right roll maneuver executed at an airspeed of around 16 m/s with $\Delta PWM = -400$ with respect to the neutral value, reaching a roll rate of about 25 deg/s. Figure 2.14b, instead, shows a left roll maneuver at around 13 m/s with $\Delta PWM = +300$ that reached about -40 deg/s of roll rate, despite the lower airspeed and with a deflection command much narrower than the one mentioned above. This behaviour was present during the entire flight, even though it was not intense enough to require active adjustments from the pilot.

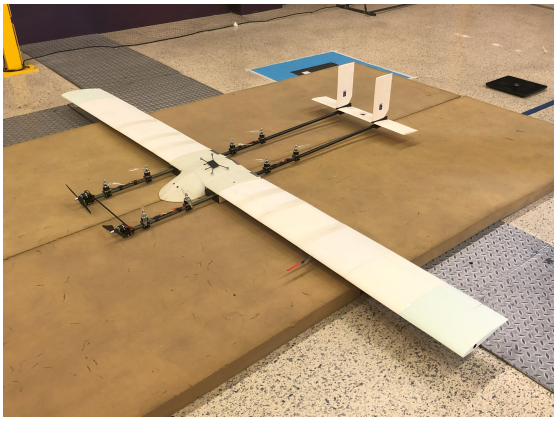

(a) Complete new aircraft.

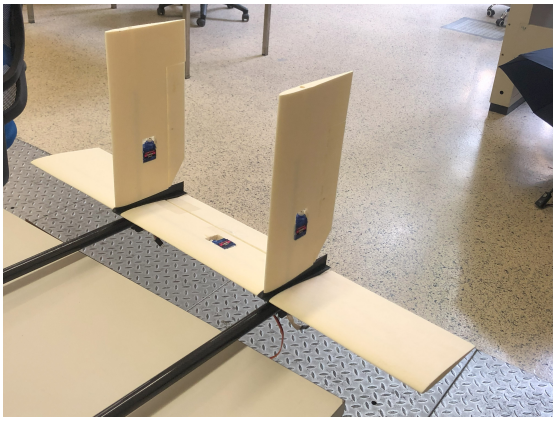

(b) Foam tail.

Figure 2.11: New wing and tail made out of hot wire cut foam

Figure 2.12: June 12th crash final moments; significant torsion can be observed at the wingtip.

3. At the time of loss of attitude and crash, the ailerons became completely ineffective and their control action was suspected to be reversed, idea reinforced by the continuously increasing roll rate that can be seen in Figure 2.16. The assumption is that, as shown in Figure 2.15, the increase in airspeed occurred after the last right turn caused the wings to enter control reversal.

Control reversal is a counter-intuitive aerodynamic phenomenon that can occur in aircraft structures, particularly in those with flexible wings like foam wings. When the ailerons are deflected to generate a rolling moment, this moment induces a wing twist or torsion due to the wing's flexibility. As the wing twists, the local angle of attack will vary and if the magnitude of the torsion is large enough, a rolling moment opposite to that initially intended by the aileron deflection can be produced. In essence, this means that the pilot's input to roll the aircraft in one direction could result in a roll in the opposite direction. This dynamic can be

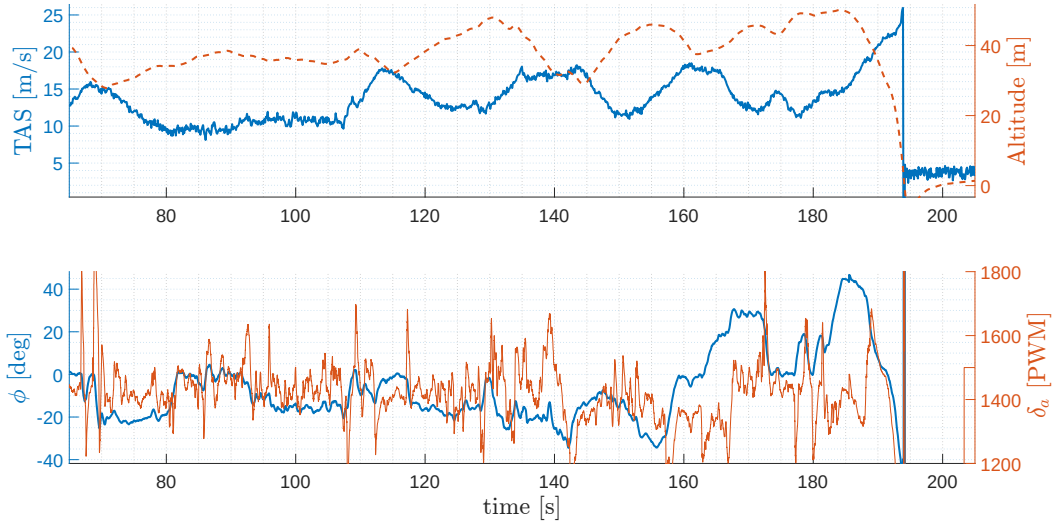

Figure 2.13: Airspeed vs altitude, and roll angle vs ailerons' PWM

well observed in Figure 2.16, in which, even though the aileron's PWM indicates a deflection to roll right, the roll rate p keeps increasing in a negative direction causing the negative bank angle seen in Figure 2.12.
Further investigation revealed also that the foam's flexibility caused it to deform permanently after supporting loads over time, which is a possible explanation to why control reversal has been encountered only after extended flight, even though similar speeds had been achieved earlier during accelerations and maneuvers.

2.5 Redesign and structural tests

2.5.1 Glass-fiber cladding of the wing

From the insights received in the previous section, it was evident that the wing needed modifications, and some adjustments to the tail were also in order. The initial structural design, referenced in [1], included a fiber cladding to reinforce the foam against bending and substantially enhance torsional stiffness. However, this design was altered due to technological constraints at that time. That concept was inspired by the UAV model developed by the University of Southampton, described in [6]. Their design featured a single layer of fine glass-fiber. For other aircraft models they designed, a heat-shrinkable aero-modeler wing film or thin Mylar was adopted, attached over the foam with spray-on contact adhesives. After reviewing the fibers available in in the departmental materials laboratory, a glass fiber cloth weighing $100\,\mathrm{g/m^2}$ was selected. This choice seemed suitable to grant the required properties when compared to the $20\,\mathrm{g/m^2}$ variant that the University of Southampton utilized.

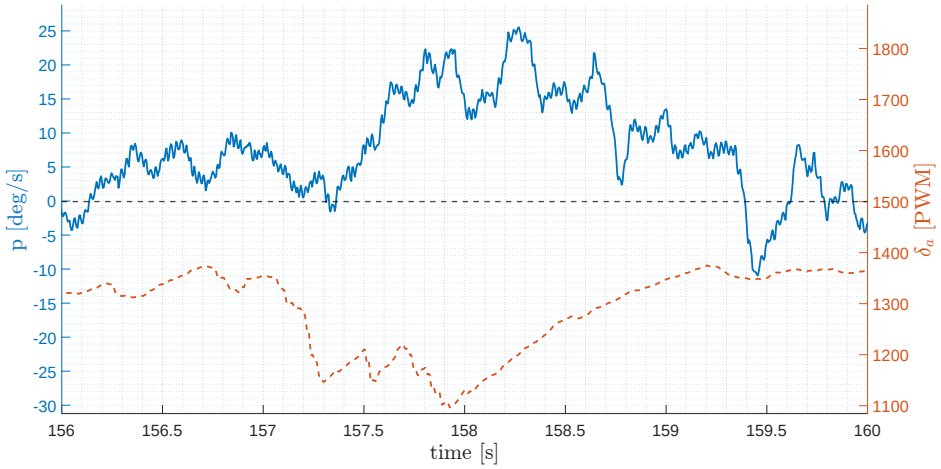

(a) Right rolling maneuver at 16 m/s exhibiting a sustained deflection.

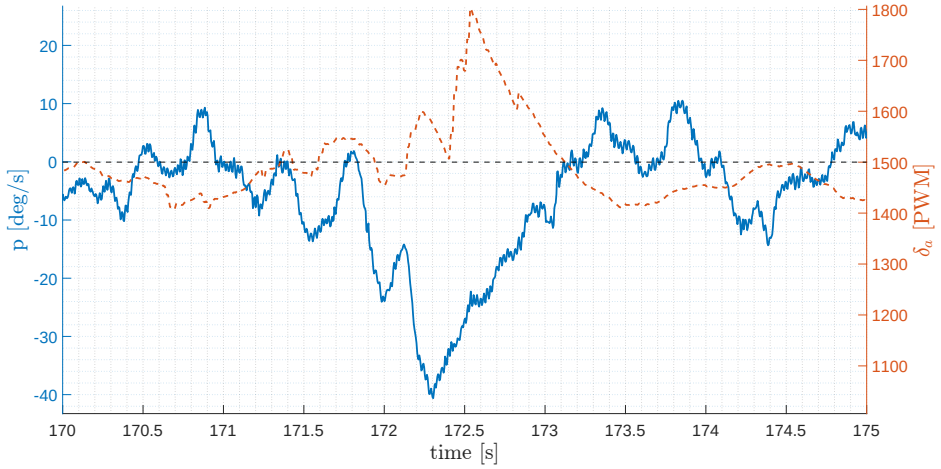

(b) Left rolling maneuver at 13 m/s exhibiting a narrow-peak deflection.

Figure 2.14: Asymmetric rolling behaviour comparison

The cladding process began by preparing the wing, ensuring it was clean and free of debris. As illustrated in Figure 2.17a, the glass-fiber cloth was trimmed slightly larger than the wing and laid out. A uniform mixture of the epoxy resin, seen in Figure 2.17b, was subsequently spread over the cloth. The foam wing is gently placed on this wetted cloth, which is then wrapped around the wing, taking care to conform it to the wing's contours and eliminate wrinkles. Using a flat-edged metal tool, any trapped air bubble between the cloth and the wing is expelled, starting from the center and moving outwards. After allowing the resin to cure for about a day, any excess cloth is trimmed off and the final wing obtained. The results of this procedure can be observed in Figure 2.18b and the difference in weight of the two semi-wings is summarized in Table 2.4.

A significant finding of the accident investigation was that the control surfaces, obtained by cutting the foam and attaching the horn for linkage with the servo

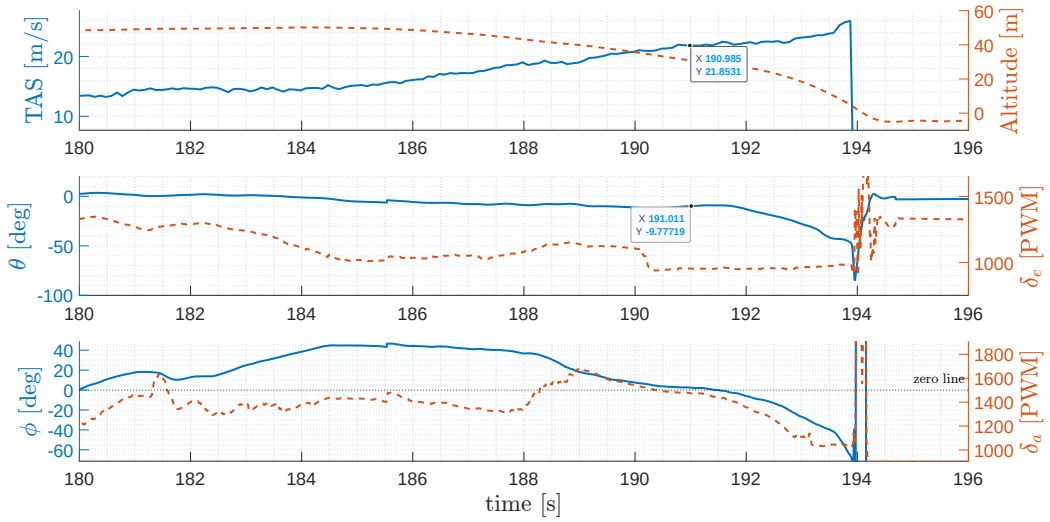

Figure 2.15: Synoptic view of the last rolling maneuver during the crash occurred on June 12th

Component	Foam wing	Glass-fiber cladded wing
Right wing	318 g	558 g
Left wing	361 g	586 g

Table 2.4: Comparison of wing weights before and after the glass-fiber cladding

motors, were overly flexible. This is despite this method being a popular practice in model aircraft manufacturing. For the ailerons, the glass-fiber cladding proved effective in solving the problem. For the elevator instead, a thin carbon fiber plate was attached to the bottom surface, rendering it stiffer and slightly enlarging its surface area. The surface area of the new elevator increased from $S_{elevator} = 0.0119\,\mathrm{m}^2$ to $S_{elevator} = 0.0156\,\mathrm{m}^2$.

2.5.2 Aeroelastic assessment

Once the upgrades were done, an evaluation of the modifications to the wing's properties and their effect on the aeroelastic concerns has been performed. For this purpose, a simple two-degree-of-freedom dynamic model of the wing has been considered, as suggested by [6], with assumptions of unswept wing and high aspect ratio. The model of the wing's motion is characterized by its vertical heave h and by its torsional rotation θ about the elastic axis, but restrained by two springs of stiffness K_h and K_θ, as represented in Figure 2.19.
The adopted model is linearized and the variables to be defined are: M the mass of the semi-wing, I the polar inertia about the elastic axis, L the aerodynamic lift force acting in the center of lift x_{ac} (assumed to be in front of the elastic axis) and x_{cg} the center of gravity lying behind it.

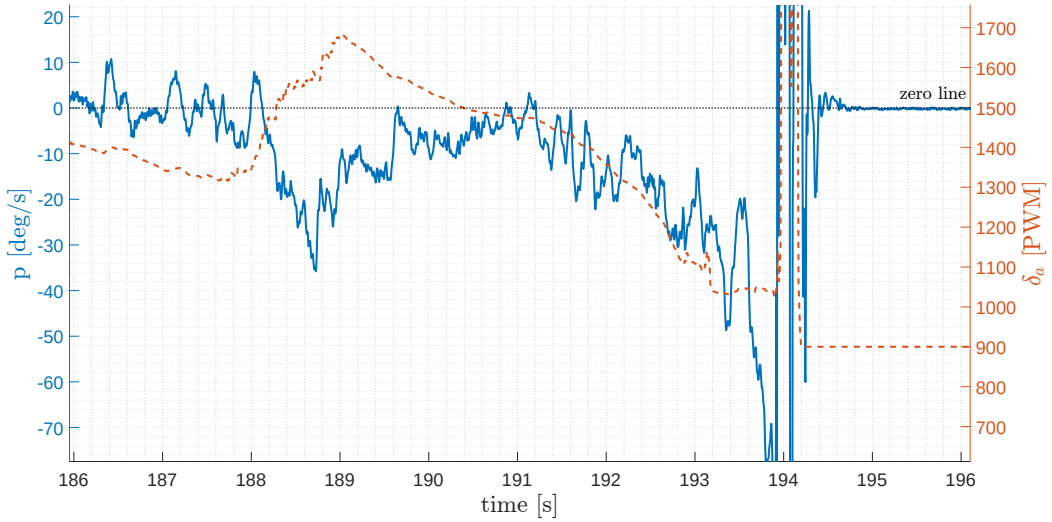

Figure 2.16: Roll rate vs ailerons' PWM during the crash

The equations of motion of the system can be defined as follows:

$$-L - K_h h = M\frac{d^2h}{dt^2} + x_{cg}M\frac{d^2\theta}{dt^2}\,; \tag{2.21}$$

$$Lx_{ac} - K_\theta\theta = I\frac{d^2\theta}{dt^2} + x_{cg}M\frac{d^2h}{dt^2}\,. \tag{2.22}$$

By assuming a steady-state thin airfoil behaviour, the lift of the semi-wing is taken to be simply proportional to the twist as

$$L = \frac{1}{2}\rho V^2\frac{S}{2}\frac{dC_L}{d\theta}\theta\,,$$

and can be substituted into Equations (2.21) and (2.22). Subsequently, assuming an harmonic solution to these equations with frequency ω and amplitude $\begin{bmatrix} h_0 \\ \theta_0 \end{bmatrix}$, the following matrix equation is obtained:

$$\begin{bmatrix} M\omega^2 - K_h & x_{cg}M\omega^2 - \frac{1}{4}\rho V^2 S\frac{dC_L}{d\theta} \\ x_{cg}M\omega^2 & I_\theta\omega^2 - K_\theta + \frac{1}{4}\rho V^2 S x_{ac}\frac{dC_L}{d\theta} \end{bmatrix}\begin{bmatrix} h_0 \\ \theta_0 \end{bmatrix} = \begin{bmatrix} 0 \\ 0 \end{bmatrix}\,. \tag{2.23}$$

By setting the determinant of this matrix equal to zero, the nontrivial solution to the equation can be found and, omitting the mathematical steps that are well explained in Chapter 14 of [6], the equation for divergence speed V_{div} is finally obtained as

$$V_{div} = \sqrt{\frac{K_\theta}{x_{ac}\pi\rho S/2}}\,. \tag{2.24}$$

(a) Glass-fiber cloth and foam wing (b) Epoxy resin and hardener mix

Figure 2.17: Materials and tools used in the cladding process.

A similar analysis can be performed by assuming the presence of a trailing-edge control surface which alters the lift of the section proportionally to its deflection δ, leading to the following definition of lift and moment coefficients:

$$C_L = C_{L_0} + \frac{dC_L}{d\theta}\theta + C_{L/\delta}\delta\,;$$

$$C_M = C_{M_0} + \frac{dC_M}{d\theta}\theta + C_{M/\delta}\delta\,;$$

where $C_{L/\delta} = \frac{dC_L}{d\delta}$ and $C_{M/\delta} = \frac{dC_M}{d\delta}$. This leads to the other equation of interest, the control reversal speed

$$V_{rev} = \sqrt{\frac{-K_\theta C_{L/\delta}}{\pi\rho MACC_{M/\delta}S/2}}\,. \tag{2.25}$$

At this point, the two control derivatives can be estimated through thin airfoil theory, that gives:

$$C_{L/\delta} = 2(\cos^{-1}(d) + \sqrt{(1-d^2)})\,; \tag{2.26}$$

$$C_{M/\delta} = 0.5(-aC_{L/\delta} + \cos^{-1}(d) - d\sqrt{(1-d^2)})\,; \tag{2.27}$$

where d is distance of the aileron hinge behind the mid-chord point as a fraction of the semi-chord and a is the distance of the aerodynamic center in front of the mid-chord point as a fraction of the semi-chord. In this case $d = 0.58$ and $a = 0.5$.

(a) Cladded wing during curing phase (b) Completed cladding

Figure 2.18: Progression of the glass-fiber cladding process

Wings structural tests

The last things needed to conclude the analysis are the two equivalent spring constants K_h and K_θ. To get them, the wing has been constrained by clamps to a workbench, a digital inclinometer has been attached at the wing tip to measure the twist angle while known weights were being gradually added. In addition, a ruler has also been placed close to the trailing edge supported by a tripod to measure the bending of the wing instead. The torsional stiffness K_θ is determined as

$$K_\theta = \frac{M}{\theta}\,, \tag{2.28}$$

where $M = m_w l$ is the torsional moment produced by placing the known weights mass m_w at a known distance l behind the elastic axis, as shown in Figure 2.20; θ instead is the angular displacement of the wingtip with respect to the root section measured by the inclinometer. The bending stiffness K_h instead, is determined as

$$K_h = \frac{P}{h}\,, \tag{2.29}$$

where P is the force applied on the elastic axis and h is the vertical displacement of

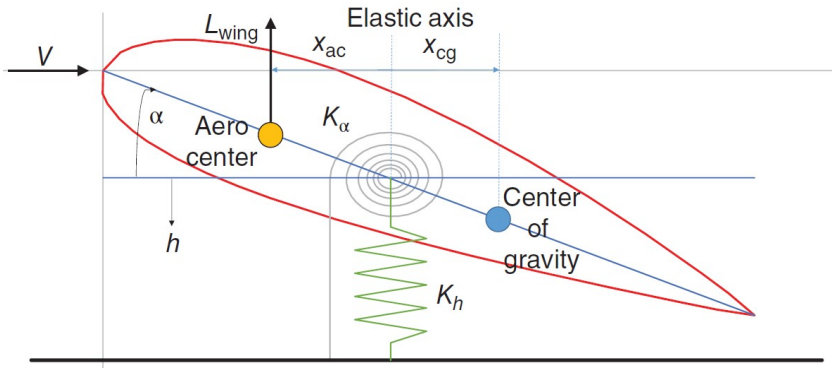

Figure 2.19: Aeroelastic two-degrees-of-freedom model of a wing (source [6])

the wingtip measured by the ruler. To perform the test, it is then required to know the position of the elastic axis. For this purpose, the wing was first loaded with the weights in several points along the chord, measuring the twist, and looking for the point that would produce none. In agreement with the expectation, the elastic axes of both the foam wing and the glass-fiber cladded wing coincided with the axis of the carbon fiber tube spar. This spar was strategically located a quarter chord distance from the leading edge, a crucial position considering that, according to the thin airfoil theory, the aerodynamic center is also located at this point.

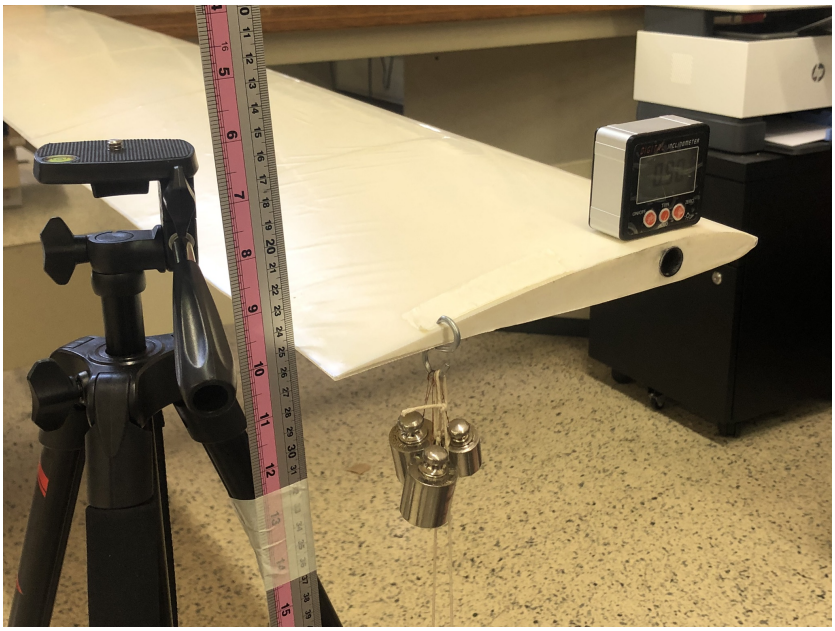

Figure 2.20: Structural test setup with ruler, weights and inclinometer

The bending stiffness test has been repeated three times on both wings by adding the five weights in random orders; a linear regression has then been applied to

each of the tests and the mean of the three angular coefficient of the straight lines taken as the equivalent spring constant, after appropriate dimensions processing. An example of the collected data for the cladded wing's bending test is presented in Figure 2.21.

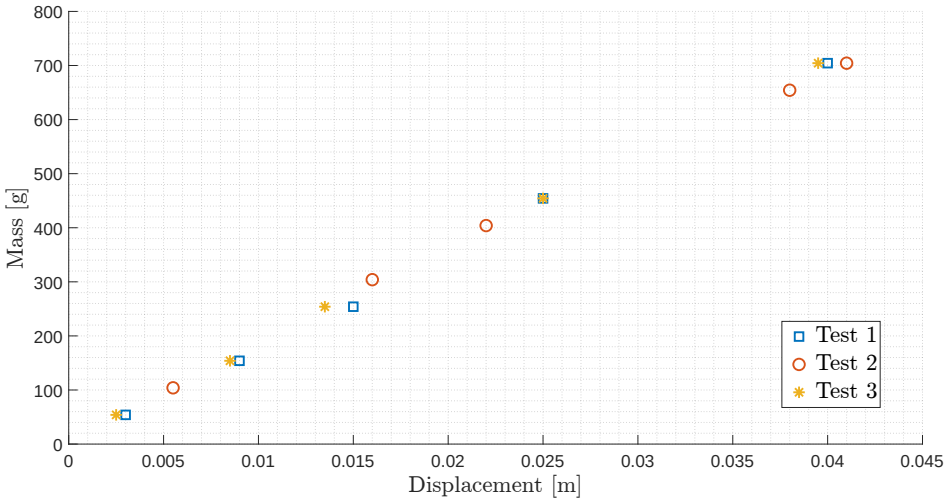

Figure 2.21: Cladded wing's bending test collected data

The torsional stiffness test was replicated three times for the foam wing and four times for the cladded version. The process involved incrementally and randomly adding and then removing the weights to increase the number of collected data points. The dataset of the torsional test performed on the foam wing is shown in Figure 2.22.

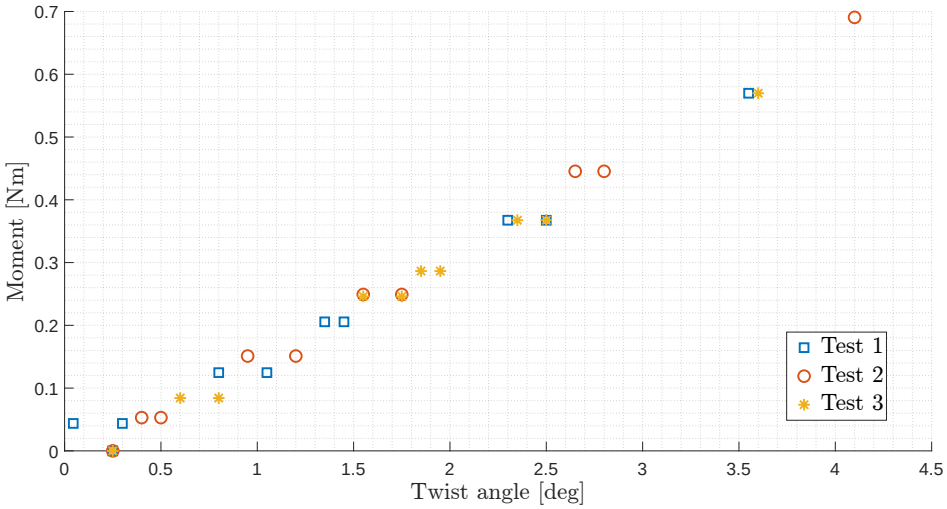

Figure 2.22: Foam wing's torsional test collected data

2.5.3 Final results

The results of the the tests and the analysis are here presented and commented: the cladding slightly increased the bending stiffness of the wing and significantly increased the torsional one, which was the main goal of the upgrade. The values can be observed in Table 2.5 and it can be noticed that the maximum twist angle measured got drastically reduced from 4.1 deg obtained with a torsional moment of 0.69 Nm on the foam wing to just 1.15 deg with 0.97 Nm on the cladded wing, demonstrating that the latter is nearly five times stiffer in torsion. From an aeroelastic point of view, the conclusions are two:

- in the context of this aircraft, divergence is precluded. Observing Equation (2.24), the term x_{ac} at the denominator represents the distance between the aerodynamic center and the elastic axis. It has been ascertained that these two points coincide. Specifically, the aerodynamic center is identified at 25% of the mean aerodynamic chord (MAC), precisely aligning with the wing spar's axis. This alignment results in x_{ac} being equal to 0.
- Control reversal speed instead, has been calculated by inserting the two values of torsional spring constants from Table 2.5 into Equation (2.25), and it has been confirmed that the former value $V_{rev} = 13$ m/s, critically close to the design cruise speed, has been moved by the upgrades to $V_{rev} = 29$ m/s, approximately 30% higher than the maximum speed.

Parameter	Foam wing	Glass-fiber cladded wing
K_h [N/m]	145.6	170.3
max h [cm]	4.8	4.1
K_θ [Nm/rad]	9.7	47.8
max θ [deg]	4.1	1.15

Table 2.5: Bending and torsional equivalent spring constants

One evident drawback of the cladding is the additional weight it introduces, as detailed in Table 2.4. Notably, the left wing is slightly heavier than the right one, discrepancy attributed to the presence of the Pitot tube. Moreover, this added weight results in an augmentation of the MTOM of the aircraft. While the VSP analyses initially utilized a value of 5.6 kg, the inclusion of the cladding increases the MTOM to approximately 6 kg (6070 g).
In conclusion, the cladding significantly enhanced the torsional stiffness of the wing, considerably pushing the control reversal speed beyond the aircraft's maximum speed. These results underline the potential of glass-fiber cladding as an effective upgrade for ensuring safe and efficient aircraft performance. Given its benefits, consideration will be given to integrating this material into the tail in future iterations, aiming for an overall more robust aircraft structure.

Chapter 3

Propulsive system

The propulsion system is fundamental to any aircraft, translating power into the critical thrust needed for flight. During the flight test campaign, it became evident that the UAV's propulsive components, specifically the propellers, struggled to adapt to the aircraft's increasing weight, as already noted in [3]. This chapter will be focused on the evolution of the FF propellers. It will start with an overview of the initial propeller, the GF 6x4.5, detailing its performance through the data collected during acceleration tests. Then, an upgraded version, the GF 9x4.3, will be discussed with a description of the motor test bench and the wind tunnel used to carry out experiments before their deployment, and the improvement they brought. Lastly, the newest propeller, the APC 10x55MR, purchased specifically for the required performance, will be presented, and through wind tunnel data and in-flight data, the leaps in performance and capability it introduced will be illustrated.

3.1 Propeller Gemfan 6x4.5

Initially, the forward motor's propellers selected for mounting were the GF 6x4.5 by Gemfan ([22]), implying a diameter of 15.24 cm (6 in) with a pitch of 11.43 cm (4.5 in). These propellers, paired with the electric motor KDE2315XF-965 by KDE Direct ([23]), were anticipated to provide the required thrust throughout the entire flight envelope by the initial design. However, at that time, wind tunnel data was not available and the only tests conducted were static, meaning the propeller's axial inflow effect was overlooked, resulting in a predicted thrust that was optimistic compared to the actual performance.
For propeller aerodynamics, axial inflow plays a significant role in determining propeller performance. When there is an axial inflow, the oncoming air moves parallel to the propeller's axis of rotation. This results in a reduced angle of attack for the propeller blades as illustrated in Figure 3.1, given that the relative velocity between the propeller and the inflow is diminished. As this angle

of attack decreases, so does the propeller's ability to generate lift, which directly translates to a decrease in thrust. This highlights the importance of understanding the operational environment and aerodynamic interactions when evaluating propeller performance. The increased weight of the aircraft and the substantial drag produced by the fuselage and vertical flight (VF) motors further aggravated the situation. These elements will be repeatedly emphasized in this thesis and will be discussed in detail in Chapter 5.

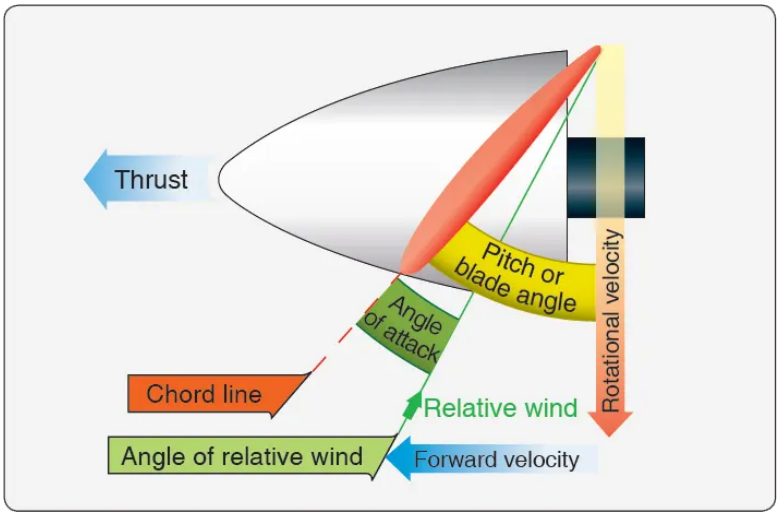

Figure 3.1: Simplified propeller aerodynamics (source [7])

The unsuitability of these propellers has been confirmed immediately at the beginning of the flight test campaign. As a mission progresses, the vertical take-off is succeeded by the transition phase, during which the aircraft speeds up from a hovering position to fixed-wing forward flight. This acceleration is fully provided by the thrust generated by the two frontal motors, with no contribution from the VF motors since the controller keeps the aircraft in level attitude.

During the campaign's early stages, the primary objective was ensuring the aircraft operated correctly throughout all flight phases before committing to fixed-wing data collection. This encouraged the team to adopt a cautious approach and conduct incremental tests. This meant that before completing a full transition, many accelerations have been first performed, interrupting the transition either by pulling the back-transition switch or by reaching the controller's preset transition time-out to abort it.

Figure 3.2 displays the true airspeed during one of the transitions. It can be noted that the transition lasted approximately 6 seconds, achieving a peak speed of about 9.5 m/s. Given that the target airspeed for completing the transition was set at 13 m/s, and the design cruising speed was 15 m/s, it became evident that these propellers were inadequate for sustaining the aircraft's flight.

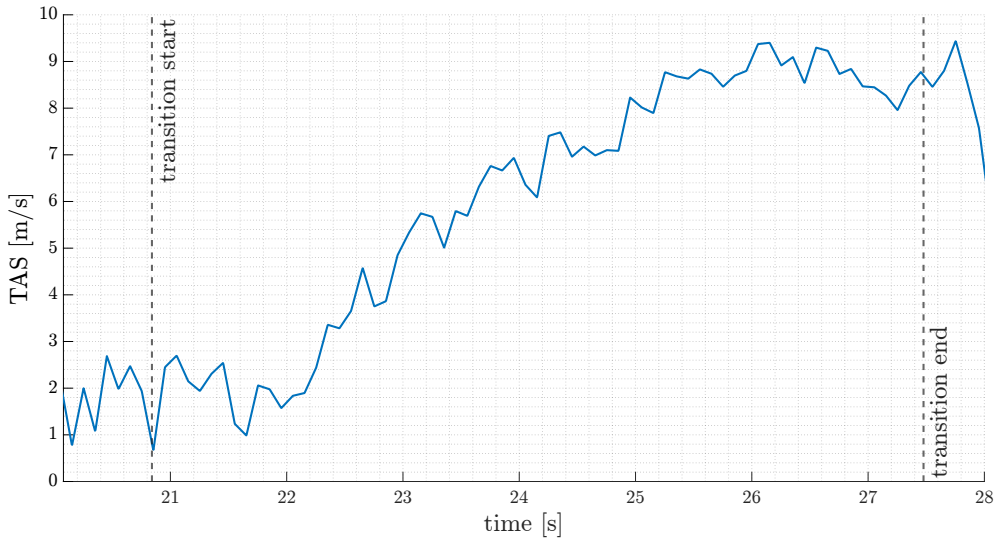

Figure 3.2: GF 6x4.5 acceleration during transition

3.2 Propeller Gemfan 9x43

Given the need of new propellers, the GF 9x43 have been selected as candidates thanks to their their increased diameter of 22.86 cm (9 in) and their immediate availability in the laboratory. To enhance the quality and accuracy of the predictions of the in-flight performance and to improve the existing Simulink model, wind tunnel tests have been carried out to get a complete characterization of the propellers behaviour with an axial inflow at different speeds.

3.2.1 Test bench modifications

A test bench, previously built in the laboratory as described in [2], served as the foundation for the motor testing activities. Central to its design is the robust main frame, crafted from 30 mm x 30 mm aluminum profiles. This frame not only forms the backbone of the bench but also provides a stable anchor for all components during testing. One of the main components is the set of strain gauge type load cells, complemented with the HX711 chip, a 24-bit analog-to-digital converter. With a measuring capability of up to 5 kg, these cells measure both motor thrust and torque. The setup is also capable of measuring the motor's angular velocity by detecting the blade's rotations through an optical tachometer, employing a laser-photodiode mechanism. To guarantee the accuracy of electrical measurements during tests, a power module is situated between the DC power supply and the motor's Electronic Speed Control (ESC). This module monitors both current and voltage parameters. An Arduino Uno board is used to collect data ([24]), then processed in Matlab. The unmodified setup can be seen in Figure 3.3.
To prepare it for use in the wind tunnel, some modifications were necessary to

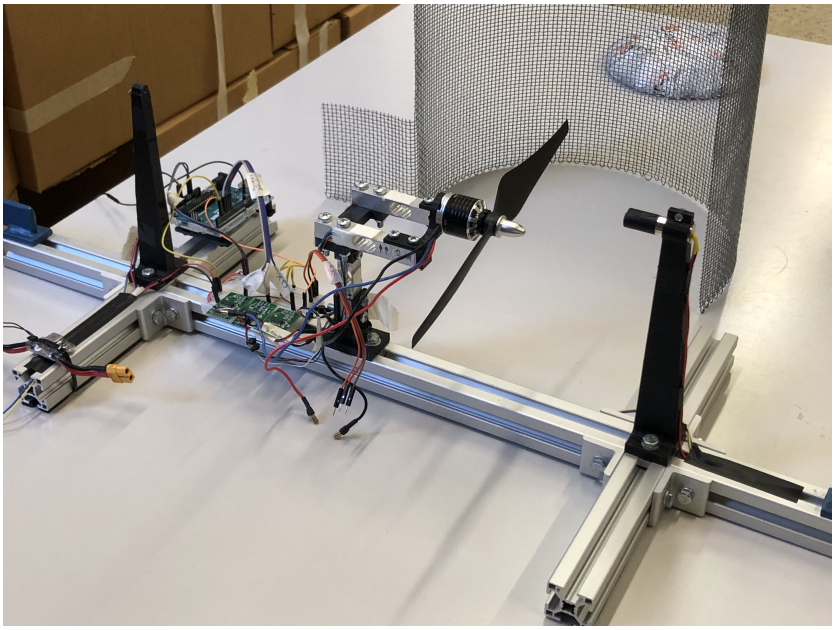

Figure 3.3: Motors test bench before modifications

facilitate easier installation within the chamber and to enable testing of larger propellers without the risk of contact with the lower part of the frame. These adjustments involved the removal of the laser tower positioned in front of the propeller, which would have been cause of great disturbance of the airflow. Additionally, the front part of the frame was shortened.

As a result of these changes, the optical tachometer had to be replaced with a new system for measuring angular velocity. The new approach involved utilizing a Hall effect sensor, which detects the presence and magnitude of a magnetic field using the Hall effect. This offered a more precise measure of angular velocity and minimized inaccuracies, that with the previous setup, were caused by misalignment between laser and photodiode during handling and mounting. Traditionally, Hall effect sensors are combined with small permanent magnets attached to rotating components for angular velocity measurement. However, in this study, a different approach was adopted. To minimize potential asymmetries on the motor casing's weight given their reduced size, and to avoid tampering with the results, the sensor was utilized to detect variations in the magnetic field generated directly by the motor's coils during operation. These variations generated voltage pulses in the sensor's output, which were directed to the dedicated pins on the Arduino Uno. By processing the frequency of these pulses and knowing the number of coils inside the motor, the motor's angular velocity was accurately determined as

$$\text{RPM} = \frac{\text{frequency of pulses}}{\text{number of coils}} \times 60\,. \tag{3.1}$$

The updated test bench is shown in Figure 3.11, depicting it mounted in the wind

tunnel's test chamber.

3.2.2 Wind tunnel tests

Politecnico di Milano is equipped with multiple wind tunnels of different dimensions. The one used to test the motors is "Galleria Sergio De Ponte", a closed circuit wind tunnel with a test chamber measuring 1 m in width, 3 m in length, and 1.5 m in height. It is powered by a 100 kW turbine, providing a controlled airflow environment with minimal turbulence and reaching maximum speeds of up to 55 m/s. Figure 3.4 illustrates a schematic overview of the wind tunnel plant.

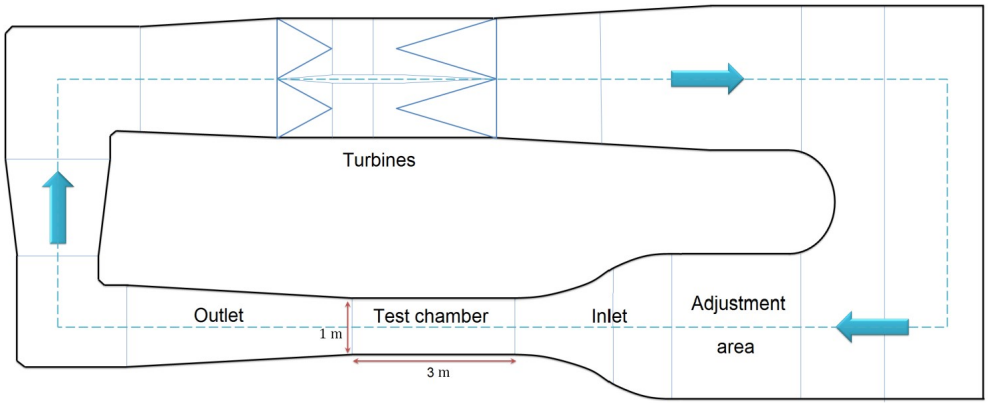

Figure 3.4: Wind tunnel schematic plant (source [8])

After positioning the test bench within the chamber and securing it using a tilting support, the experimental procedure was reviewed and approved by the wind tunnel staff that supervised the tests. The testing sequence involved examining every throttle point, ranging from 10% to 100% in 10% increments. For each throttle setting, the wind tunnel speed was adjusted, beginning from a static condition (0 m/s) and increasing up to 24 m/s in 3 m/s increments. This comprehensive approach, not only evaluated the entirety of the fixed-wing flight envelope airspeeds, but also captured airspeeds associated with the transition phase, allowing a thorough analysis of the propeller's operational range. Furthermore, for every throttle level, the wind tunnel's acceleration was interrupted if a negative thrust value was recorded, signaling that the propeller was out of its optimal efficiency range. The setup of the test chamber is illustrated in Figure 3.11 with an other propeller mounted. Note that the wires, and moving parts in general, have all been properly anchored before the tests.

A different approach considered was to fix the wind tunnel at a specific airspeed and then sweep through the throttle percentage range. While this method might have been more energy-efficient, it introduced complications during the initialization phase of the test bench at the start of a test. When transitioning

between throttle settings, the bench carries out a zeroing process by first shutting off the motors before powering them on again. In the presence of airflow during this stage, the propeller has been observed to windmill. This windmilling was accounted for in the zeroing, effectively nullifying the drag introduced by the airflow. Consequently, the chosen method was to maintain a constant throttle setting and vary the wind tunnel speeds.
The experimental procedure is presented in the following:

1. set the desired throttle value for the motor and power it;
2. start the data acquisition routine within MATLAB to record starting from the static test point;
3. activate the wind tunnel, starting at an airspeed of 3 m/s;
4. once a steady airspeed is achieved, collect wind tunnel data for a duration of 10 seconds with its dedicated acquisition system;
5. advance to the subsequent airspeed value, repeating the process from point 4, either until a negative thrust is detected or the peak airspeed is reached;
6. deactivate both the motor and the wind tunnel.

The tests were executed without any complications, and all settings functioned as anticipated. Data was systematically gathered from both the test bench and the wind tunnel, which were equipped with two separate acquisition systems.

3.2.3 Post processing and results

As anticipated, the collected data originated from two separate sources and was then divided into two sets. The first set was derived from the MATLAB data acquisition routine, which recorded parameters associated with the test bench, including generated thrust, motor torque, RPM, voltage, and current. In contrast, the second set was sourced from the wind tunnel data acquisition system, focusing on parameters such as airspeed, air temperature, and air density.

The initial step in post-processing involved aligning the timestamps of both data sets. Following this, the mean values of the parameters were extracted for the specific acquisition time windows. Subsequently, these parameters were coupled to derive the desired performance indexes. A significant aspect of this analysis was the development of a carpet plot, which was generated using Matlab's Curve Fitting Toolbox™. In selecting a fitting method, a polynomial approach was deemed most suitable, given its reliability in producing robust models. Following a trial-and-error methodology, a third-degree dependency was chosen for both airspeed and throttle. This combination provided an optimal balance, offering accuracy in

representation while maintaining a manageable level of complexity for seamless integration into subsequent analyses.
The derived polynomial took the form:

$$z = \mathrm{p}_{00} + \mathrm{p}_{10}\, x + \mathrm{p}_{01}\, y + \mathrm{p}_{20}\, x^2 + \mathrm{p}_{11}\, x\, y + \mathrm{p}_{02}\, y^2 + \mathrm{p}_{30}\, x^3 + \mathrm{p}_{21}\, x^2\, y + \mathrm{p}_{12}\, x\, y^2 + \mathrm{p}_{03}\, y^3\,, \tag{3.2}$$

where z represents the thrust in grams, x is the throttle percentage and y is the airspeed in m/s. The coefficients resulting from this fitting can be found in Table 3.1. A key metric for evaluating the quality of a fit is the coefficient of determination, $\mathcal{R}^2$. This metric measures the proportion of variance in the dependent variable explained by the independent variables in a regression model. Ranging between 0 and 1, an $\mathcal{R}^2$ value of 1 indicates a perfect fit, capturing all variability in the dependent variable. In contrast, a value of 0 suggests the model fails to explain any variance. For this study, the fit was considered satisfactory with $\mathcal{R}^2 = 0.999$. A visual representation of the fitting can be observed in Figure 3.5.

Coefficient	Value
p_{00}	39.87
p_{10}	2.143
p_{01}	-19.39
p_{20}	0.2525
p_{11}	0.336
p_{02}	-0.2447
p_{30}	-0.001201
p_{21}	-0.006872
p_{12}	0.001514
p_{03}	-0.004651

Table 3.1: GF 9x43 thrust data polynomial fitting coefficients

3.2.4 In-flight performance

Following the exhaustive analysis of the propeller's performance in the wind tunnel, an evaluation was conducted based on simple horizontal equilibrium to ascertain its suitability for mounting. The starting point was establishing equilibrium between thrust and drag, under the assumption of cruise conditions at a constant airspeed of 15 m/s:

$$T_{req} = \frac{1}{2}\rho V^2 S C_D\,. \tag{3.3}$$

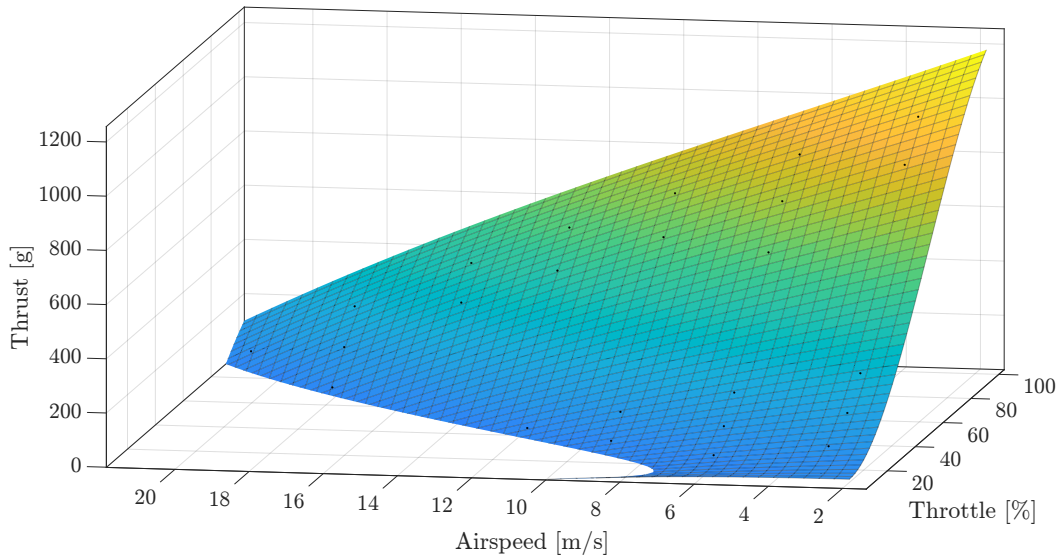

Figure 3.5: GF 9x43 wind tunnel data fit carpet plot

Assuming $S = 0.78$ m^2 (as in Table 2.1) and $C_D = 0.02564$ from the trimmed drag polar in Figure 2.8, the resulting equilibrium thrust in grams is $T_{req} = 273$ g. Referring to the fit illustrated in Figure 3.5, at 15 m/s with 65% of throttle, the thrust generated by a motor is approximately 133 g. Considering the drone has two FF motors, this thrust effectively doubles, summing up to a total of 266 g. The results indicated that the GF 9x43 propellers were capable of delivering enough thrust to sustain the aircraft's flight with still a margin of thrust for maneuvers or accelerations. Consequently, these propellers were mounted and tested in flight.

As for the previous propellers, the performed tests were accelerations during the transition phase. These new propellers showcased their capability, effectively facilitating not only the transition phase but also enabling sustained fixed-wing flight. Figure 3.6 shows the airspeed recorded during one of the acceleration tests. The improvement is immediately evident: the propeller managed to break through the transition airspeed set at 13 m/s, culminating in a successful fixed-wing flight. Subsequently, by analyzing Figure 3.7, it is observed that during the fixed-wing flight, the propeller supported various maneuvers, including cruise phases and turns, within an airspeed range spanning from 9 m/s to a top of approximately 18 m/s. A crucial observation from the collected data was the pilot's need to maintain full throttle for the majority of the flight. This finding suggested that, despite the successful flight, there was a potential need for more powerful propellers.

3.3 Propeller APC 10x55MR

Market research was conducted to identify an alternative to the previous propellers and equip the aircraft with more capable ones. The selection criteria were:

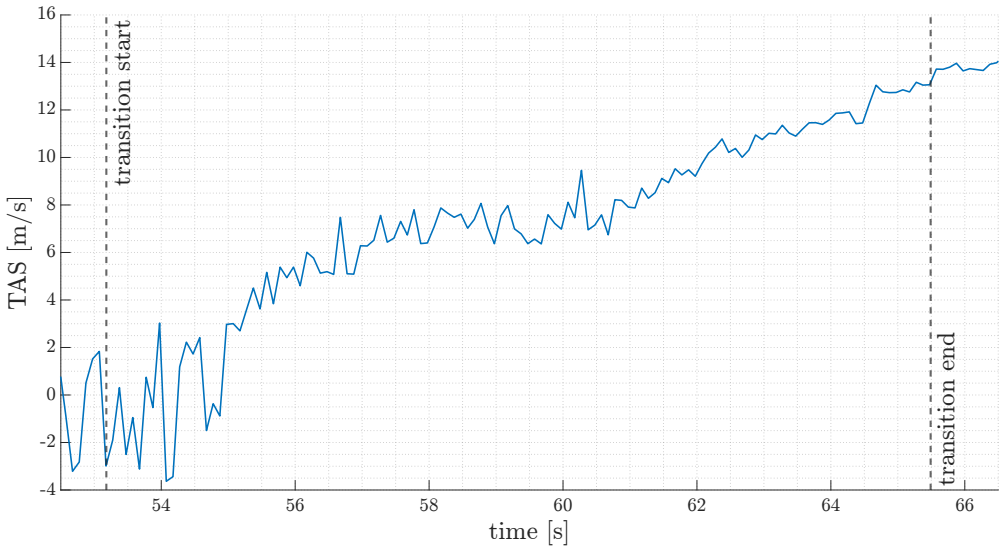

Figure 3.6: GF 9x43 acceleration during transition

- size range: 22.86 cm (9 in) to 27.94 cm (11 in) to prevent interference between propellers due to the fixed motor booms distance;
- immediate availability of both pusher and puller versions, considering the counter-rotating configuration of the FF motors;
- manufactured by APC, chosen for the comprehensive performance data available on their website.

3.3.1 Propeller selection

Five candidate propellers, outlined in Table 3.2, were identified in line with the criteria on the usual components provider website used by the laboratory.

Model	Diameter [cm]	Pitch [cm]	max RPM
APC 9x47 Slow Flyer	22.86	11.94	7200
APC 9x6 Thin Electric	22.86	15.24	16670
APC 10x45 Multi-rotor	25.40	11.43	10500
APC 10x55 Multi-rotor	25.40	13.97	10500
APC 11x47 Slow Flyer	27.94	11.94	5900

Table 3.2: APC candidate propellers

Notably, these models not only had different diameters and pitches, but also belonged to different categories. Following, a general description:

- Slow Flyers (SF): designed to operate at low RPMs, producing substantial thrust even at lower speeds.

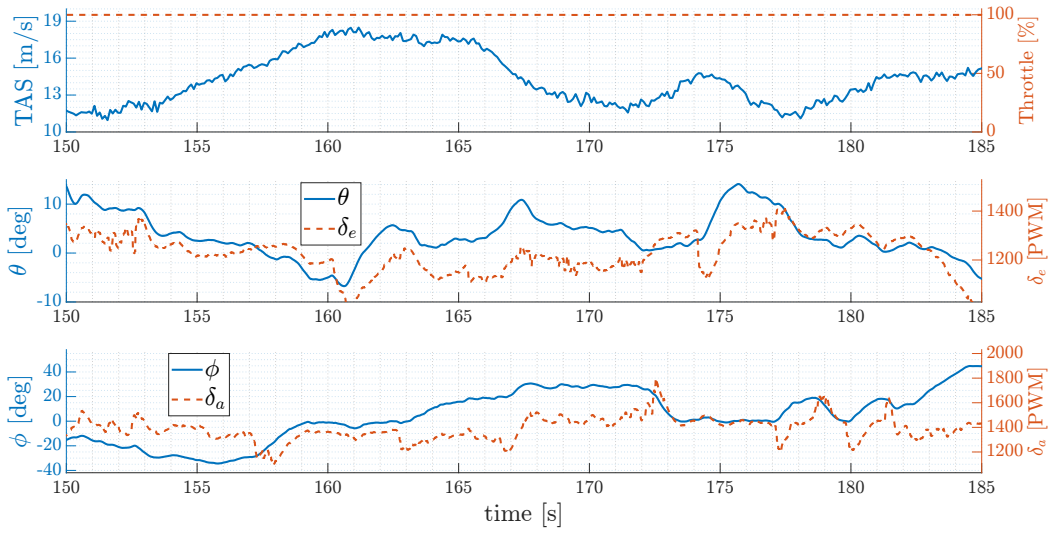

Figure 3.7: GF 9x43 performance during fixed wing flight

- Thin Electric (E): designed primarily for electric motors. Compared to Slow Flyers, they are thinner and operate efficiently at higher RPMs. They are suitable for sport planes and other types of aircraft that require higher speeds.
- Multi-rotor (MR): designed for multi-rotor aircraft. They are optimized to provide stability and efficiency, crucial for hover and vertical flight seen in drones.

Each of the categories also had different RPM limits given their different applications. Defining D as the propeller's diameter in inches, APC's safety recommendations are:

- Slow Flyer (SF): $RPM_{max} = \frac{65000}{D}$.
- Thin Electric (E): $RPM_{max} = \frac{150000}{D}$.
- Multi-rotor (MR): $RPM_{max} = \frac{105000}{D}$.

These are the formulas used to obtain the RPM limits reported in Table 3.2. APC also offers an archive of performance data files on their website ([25]). The propeller blade loads and resulting performance data are generated using a specialized computational method that is based on Vortex theory and integrated in a proprietary analysis software. In addition, a comprehensive set of wind tunnel experimental data on APC propellers can be found on the University of Illinois Urbana-Champaign (UIUC) Aerospace Engineering website ([26]). To ensure reliability, performance data from APC was cross-referenced with the experimental data from UIUC, and the datasets showed a high degree of correlation. The APC

data has then been used for a comparison between the candidate propellers, given the lack of experimental data from UIUC on the two listed multi-rotor models. The first comparison was between the generated thrust against the airspeed. As visible from Figure 3.8, the APC 11x47SF was dominant with an outstanding 2.7 kg of static thrust against the 1.8 kg of the APC 10x55MR, which was the second most performing propeller. Moreover, the range of airspeed of interest was highlighted, and also withing that range, these two propellers were the best performing, keeping the lead up until about 25 m/s, where they cross paths with the APC 9x6E, optimized for higher airspeeds.

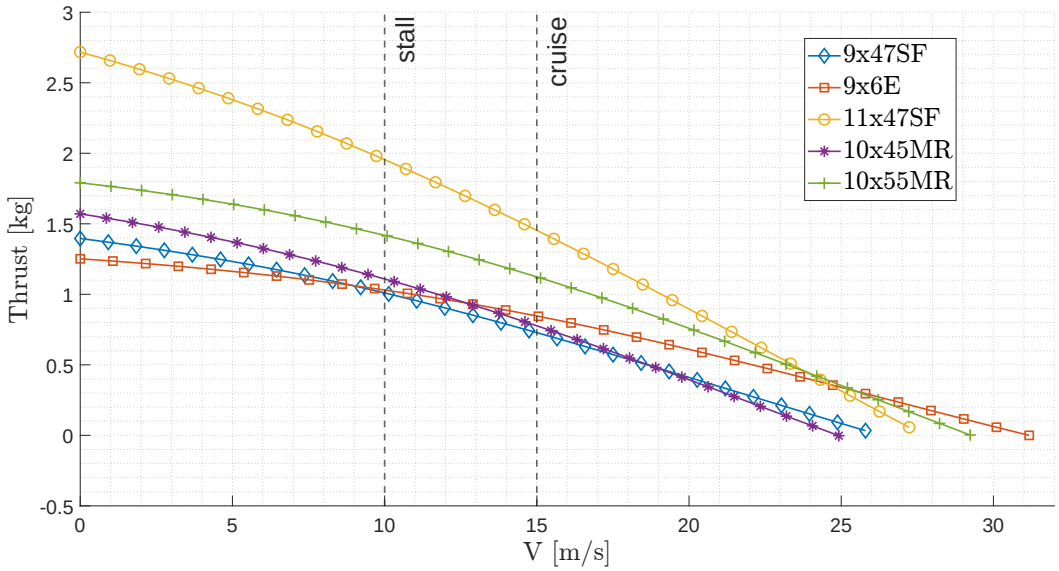

Figure 3.8: Thrust comparison of candidate propellers

Proceeding with the analysis, the efficiencies have been compared as illustrated in Figure 3.9. According to UIUC, the propulsive efficiency of the propeller is expressed as

$$\eta = \frac{C_T J}{C_P}\,, \tag{3.4}$$

where C_T and C_P represent the thrust and power coefficients, respectively, and J is the advance ratio. Introducing n, revolutions per second, these coefficients are defined as follows:

$$C_T = \frac{T}{\rho n^2 D^4}\,, \tag{3.5}$$

$$C_P = \frac{P}{\rho n^3 D^5}\,, \tag{3.6}$$

$$J = \frac{V}{nD}\,. \tag{3.7}$$

The efficiency η provides insight into the ability of the propeller in transforming the input power into forward motion. A higher efficiency indicates that for the same power, more thrust is generated by the propeller.
It can then be observed in Figure 3.10 that all of the propellers performed similarly around cruise speed, but quickly diverged at higher speed. Though the APC 11x47SF was leader in thrust, its efficiency was found to be suboptimal, particularly at speeds below 20 m/s. The APC 10x55MR instead was highly efficient up to 25 m/s, accompanied by the APC 9x6E which is the overall most efficient of the candidates. Both these last two propellers had great efficiencies over the operational range of the aircraft, even though the 10x55MR generated more thrust and so far was considered the better choice between the two.

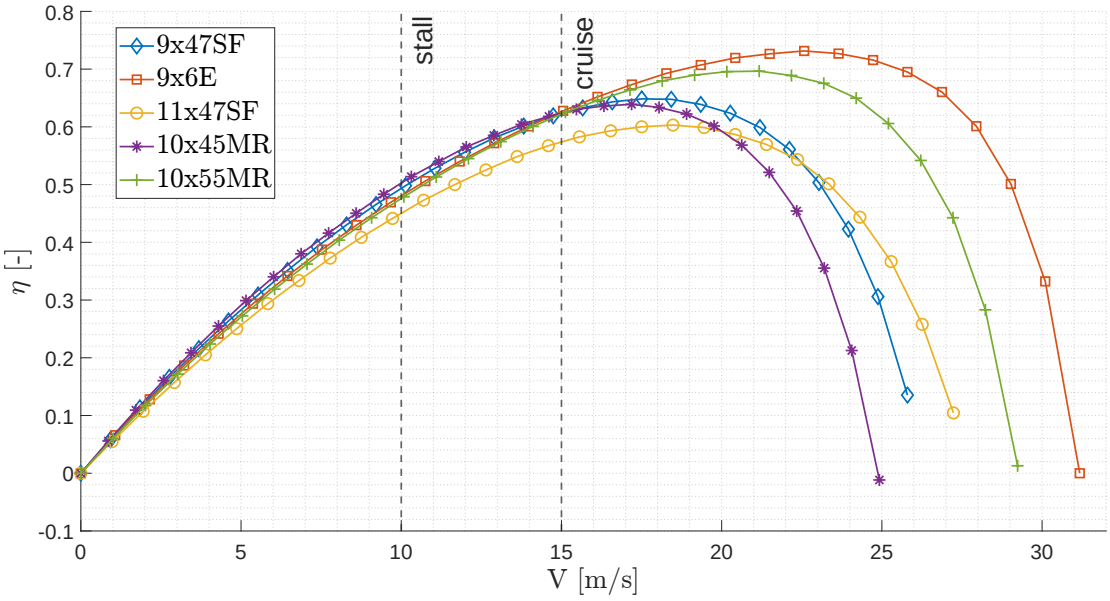

Figure 3.9: Efficiencies comparison of candidate propellers

Summarizing, the APC 11x47SF was the most thrusting propeller but with the least overall efficiency. Thrust-wise, the APC 10x55MR was the immediate competitor with also a great efficiency over the complete flight-envelope airspeeds, similarly to the APC 9x6E, which had the downside of not generating as much thrust. The other two propellers instead, generated similar thrust to the APC 9x6E but had efficiencies that began to drop at around 17 m/s, therefore were less appealing.

The last key parameter to be studied was the electrical current consumed by these propellers. The currently mounted ESCs are the KDEXF-UAS35, which can withstand a maximum continuous current of 35 A, and therefore set an upper limit to the power that the propulsive system can absorb. Considering that the batteries are 4S, meaning they are built with four cells of 3.7 V each connected in series, for a total nominal voltage of $V_{batt} = 14.8$ V, and that the power, P,

absorbed by each of the propellers is available in the data, the current I has been calculated as

$$I = \frac{P}{V_{batt}} . \tag{3.8}$$

This led to the result illustrated in Figure 3.10: while the APC 11x47SF stood out in thrust generation, its current consumption has been deemed too high and with little margin from the limits, rendering it unsuitable. Among the remaining candidates, the APC 10x55MR drew the highest current, yet remained well within the acceptable bounds.

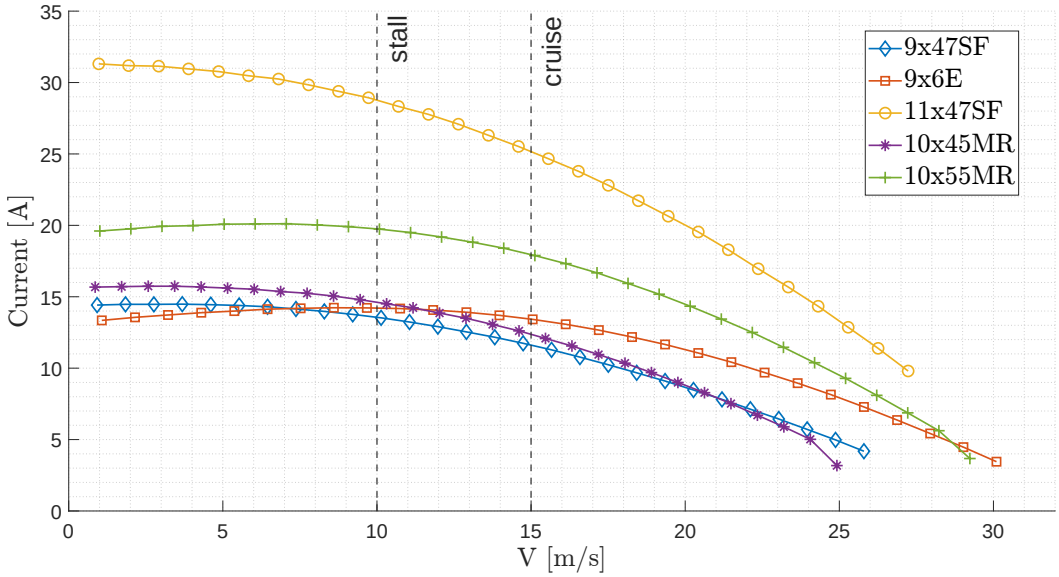

Figure 3.10: Absorbed current comparison of candidate propellers

In light of detailed evaluations on multiple fronts, the APC 10x55MR was identified as the most suitable propeller for the specific application. Referring back to Table 3.2, the suggested RPM limit for this propeller was about 10500, which the wind tunnel tests discussed in Section 3.2.2 confirmed to be adhered to in all operational scenarios.

3.3.2 Wind tunnel tests

Given the availability of the wind tunnel, also this new propeller has been tested deploying the same procedure detailed in Section 3.2.2. Figure 3.11 illustrates the setup of the tests, which was the same as the previous one.
At all throttle values from 0% to 100%, with increments of 10%, all the airspeeds ranging from 0 m/s to 24 m/s have been tested with increments of 3 m/s. Following data collection, a third-degree polynomial with two independent variables was employed for data fitting, adhering to the form presented in Equation (3.2).

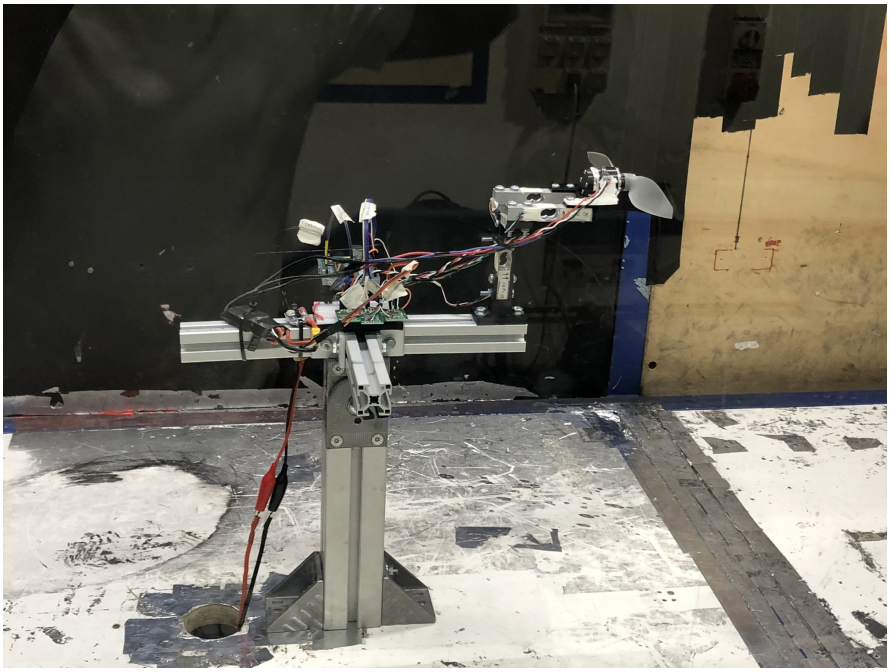

Figure 3.11: Test bench configuration with the APC 10x55MR mounted for wind tunnel testing

The graphical representation of this polynomial fit can be viewed in Figure 3.12 while the fitting coefficients are reported in Table 3.3; the quality of the fit was considered satisfactory with a coefficient of determination $\mathcal{R}^2 = 0.9847$.
An analysis of the test outcomes revealed a better performance of the new propeller in comparison to its predecessor, the GF 9x4.3. Specifically, with a throttle set at 100% under static conditions, the new propeller produced a thrust of approximately 1600 gf against the peak thrust of 1150 gf of the GF 9x4.3. Increasing the airspeed to 15 m/s, which is the design cruise speed, both values decreased to 700 gf and 470 gf respectively. This data underscores an approximate thrust enhancement of 40% to 50% with the new propeller depending on flight conditions.

3.3.3 In-flight performance

Following the wind tunnel tests that validated the propeller's enhanced performance, in-flight tests were conducted. The benefits of these propellers in flight conditions were clear: the transition phase duration and spatial extent were noticeably shortened. This allowed the aircraft to swiftly transition into fixed-wing flight, analysis that will be discussed thoroughly in Chapter 4.
Figure 3.13 provides insight into a segment of a test flight. In comparison to the previous GF 9x4.3, it highlights that maneuvers and trimmed flight legs are efficiently executed using throttle values predominantly between 60% and 80%.

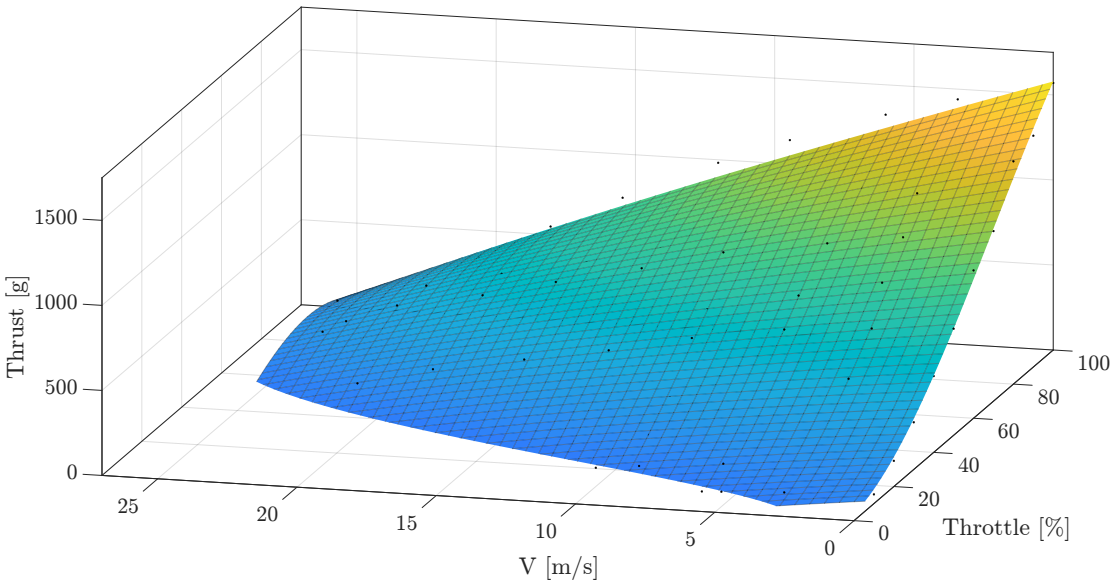

Figure 3.12: APC 10x55MR wind tunnel data fit carpet plot

Furthermore, electrical consumption during these flights was also analyzed. During the majority of the test flight, the witnessed current absorption was between 7 A and 20 A, values perfectly in line with the data from APC used during the preliminary comparison. Figure 3.14 details the voltage and current metrics for both batteries during the flight. A singular peak is evident at about 260 s, where one battery reached 24 A and the other 27.5 A, slightly surpassing the ESC's standard limits. Nonetheless, this did not compromise flight safety given that the ESC is designed to withstand electrical currents up to 35 A for brief periods without incurring damage or reducing its operational lifespan.

In conclusion, the APC 10x55MR propeller effectively addressed challenges iden-

Coefficient	Value
p_{00}	32.03
p_{10}	-1.872
p_{01}	5.013
p_{20}	0.3017
p_{11}	-0.8722
p_{02}	-0.1096
p_{30}	-0.001624
p_{21}	0.003064
p_{12}	0.006345
p_{03}	-0.02751

Table 3.3: APC 10x55MR thrust data polynomial fitting coefficients

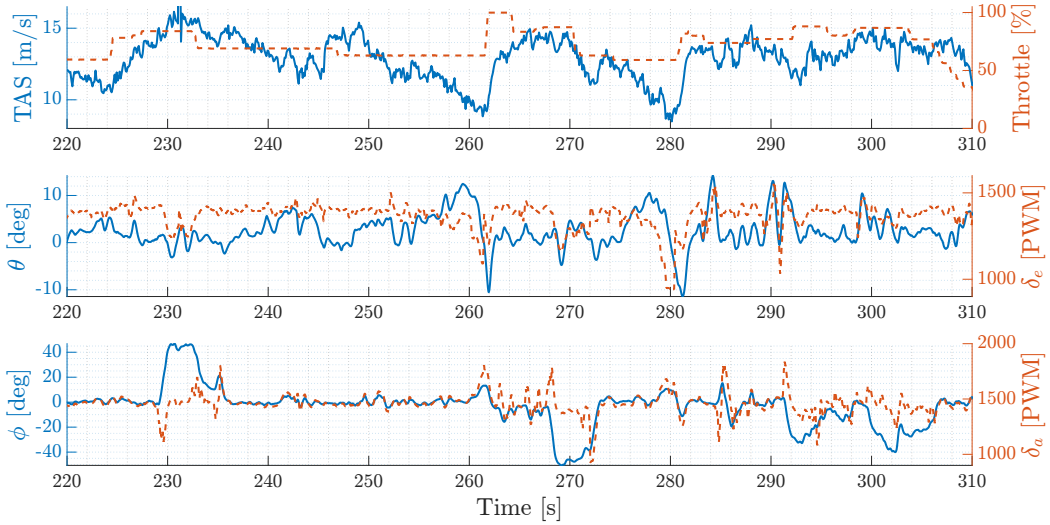

Figure 3.13: APC 10x55MR performance during fixed wing flight

tified during the early stage of the flight campaign, proving its suitability for the propulsion system. A more in-depth analysis about the aircraft's performance concerning the generated thrust is reserved for Chapter 5.

3.4 Additional experiment

In conjunction with the GF 9x4.3 wind tunnel tests detailed in Section 3.2.2, making use of the support's ability to tilt about its pitch axis, the vertical motors' configuration was also tested. Specifically the tested components were:

- motor: KDE2315XF-2050 by KDE Direct ([23]);
- ESC: KDEXF-UAS55 by KDE Direct;
- propeller: GF 7x4.2 by Gemfan ([22]).

Similarly to the case of a propeller with an axial airflow, in a non-axial airflow scenario, complexities arise. Varying local angles of attack along the blade span, in increased risk of stall, and unpredictable vortex generation can be observed. The expected net effect is a reduced thrust generation but, according to [27], less pronounced than in the axial case.
The setup of the test is shown in Figure 3.15: the test bench was rotated 180 deg about its vertical axis. Subsequently, after a 90 deg rotation of the tilting support about its pitch axis, the propeller was pointing upwards and was the first components facing the undisturbed airflow.

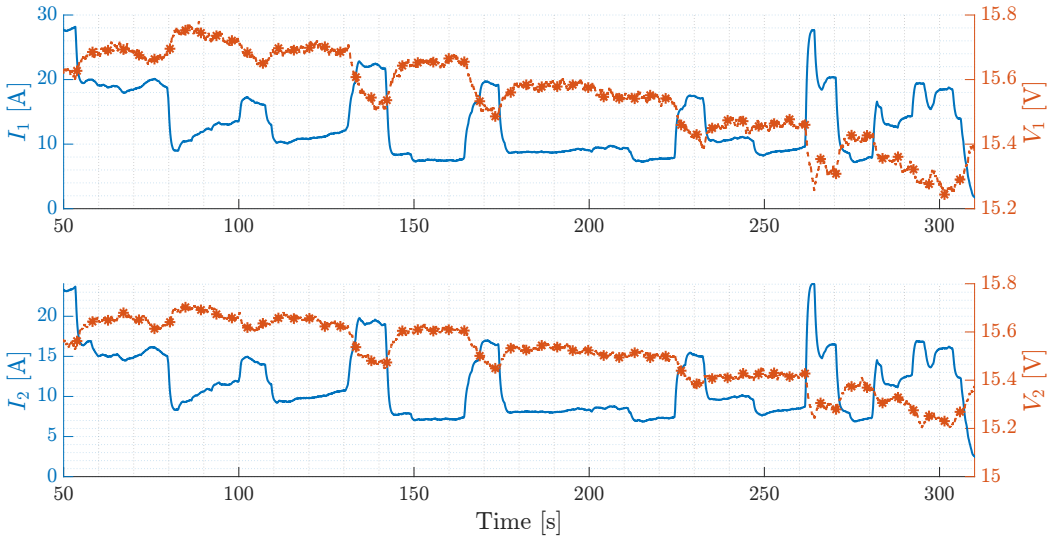

Figure 3.14: APC 10x55MR batteries consumption

Given that the multi-rotor portion of a flight mission is small, including take-off, vertical climb, final vertical descent and landing, the vertical motors operate within a limited airspeed range. With this in mind, the procedure tested throttle values from 10% to 100% in 10% increments, adjusting the wind tunnel speed from static condition to 14 m/s in 2 m/s increments. This procedure captured the thrust trend of the 8 vertical motors from hovering to the end of the transition phase, when they are turned off, as the lift is fully provided by the wing.
Following the same procedure detailed in Section 3.2.3, and using the same polynomial presented in Equation (3.2), the collected data has been processed. The results have then been used to refine the Simulink model of the aircraft, aligning it closely to the real behaviour. The coefficients of the fit are reported in Table 3.4, with a coefficient of determination equal to $\mathcal{R}^2 = 0.9963$, indicating its good quality, while the graphical representation of the fit is shown in Figure 3.16.
Notably, unlike the axial flow configurations, the increase in airflow speed initially causes a reduction in the produced thrust. As the airspeed gets close to the ending portion of the test range the thrust recovers slightly, effect that is emphasized at higher throttles. While it was difficult to pinpoint the exact dynamic that caused the behaviour, it has been confirmed that the effect of the airflow, in the studied speed range, is limited and does not cause a critical reduction in thrust.

3.5 Temperature's effect on thrust

The most recent wind tunnel tests, conducted on the APC 10x55MR in a horizontal configuration and on the GF 7x4.2 in the vertical configuration, took place

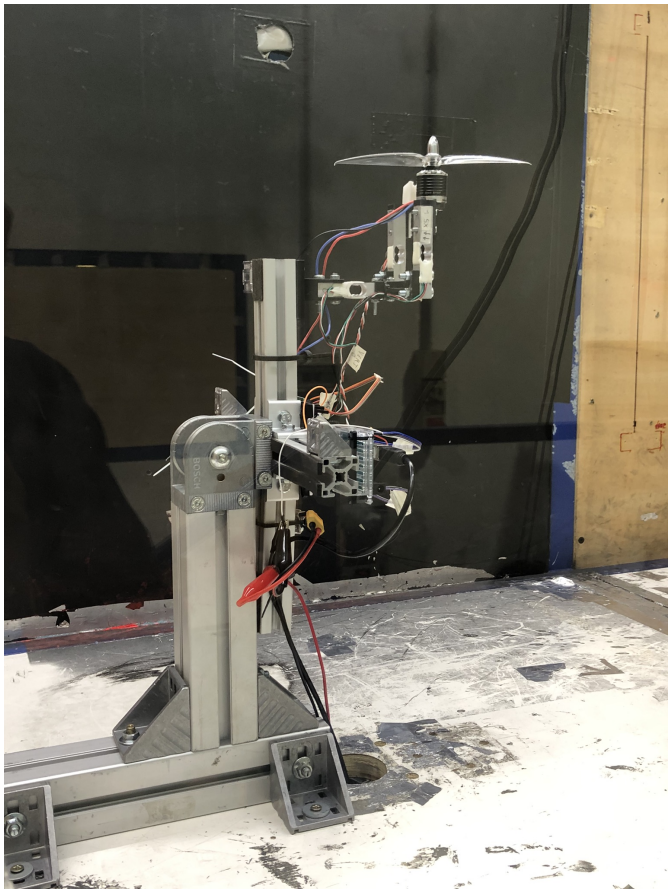

Figure 3.15: Vertical motors setup for wind tunnel testing (airflow from right to left)

in July with an average test chamber temperature of 26°C. Flight testing, as subsequently discussed in Chapter 5, occurred in two distinct periods. The first occurred in the late days of July, with a maximum outside air temperature of approximately 32°C, while the second took place at the end of September and the beginning of October, with a minimum outside air temperature of 23°C. Considering the crucial significance of accurately estimating the thrust produced during flight, a comprehensive study on the impact of temperature has been conducted to assess the need for correction.

3.5.1 Mach number

The impact of temperature variation on thrust estimation involves several aspects, with the first analysis focusing on the variation of the propeller's local Mach number, directly proportional to the flight Mach number. By employing the

Coefficient	Value
p_{00}	-70.52
p_{10}	12.15
p_{01}	15.68
p_{20}	0.1354
p_{11}	-0.4846
p_{02}	-1.184
p_{30}	-0.001125
p_{21}	-0.0008033
p_{12}	0.02267
p_{03}	0.05008

Table 3.4: Vertical configuration thrust data polynomial fitting coefficients

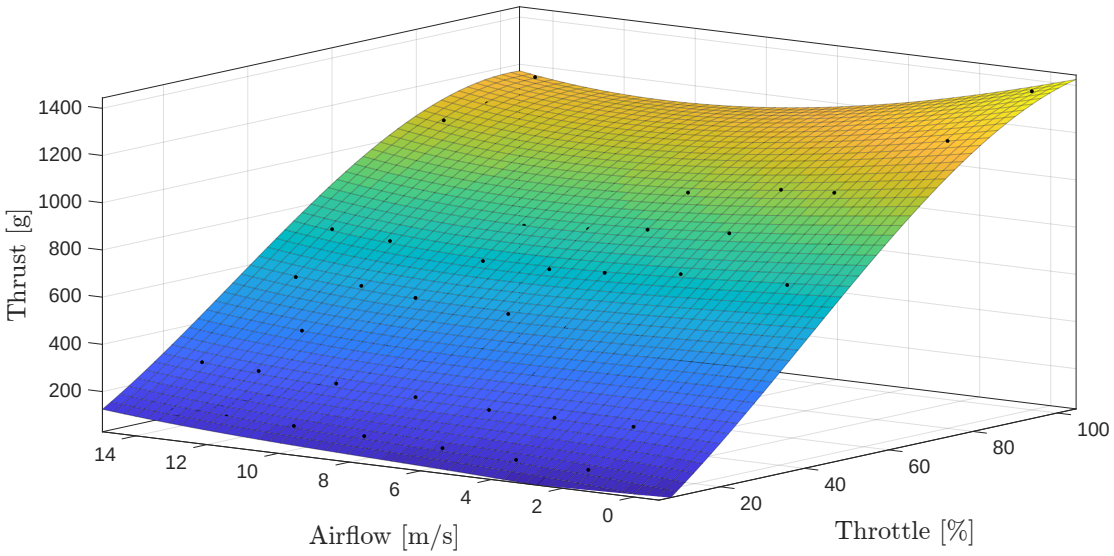

Figure 3.16: Vertical configuration wind tunnel data fit carpet plot

definition of Mach number:

$$M = \frac{V}{\sqrt{\gamma R \Theta}},$$

where V is the airspeed, γ is the ratio of specific heat (assumed to be 1.4 for perfect gases), and R is the specific gas constant (equal to 287.05 J/(kg·K) for ideal gases), the ratio between Mach numbers at two different temperatures can be calculated. This analysis considers a worst-case scenario where the temperatures are 10°C apart. This approach is chosen to assess the magnitude of the influence, considering the maximum deviation of 6°C observed between the airfield and the wind tunnel. The calculation is expressed as:

$$\frac{M_2}{M_1}|_{\Delta\Theta=10} = \frac{\frac{V}{\sqrt{\gamma R\Theta_2}}}{\frac{V}{\sqrt{\gamma R\Theta_1}}} \,. \tag{3.9}$$

The result of Equation (3.9) is $\frac{M_2}{M_1} = 1.0165$. This indicates that the Mach number varies by 1.65% with a temperature difference of 10°C. For the purposes of this study, this variation is considered negligible.

3.5.2 Reynolds number

The subsequent analysis focuses on the impact of temperature on Reynolds number variation, influenced by air density ρ and dynamic viscosity μ as described by the equation:

$$Re = \frac{\rho(\Theta, p)VL}{\mu(\Theta)} \,, \tag{3.10}$$

where p represents the air pressure, V is the airspeed, and L denotes the characteristic length. Using Equation (3.10), the Reynolds number's temperature dependence was computed at different outside air pressures, leading to the results depicted in Figure 3.17. This Reynolds number variation was subsequently correlated with propeller performance based on insights from [28]. Wind tunnel tests, conducted on various APC propellers with varying Reynolds numbers, demonstrated the dependency of efficiency on non-dimensional propeller parameters, including Reynolds number.

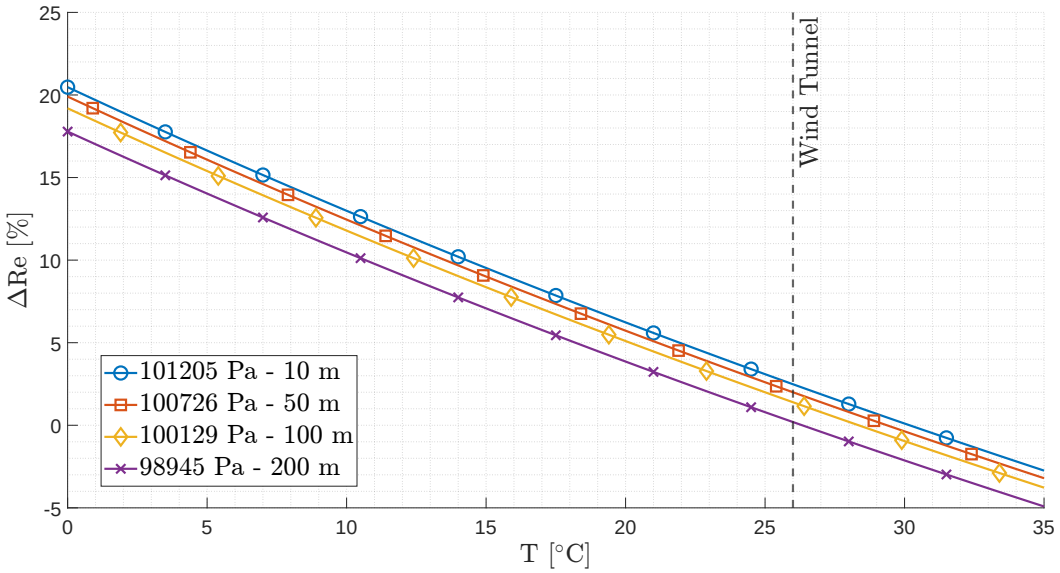

Figure 3.17: Percentage Reynolds number variation with temperature at different air pressures

Specifically, the trends illustrated in Figure 3.18 present the outcomes of tests conducted by [28] on an APC 18x12: assuming a worst-case scenario with a maximum airspeed of 22 m/s, a Reynolds number variation of approximately 100% (from 577,000 to 1,155,000) led to a 42% variation in thrust coefficient. Under similar conditions during cruise, the thrust coefficient increased by 17%.

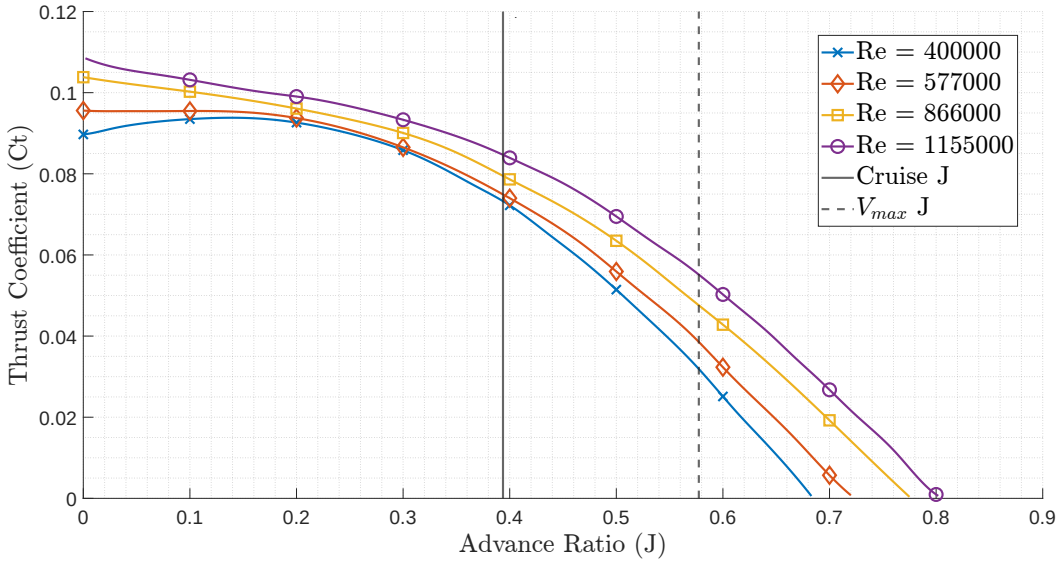

Figure 3.18: Thrust coefficient variation with propeller pitch at different Reynolds numbers

Referencing Figure 3.17, it is evident that the maximum anticipated Reynolds number variation due to temperature differences between the wind tunnel test chamber and the flight testing field is approximately 6%, resulting in a worst-case scenario thrust coefficient variation of less than 3%. This analysis concludes that the impact of temperature on Mach number and Reynolds number variation is minimal. Consequently, in the context of this research, temperature does not significantly affect thrust estimation.

Chapter 4

Multirotor flight testing

This chapter offers a comprehensive exploration of the multirotor performance of the VTOL. The first section explores the assessment of the PX4 Weathervane feature, providing insights into the system's capabilities in rejecting external disturbances. Moving forward, the analysis extends to the precision of the GPS module, disruptions in attitude states, and endurance during hover. The subsequent section explores the forward transition phase, dissecting the PX4 transition logic and detailing the flight testing procedures of this critical operational phase. Lastly, in the third section, the backtransition phase is examined in detail, covering the PX4 backtransition configuration and presenting the outcomes of dedicated flight testing efforts.

4.1 Outdoor multirotor

The multi-rotor (MR) phase of a VTOL drone flight is typically limited to short segments, predominantly during terminal phases, such as take-off and landing. However, specialized applications may demand operations in hover conditions or require precise MR maneuvering for positioning accuracy. Though brief when compared to fixed-wing flight, the MR phase is often the most power-intensive. This is due to the need for the generated thrust to sustain the entirety of the aircraft's weight, in contrast to the fixed-wing flight mode where aerodynamic lift counterbalances the weight, and propulsion is largely dedicated to forward movement. In the scope of this thesis, as already noted in Chapter 2 of [3], a major endurance-limiting factor is the voltage drop in the batteries. This is attributed to their internal resistance, since batteries are not ideal power sources, and to the high current drawn by the eight vertical motors during hovering or climbing. This limitation becomes particularly pronounced when vertical motors operate near their maximum capacity, a situation frequently encountered during yaw control maneuvers given the size and weight of the studied VTOL.
Yaw control in a standard quadcopter, whether configured in an "X" or "+" shape,

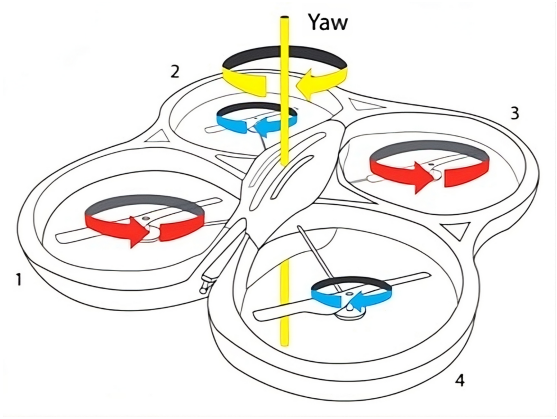

Figure 4.1: Simplified quadcopter CW yaw maneuver dynamic (source [9])

is tied to the balance of rotational speeds among its propellers. Typically, two propellers spin clockwise (CW) and the other two spin counterclockwise (CCW). This counter-rotation stabilizes the quadcopter by balancing out the total angular momentum and prevents it from spinning uncontrollably. For yaw control, the differential speeds of these propellers are modified. As depicted in Figure 4.1, by increasing the speed of the CCW propellers and simultaneously decreasing the speed of the CW propellers, the drone rotates in the CW direction, and vice versa. The principle remains the same for other multi-rotor configurations, in this case an octocopter, albeit with more propellers.

While the indoor environment of the Fly-ART facility ([29]) in the ASCL laboratory ([30]) permitted extensive MR flight testing, enabling the study of yaw control under the aircraft's self-induced turbulence, outdoor testing introduced a new variable: wind gusts. From the early stages of flight testing, these gusts posed significant challenges, particularly when motors reached saturation due to the controller's attempt to maintain a constant yaw angle, allowing little to no authority for control over other axes.

Figure 4.2 shows the yaw angle ψ in relation to the setpoint from the controller, along with the PWM of the vertical motors during an hover test performed in strong wind conditions. It can be observed that the setpoint is constant at a value of approximately 5 deg. Concurrently with the mismatches between actual and desired angle, four motors' speed increase drastically, or even reach saturation with a PWM value of 2014, and the other four slow down, or are turned off with an associated PWM value of 900. By closely analysing the two groups of motors, it became evident that the distinguishing factor between them was the motors' rotational direction, pinpointing the issue to the yaw control action. This undesirable and hazardous behaviour compromises flight safety. The aircraft becomes challenging to pilot, and the batteries experience excessive strain, as observed in Figure 4.3. The previously discussed voltage drop, which significantly diminishes the aircraft's endurance, is evident around the 5 seconds mark, coinciding with

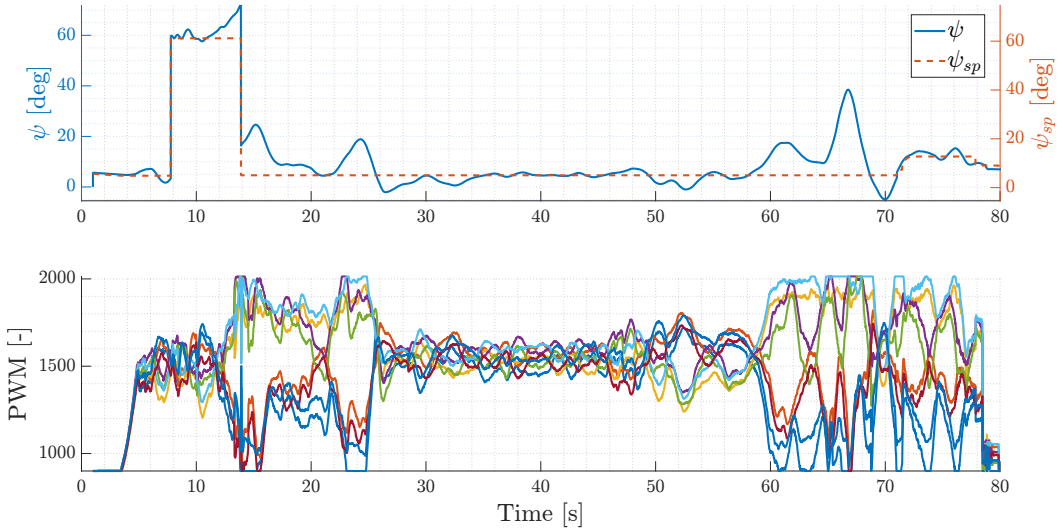

Figure 4.2: Vertical motors yaw angle against yaw setpoint (above) and PWM (below) during hovering without wind gust countermeasures

the vertical motors' PWM rise at take-off. Subsequently, the current drawn from the two batteries can be seen varying strongly during gusts, with peaks from lows of 30 A from a battery to highs of 120 A from the other. This test highlighted the necessity for a solution that allowed relaxation of the yaw control action, with consequent benefits to endurance, maneuverability and safety.

4.1.1 PX4: VTOL Weathervane feature

PX4's software offers a feature specifically designed for VTOL hybrid vehicles flying in multirotor mode: the VTOL Weathervane. Unlike pure multirotors, hybrid VTOLs possess large wings and control surfaces to facilitate fixed-wing flight. This extensive surface area is susceptible to wind forces, often resulting in undesired yaw moments. Such effects are especially pronounced in gusty conditions. In hovering flight conditions, the primary objective of the vehicle is to maintain its position. To achieve this while prevailing wind conditions, the drone has to counteract the disturbance of the wind. This counteraction is achieved by tilting the thrust vector in the direction of the relative wind, which can be visualized as the drone "leaning" against the wind. This tilt provides a visual cue, and by analyzing the orientation of the thrust vector, the drone's onboard systems can estimate the wind's direction.

PX4's weathervane feature offers a solution exploiting this behaviour. Instead of merely counteracting the wind's force, the weathervane controller actively works to orient the drone's nose into the estimated wind direction. This nose-forward orientation offers three primary benefits:

- aerodynamic efficiency: by pointing the aircraft's nose into the wind, the

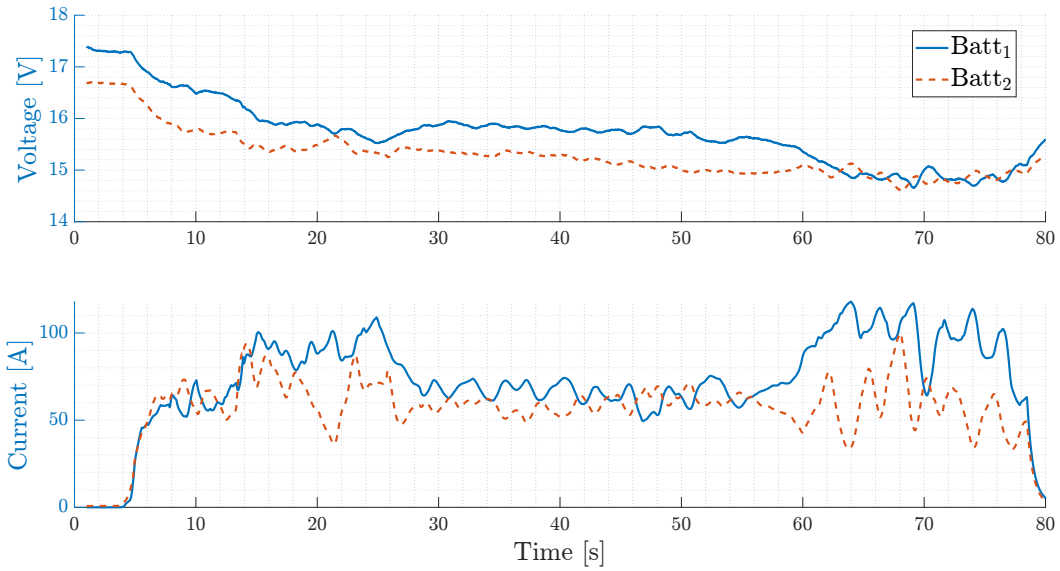

Figure 4.3: Batteries consumption during hover test in high wind conditions without gust countermeasure

hybrid VTOL can leverage its aerodynamic design to reduce drag, thereby improving energy efficiency and stability during hover;

- improved control: turning the aircraft's nose into the wind reduces the yaw moment induced by side winds. This proactive orientation means that the drone's control systems have to deal with fewer unexpected disturbances, ensuring smoother flight and better position hold;
- flight safety: orienting the nose into the wind minimizes the risk of side winds lifting a wing, which could potentially flip the vehicle, thereby enhancing the safety of the flight.

The weathervane feature on PX4 operates by constantly monitoring the drone's thrust vector orientation, and using sensors and onboard algorithms, the system estimates wind direction based on this tilt. Once the wind direction is estimated, the weathervane controller commands a yaw rate to turn the drone's nose into that direction. This dynamic adaptation ensures that the drone can maintain stable hover flight even in changing wind conditions. Three parameters are associated with the weathervane feature in the installed version of the PX4 firmware. These parameters are detailed in Table 4.1, which provides a brief explanation for each parameter as well as their set values for the test.

4.1.2 Weathervane testing and results

The weathervane feature underwent tests under conditions identical to those of the test depicted in Figures 4.2 and 4.3. Predictably, the aircraft's yaw setpoint

Parameters	Description	Value
WV_EN	Activation of the weathervane feature	Enabled (1)
WV_ROLL_MIN	Minimum roll angle at which the weathervane controller starts demanding a yaw rate	1.0 deg
WV_YRATE_MAX	Maximum yaw rate the weathervane controller can demand	90 deg/s

Table 4.1: Weathervane feature parameters in PX4 firmware v1.12

aligned exactly with the actual yaw angle, given that the desired orientation is dictated by the wind direction. The presence of gusts is evident from the continuous yaw angle fluctuations throughout the test, independent of pilot input. This yaw angle spans approximately from -25 to 35 deg, as visible from Figure 4.4. One of the direct benefits of this behaviour is visible in the same figure: the vertical motors' PWMs are considerably more consistent throughout the test, with infrequent short periods in which yawing control can be clearly distinguished, notably around 35 second. This enhancement improved the drone's stability and maneuverability, allowing the pilot to exploit the full potential of all eight motors during flight.

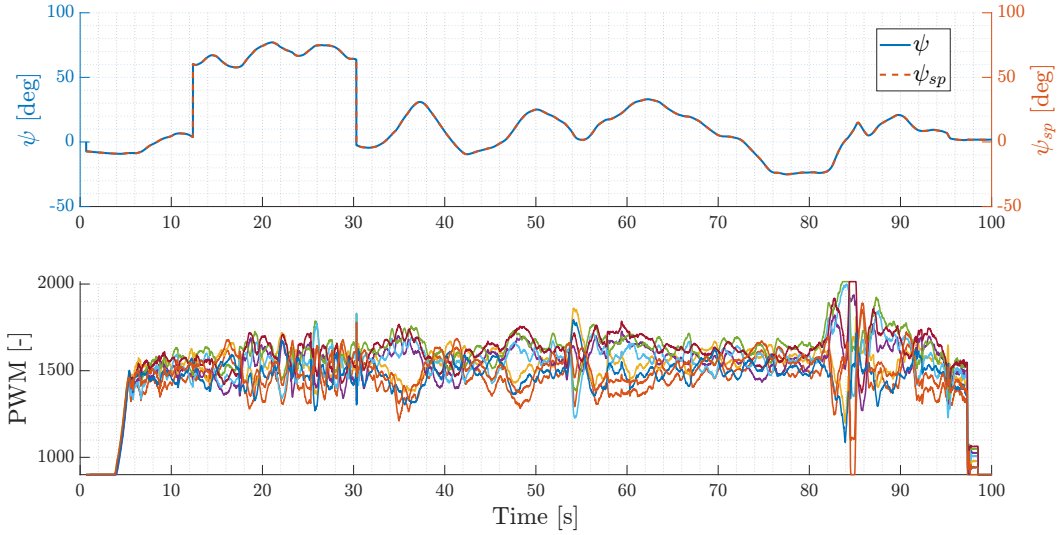

Figure 4.4: Weathervane enabled: yaw angle against yaw setpoint (above) and vertical motors' PWM (below) during hovering test

Battery consumption also experienced marked improvements, as illustrated in Figure 4.5: the average current drawn during gusts decreased from the range of 90 $\sim$ 100 A to 70 A. Only two slender peaks are noticeable at 100 A and 110 A, compared to the prior test where the battery current often exceeded 110 A, peaking at 117 A. This consistency and reduction in current consumption directly

impacts the voltage drop in the batteries, which in turn improves endurance.

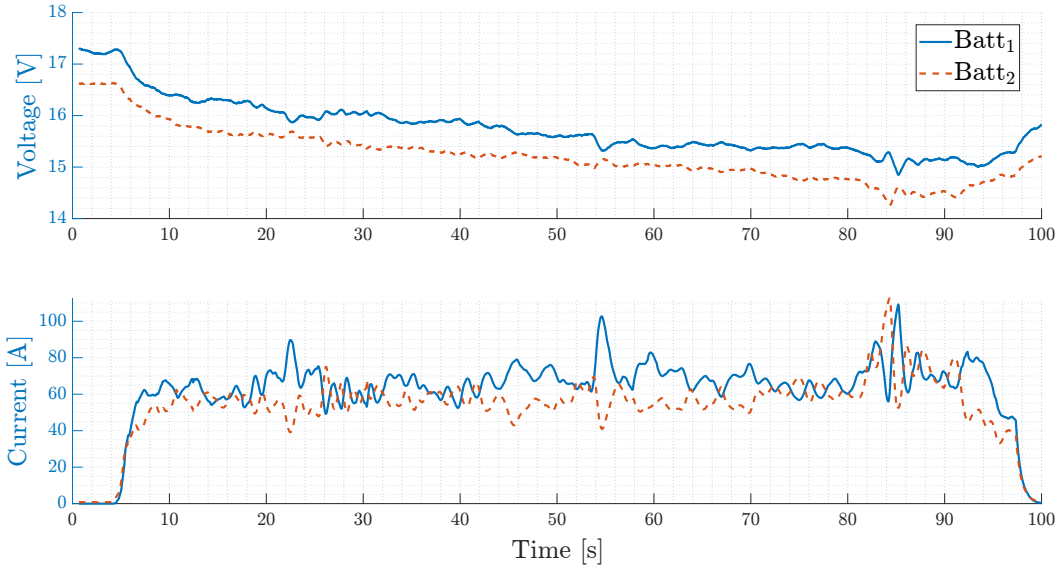

Figure 4.5: Weathervane enabled: battery consumption during hover test in high wind conditions

With this understanding, the profound implications of voltage drop from significant current drawn in the drone's multirotor mode become evident. Concurrently, the benefits the weathervane feature offers in windy scenarios to improve endurance are undeniable.

4.1.3 GPS module and positioning accuracy

In indoor test scenarios, the VTOL relied on a *Motion Capture system* (Mo-Cap) by OptiTrack [31] for precise position data. This system comprises 12 infrared-sensitive OptiTrack cameras, arranged to ensure multiple cameras capture the measurement object simultaneously. The aircraft is equipped with markers sensitive to infrared light, which, when interpreted by the Motive software platform [32], provide real-time estimates of the drone's attitude and position. However, when transitioning to outdoor testing, an alternative for the Mo-Cap system was mandatory. In this context, the VTOL's navigational requirements were addressed by its onboard M8N GPS module by Holybro [15]. This module, comprising a UBLOX M8N GPS unit, an IST8310 compass, and a safety switch for initial arming, was initially placed inside the fuselage, in front of the batteries, as illustrated in Figure 4.6a.
This shift in testing environment presented unexpected challenges. The batteries, which can draw in excess of 110 A each during certain mission phases, generate significant electromagnetic fields. This resulted in intense interference with the GPS compass' readings. The aircraft's trajectory during one of the tests is depicted

(a) Original GPS module positioning inside the fuselage (b) GPS module positioning on the right wing

Figure 4.6: Progression of the glass-fiber cladding process

in Figure 4.7. A massive drift with spiraling motion can be observed developing from the starting position until the pilot's manual intervention, highlighting the magnitude of the issue. Considering that the vehicle's local position is logged in a North-East-Down (NED) reference frame, it can be noted that the drift's area is approximately 3 m wide on the east-axis and 2.5 m on the north-axis.

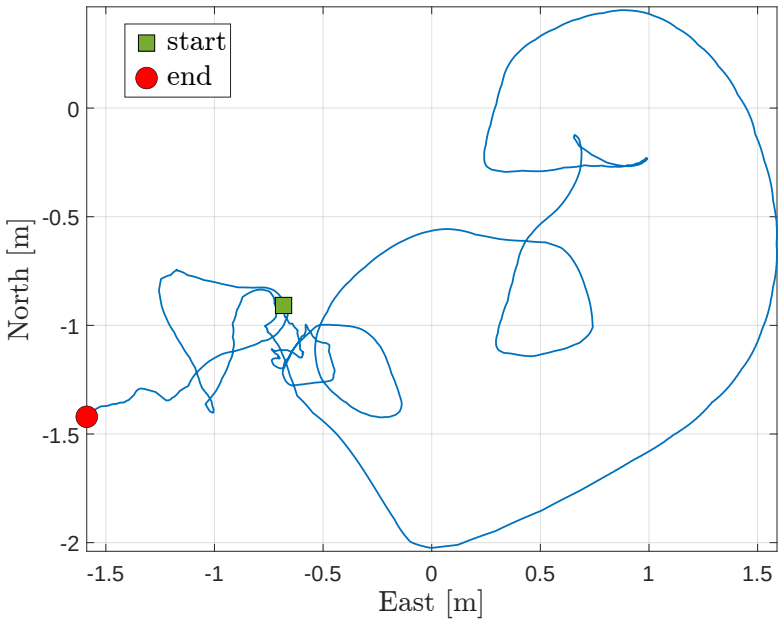

Figure 4.7: Trajectory during hover with GPS module inside fuselage

Given the unsustainable nature of this error, the GPS module's position was revised. It was relocated to the right wing, the farthest possible location from the power distribution cables, ensuring minimal interference. This new placement is

illustrated in Figure 4.6b, and will be taken into account in future design developments. Subsequent tests under this configuration brought encouraging results. The VTOL exhibited greatly improved position hold capability, with position drifts being contained within just 0.6 m range. This is a remarkable approximate 80% reduction when compared with previous tests. The improved trajectory, illustrated against the drift area from the earlier configuration (represented by the dash-dot line), can be viewed in Figure 4.8.

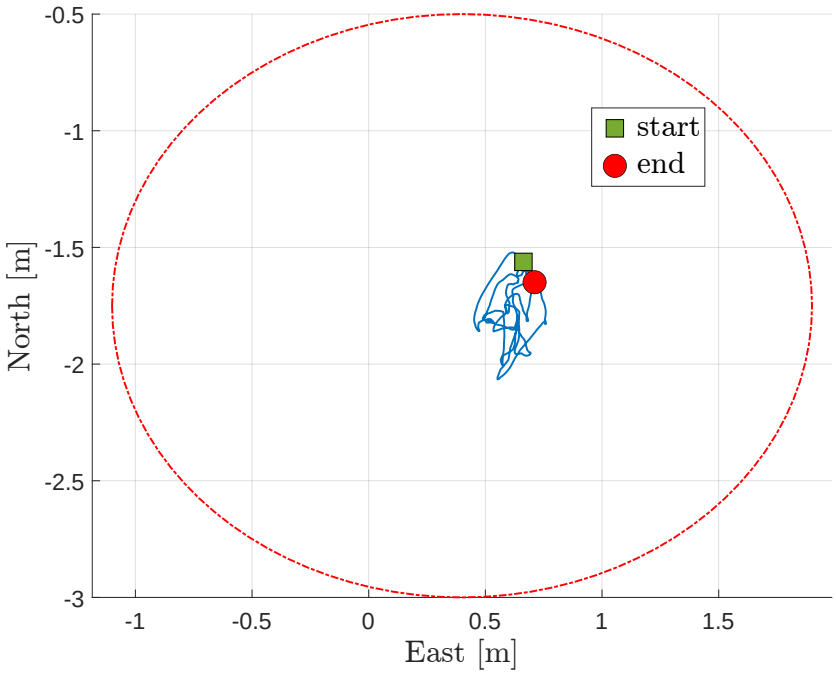

Figure 4.8: Trajectory during hover with GPS module on the right wing, red dash-dot curve represents position drift before the modification

In conclusion, the steps taken to mitigate the outdoor challenges and improve the VTOL's position hold capability have proven significantly effective. However, it is essential to acknowledge that further refinements remain recommended. Through fine-tuning of the onboard control systems parameters and sensor calibrations, it can be attempted to get closer to achieving an outdoor position holding accuracy that rivals the near-perfect results witnessed indoors using the Mo-Cap system.

4.1.4 Attitude states disruptions

During the flight testing campaign, an anomalous behavior was consistently observed in the aircraft's attitude. This issue, predominantly emerging at the beginning of each mission, manifested itself as abrupt spikes in the drone's attitude readings. Despite the extensive investigations, the precise cause has not been

pinpointed. The anomaly's characteristic behaviour can be observed in the upper part of Figures 4.2 and 4.4. In both figures, a distinctive pattern emerges shortly after take-off, typically between the 5 and 15-second mark. Here, the yaw angle setpoint and the actual yaw angle estimate experience a sudden jump, approximating a 60 deg shift. This change is not persistent though; the readings revert to their original values within a span that can range from a few seconds to almost half a minute. Though the data suggests a yaw rotation, actual visual observations of the aircraft during these episodes reveal no change in its orientation. Instead, the anomaly seems to manifest more noticeably in the drone's pitch and roll behaviour. This is illustrated in Figure 4.9, which showcases data from another test, emphasizing the regularity of this unexplained dynamic. Concurrent with the reversion of the yaw angle to its original value, the aircraft's roll angle ϕ undergoes a swift, approximately 15 deg adjustment in just a second, before stabilizing. Similarly, the pitch angle θ also spikes by about 10 deg.

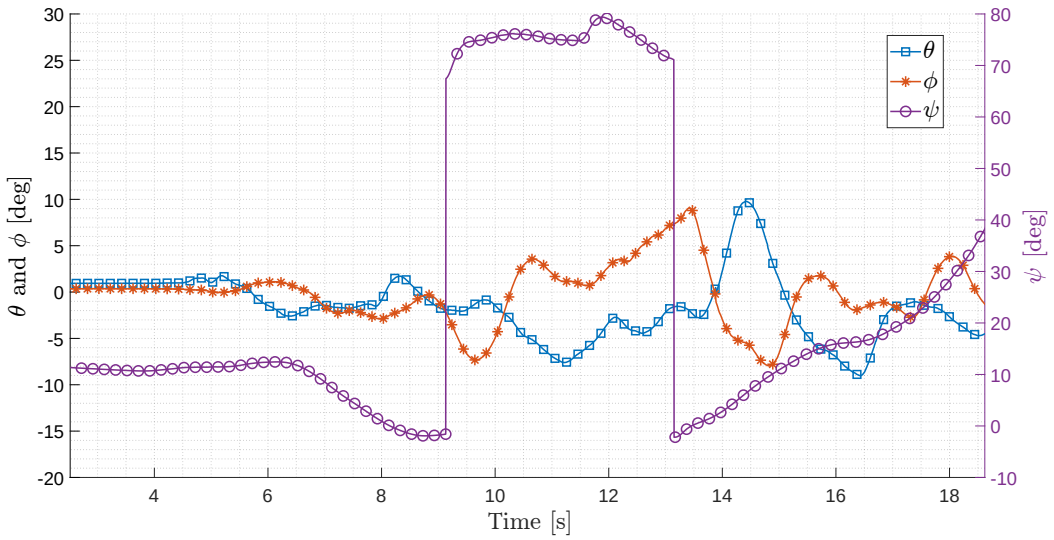

Figure 4.9: Correspondence of attitude spikes with the step variations of the yaw angle

Given the lack of actual yaw rotation and the pronounced alterations in roll and pitch, the preliminary hypothesis leaned towards potential issues in the attitude estimation process. It is plausible that interruptions or switches between different sensor data streams, or perhaps between different Extended Kalman Filter (EKF) instances, could be the underlying cause. Such switches might be initiated as the system's response to perceived data anomalies or discrepancies between sensors or EKF instances.

4.1.5 Multirotor hover endurance

The evaluation of the aircraft's hovering endurance is crucial, considering it represents one of the most energy-intensive mission profiles, excluding factors such as strong winds and maneuvering.

Test objective and execution

The primary objective of this test is to determine the endurance of the drone in a hovering condition, maintaining a constant attitude, altitude, and in-plane position. Additionally, the test aims to determine also the hovering throttle setting, a critical parameter for the multirotor controller. The test procedure is outlined as follows:

1. arm the drone and set the control mode to position;
2. take-off and climb to the predetermined test altitude, preferably at low altitude to save battery power for the hovering phase;
3. release the control sticks and allow the drone to hover until the batteries reach a predefined low voltage;
4. descend, land and disarm.

Results

Due to the test's simplicity, data processing is minimal, and the results can be directly extracted from the logs. Excluding the climb and descent phases, the strictly hovering endurance was 2 minutes and 40 seconds. The batteries' parameters during the test are visually represented in Figure 4.10, and the results are summarized in Table 4.2.
Both batteries exhibited similar behaviour during the test, with the first one concluding with a slightly lower voltage value. This discrepancy arises from one of the batteries supplying power also to the electronic components of the aircraft and drawing a higher current. Specifically, during this test, the first battery drew approximately 60 to 70 A, while the second one drew around 50 A.

Parameter	Initial value	Final value
V_{batt_1}	15.74 V	14.16 V
V_{batt_2}	15.72 V	14.32 V
THR_{hover}	52%	59%

Table 4.2: Results of the hover endurance test

Finally, the hovering throttle increased from 52% to 59% during the test duration. This adjustment is attributed to the control system's need to incrementally

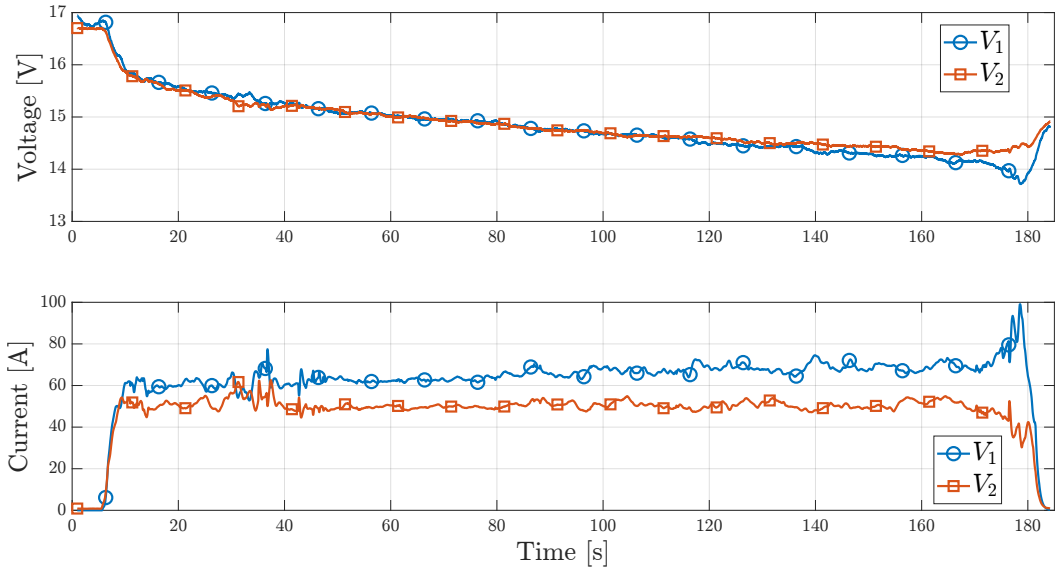

Figure 4.10: Battery states during the hover endurance test

boost throttle over time, compensating for the diminishing power as the battery discharges and ensuring a constant altitude. Factors such as battery efficiency, capacity, and response to power demands contribute to the varying throttle requirements during flights.

4.2 Forward transition phase

At the heart of a VTOL's unique capability is the ability to perform a transition between multirotor and fixed-wing flight and vice versa. This maneuver presents several complexities, demanding precision in control, stability, and efficiency. A VTOL's transition from hover to forward flight is especially critical because it comprehends the complex interaction between aerodynamic forces, control logic, and propulsion dynamics. Ensuring a smooth transition is paramount, as any instability or inefficiency during this phase can compromise the aircraft's performance or even its structural integrity.

The PX4 autopilot system, renowned for its robustness and versatility, handles this transition phase with a layered approach. At a high level, PX4's logic primarily revolves around gradually changing the control from the vertical rotors to the main wing in a fixed-wing configuration. This process is not a simple on-off switch; rather, it involves intricate algorithms that consider various factors such as the aircraft's current speed, altitude, attitude, and the desired trajectory. The PX4 system typically divides the transition into sub-phases, with each sub-phase having its set of control objectives and safety checks. This ensures that the aircraft remains stable and follows the desired flight path throughout the transition.

Furthermore, the transition logic in PX4 also incorporates fail-safes and redundancy. In the event of an anomaly, such as a motor failure or a sensor reading discrepancy, the system can abort the transition and revert to a safe mode, ensuring the aircraft's safety. In the upcoming section, the data analysis of the VTOL's transition phase tests will be examined to better understand its behaviour and bring improvements to the reliability and efficiency of the maneuver.

4.2.1 PX4 transition logic

VTOL vehicles uniquely combine the hovering capability of multicopters with the range and efficiency of fixed-wing aircraft. This comes at the cost of added complexity in control, especially during the transition phase between multicopter and fixed-wing modes. PX4 provides advanced logic to manage these transitions.

VTOL flight control structure

The PX4 VTOL flight controller integrates both multicopter and fixed-wing controllers. Depending on the operational mode, they can either run separately or concurrently, for instance during transitions. Considering Figure 4.11, the central block to observe is the VTOL attitude controller, which manages the switching and blending logic for VTOL modes and handles specific control actions during transitions, like the ramp-up of the forward flight motors in standard VTOLs. For standard and tilt-rotor VTOLs, the fixed-wing attitude controller produces rate setpoints during transition. These are channeled to separate rate controllers, which generate torque commands for both the multicopter and fixed-wing actuators and send them to the VTOL attitude block. Outputs from the VTOL attitude block are distinct torque and force commands for both multicopter and fixed-wing actuators. These outputs are managed by an airframe-specific control allocation class, *i.e.,* the mixer matrix. A mixer, in the context of VTOLs and multirotor aircraft, is a software component that determines how control commands are allocated among multiple actuators. It translates desired flight commands (like roll, pitch, yaw, and throttle) into specific actuator outputs, such as motor speeds or servomotors positions.

Airspeed scaling and controllers blending

One critical aspect of PX4's VTOL transition logic is the airspeed scaling, ensuring the vehicle's stable control across a range of airspeeds. The rate controllers in PX4 produce angular acceleration setpoints for the mixer. These setpoints are essential for the mixer to generate the required torques using the aerodynamic control surfaces. The torques produced are directly influenced by relative airspeed and air density. For example, the roll moment generated by the ailerons can be expressed as

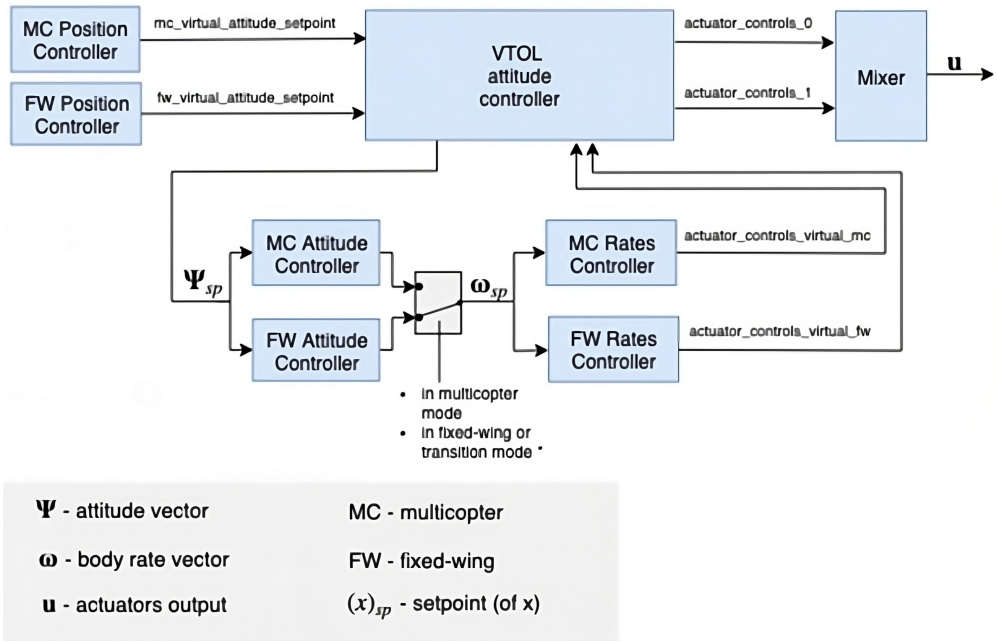

Figure 4.11: PX4: diagram of a VTOL aircraft control structure (source [10])

$$M_{roll} = \frac{1}{2}\rho V^2 S b C_m \,,$$

where S is the reference surface, b is the wing span, C_m is the nondimensional roll moment derivative coefficient, and V is the true airspeed (TAS). This equation demonstrates the importance of airspeed in torque generation: a controller that is finely tuned for a specific cruise airspeed might cause oscillations at higher airspeed or bad tracking performance at lower airspeed. Therefore, PX4 incorporates airspeed scaling. Beyond airspeed scaling, PX4 uses a blending algorithm that gradually shifts the weighting between the multicopter and fixed-wing controllers based on certain criteria, like the current airspeed. For instance, during a transition to forward flight, as the aircraft gains airspeed and gets closer to being able to sustain fixed-wing flight, the influence of the multirotor controller diminishes while the weighting of the fixed-wing controller increases. This progressive blending ensures that at any point during the transition, the control inputs are a composite of both controllers, suited to the aircraft's immediate flight conditions. This blending logic, when coupled with airspeed scaling, ensures that the aircraft's response remains linear and predictable, regardless of the phase of flight or conditions.

Transition controller tuning in PX4

Transitioning between multicopter and fixed-wing modes is a delicate process, requiring precise tuning to ensure a safe entry into fixed-wing mode and prevent scenarios such as stalling due to insufficient airspeed. This section explores various PX4 parameters crucial for fine-tuning this transition maneuver:

- VT_ARSP_TRANS: sets the airspeed at which the transition from multirotor to fixed-wing mode is completed;
- VT_ARSP_BLEND: sets the airspeed at witch the blending of multirotor and fixed-wing control is enabled as the transition airspeed approaches;
- VT_TRANS_TIMEOUT: sets the time, in seconds, after which the transition will be stopped if not completed;
- VT_F_TRANS_THR: defines the target throttle for the FF motors during forward transition;
- VT_PSHER_RMP_DT: defines the time window during which FF motors' throttle ramps up linearly to VT_F_TRANS_THR during the transition.

4.2.2 Transition phase flight testing

Following the understanding of the complexities and configurations of VTOL transitions, the next phase involved real-world flight testing aimed at validating theoretical and simulation predictions.

Test objectives and execution

Given the experimental nature of the drone, initial transition test goals focused on gradually exploring the aircraft's ability to perform the maneuver and assessing its behavior during acceleration. As confidence in the tests grew, additional objectives were incorporated, including evaluating the distance and time required to complete the transition phase, observing altitude variations, and gaining an in-depth understanding of the controller's dynamics during the blending phase. The general execution of a transition test followed these steps:

1. upon reaching the test altitude, select the predefined control mode;
2. operate the transition switch to begin the acceleration;
3. center the control sticks and maneuver only if strictly necessary;
4. operate the switch again to activate the backtransition maneuver based on criteria such as reaching predefined airspeed, transition timeout, or critical battery levels;

5. in case of completion of the transition phase, proceed with fixed-wing flight, maneuvering until properly aligned with the field for backtransition and landing.

Furthermore, all transitions conducted during flights dedicated to other tests have been analyzed and considered for upgrades and parameter modifications. This comprehensive approach ensures that insights gained from various test scenarios contribute to the refinement of the transition controller and overall system performance.

Performance results

Upon the conclusion of the flight test campaign, a total of 31 transitions were analyzed, each involving distinct combinations of propellers, transition parameters, and test objectives aimed at refining the maneuver. Table 4.3 summarizes some of the most representative tests. As a preliminary outcome, reducing the parameter VT_PSHER_RMP_DT from 3 seconds to 1 second immediately enhanced the transition by eliminating initial in-plane position drift and reducing accelerations times. This initial drift has been encountered also in Simulink simulations with the custom controller from the previous thesis [3], and is due to the fact that during transition there is no position control active, leaving the aircraft susceptible to wind and gusts. A significant improvement ensued with the substitution of the GF 6x4.5 propellers with the GF 9x4.3. This change resulted in a notable reduction of the distance required to reach an airspeed of approximately 9 m/s from 69 m to 23 m, accompanied by a halving of the required time.

Test number	Propeller	Test goal	Distance [m]	Duration [s]
003	GF 6x4.5	V = 9 m/s	69	13.6
006	GF 9x4.3	V = 9 m/s	23	6.9
008	GF 9x4.3	V = 14 m/s	119	15
015	GF 9x4.3	completion	114	12.4
025	APC 10x55MR	completion	34	6.9
026	APC 10x55MR	completion	82	9.4

Table 4.3: Progression of transition test results over time

However, further testing revealed that this high acceleration was limited to lower airspeeds and rapidly decreased above 10 m/s. Test number 008 is an example of this, with a maximum achieved airspeed of 14 m/s after traveling approximately 120 m, reaching the set timeout limit of 15 seconds and reverting to multirotor mode.
It is crucial to note that wind conditions significantly influenced test outcomes, especially with less thrusting propellers. Careful pre-flight planning for aircraft placement and orientation aimed to maximize available space, more importantly,

align with the headwind. Despite these efforts, variable and unpredictable wind conditions during setup, take-off, and climb phases contributed to different outcomes even with identical configurations.
To address the limitations of the GF 9x4.3 at higher airspeeds, the APC 10x55MR propellers were mounted and tested. This substitution resulted in a remarkable improvement, with all transitions completed within a distance of 85 m from the starting point. Notably, the duration of the maneuver was substantially reduced, completing the transition phase within a 6.5 to 9 seconds time-window, compared to cases where the 15-second timeout limit was reached.

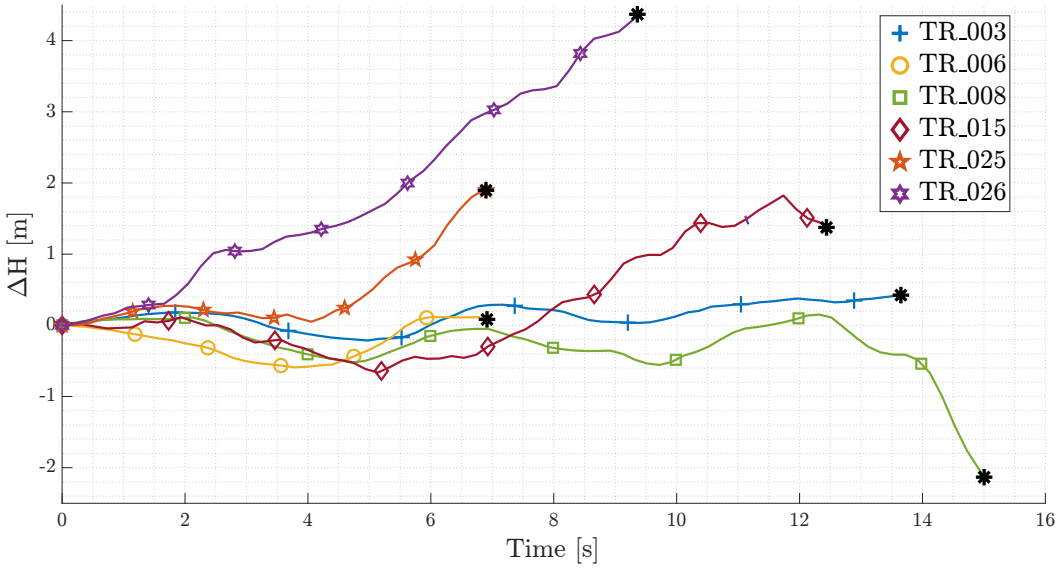

Figure 4.12: Comparison of the altitude trends during the transition tests outlined in Table4.3

The investigation into the performance of the transition phase included an analysis of altitude loss, with particular attention to the differences observed before the glass-fiber cladding upgrade to the wings, proving to be a decisive factor.
Figure 4.12 presents a comparison of the altitude variations during the transition tests outlined in Table 4.3. The black asterisk (*) symbol marks the conclusion of each transition, either by completion or manual interruption. Most transitions exhibit an altitude loss limited to less than 1 m before completing the maneuver, as depicted in the figure. The only exception is test number 008, which failed to complete the transition and reached the time-out limit with an altitude loss of 2.1 m.
The maximum recorded altitude loss across the entire test database is 3.2 m, reducing to 1.1 m when considering only tests performed with the aircraft in its final configuration, equipped with APC 10x55MR propellers and cladded wings. This result confirms the maneuver's good reliability, highlighting the possibility of executing it at relatively low altitudes to save battery charge during the multirotor

climb. However, it is advised to perform it with a considerable safety altitude margin to allow recoveries in case of unexpected behaviour.

Aircraft's behaviour observations

The behavior of the aircraft was closely observed during the tests, considering changes in both parameters and hardware configurations. One notable dynamic observed was a pitch-up attitude at the beginning of the transition phase. While this did not immediately impact altitude or disrupt the maneuver, it drew attention to another aspect related to the controller: the buildup of elevator deflection. An example test illustrates in Figure 4.13 that the aircraft exhibits a pitch-up attitude at the onset of the transition phase. The elevator starts deflecting downwards (positive deflection) as the aircraft pitches up, reaching approximately $\delta_e = 30$ deg. As the aircraft gains speed and returns the nose to a zero pitch attitude, the elevator's deflection decreases slowly, leaving a residual 15 to 20 deg deflection, hardly going to negative values even when the pitch angle reaches nearly -10 deg.

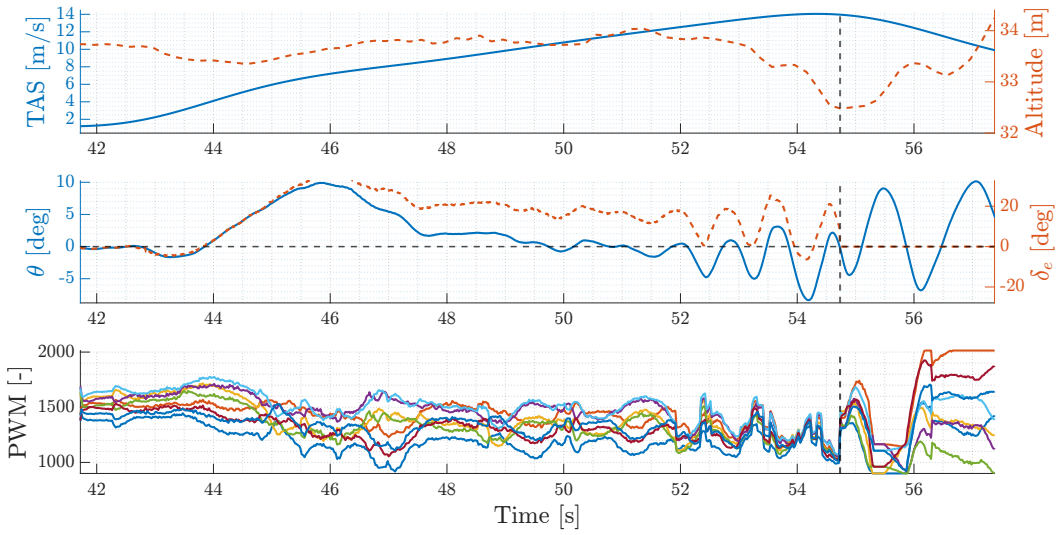

Figure 4.13: Elevator's deflection buildup and pitch-up attitude during test number 013; vertical dashed line represents transition end

To further investigate this issue, ground tests were conducted by manually tilting the aircraft with shutdown motors. Upon realignment to the horizontal plane, the elevator did not revert to a neutral position but maintained some degrees of deflection confirming assumptions. The parameter associated with the integral gain of the pitch rate, with a default value of 0.1, has then been lowered. This modification proved effective in resolving the issue, making the elevator more responsive to the pitching behaviour of the aircraft.
This behavior prompted an investigation into the VT_ARSP_BLEND parameter's functionality. According to the PX4 User Guide, this parameter defines the air-

speed at which the blending of FW and MR controls begins [10]. However, in practice, as seen in Figure 4.13 and consistent across all tests, the elevator starts deflecting before reaching the specified blending airspeed of 12 m/s, indicating a deviation from the expected controller behavior.
Furthermore, the PWM values of the vertical motors in Figure 4.13 demonstrate that their throttle did not decrease significantly as airspeed increased. This observation underscores the inadequacy of the wing's manufacturing technique prior to its glass-fiber cladding.

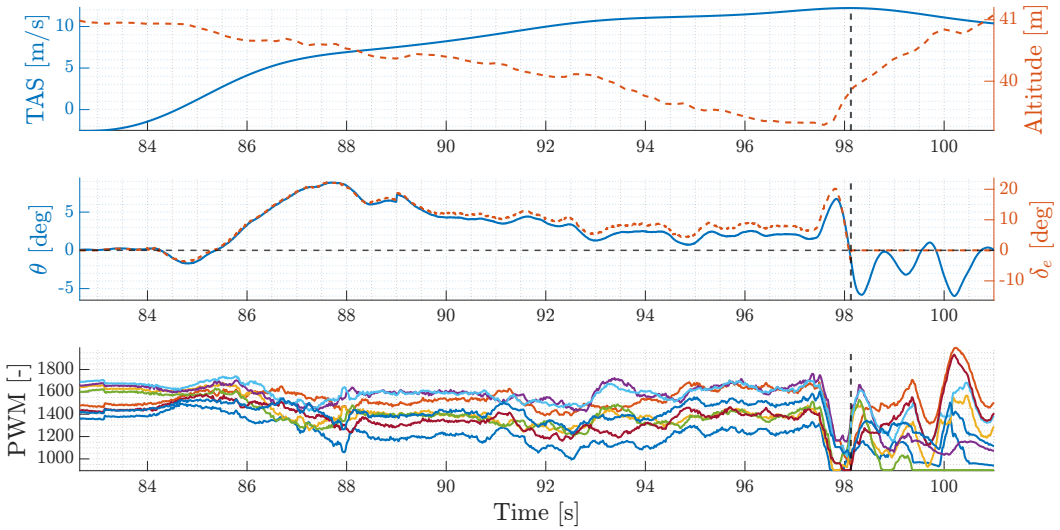

Figure 4.14: Transition phase with improved pitch rate proportional and integral gains

After addressing the elevator's deflection buildup, attention turned to divergent pitch oscillations oscillations (an example in Figure 4.13, around 52 seconds). These oscillations, initiated at the blending airspeed, involved both aircraft pitch and elevator deflection, as well as the PWM of the vertical motors. Considering the timing and the involvement of both MR and FW control action, the interaction between the aggressive FW controller and the MR controller during their blending phase was identified as the cause.
Being the MR controller's gains already tuned and validated, modifications were made to the FW pitch rate gains, specifically lowering the default value of the proportional gain from 0.08 to 0.05.
The impact of these adjustments is evident in Figure 4.14: the elevator's deflection now more promptly follows the aircraft's pitching behavior, and oscillations are notably reduced. It is important to note that, despite the improvements in pitch control, the PWM of the vertical motors did not decrease, as there were no hardware changes between the tests shown in Figures 4.13 and 4.14.
After further testing, hardware modifications, and increased confidence with the system, the final result is depicted in Figure 4.15, showcasing a test executed with

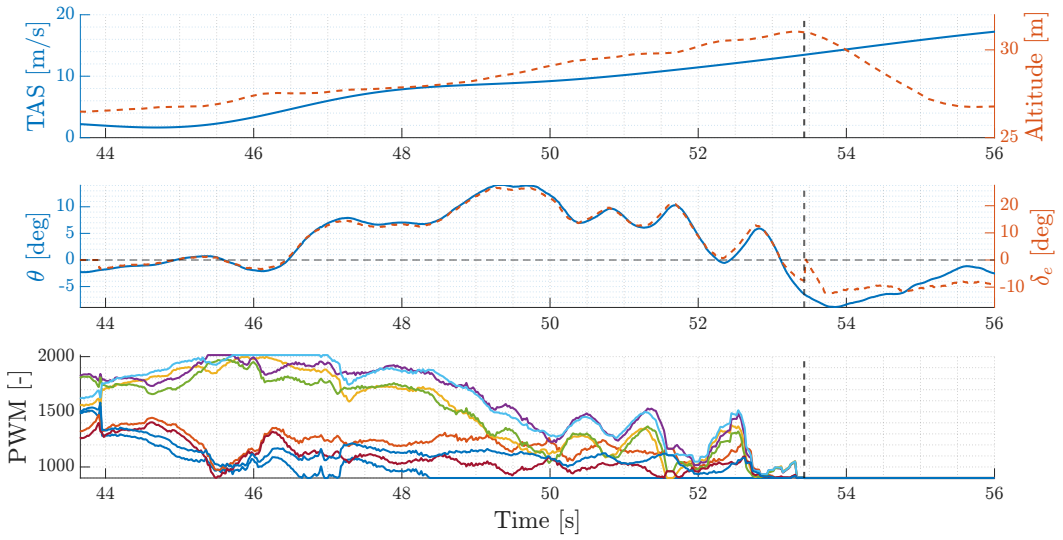

Figure 4.15: Properly executed transition example

the latest configuration. Several key improvements have been achieved, rendering the maneuver highly efficient and reliable:

- the elevator's deflection now aligns more consistently with the aircraft's behavior, working properly in both up and down directions without visible asymmetries;
- the blending phase has been smoothed, and although small oscillations persist, they do not significantly impact the maneuver, avoiding altitude loss or breaks in acceleration;
- the PWM of the vertical motors gradually decreases to 900, indicating the motors' stopping, as the aircraft completes the transition phase, confirming the wing's effective production of lift.

Furthermore, comparison with simulation results from the previous thesis [3] revealed notable similarities. The prediction was that the aircraft would require 15 seconds to reach a cruise speed of 15 m/s from a hovering condition, a performance goal that has been largely achieved, thanks in part to the improved propellers. Interestingly, a common aspect observed between simulation and flight testing is the gained altitude during the transition phase, followed by a descent to return to the initial altitude. This behavior can be seen in Figure 4.15, highlighting consistency between simulated predictions and actual flight testing results, and enhancing the credibility of both the developed simulation model and the implement flight control strategies. Table 4.4 provides a comparison between the initial and final configurations. Note that the dimensions of the wing and elevator also changed, as detailed in Chapter 2.

	Initial state	Final state
VT_PSHER_RMP_DT	3 s	1 s
VT_ARSP_BLEND	8	11
VT_TRANS_TIMEOUT	15	16
FW_PR_P	0.08	0.04
FW_PR_I	0.1	0.01
Propellers	GF 6x4.3	APC 10x55MR
Elevator	balsa wood	foam with carbon-fiber plate
Wing	3D printed ribs and Mylar coating	glass-fiber cladded foam

Table 4.4: Transition parameters and components evolution throughout the flight test campaign

Future developments

In conclusion, while significant improvements have been made to the transition phase, resulting in a reliable and safe execution, further investigation into the blending phase and its associated parameter VT_ARSP_BLEND is recommended. A deeper understanding of its logic will help address the question regarding the elevator's operation before reaching the set speed. Moreover, the current study relies on the conversion of PWM signals sent to each actuator, lacking direct measurements of control surface deflection. To enhance the precision of future studies, a suggested implementation involves the use of a small camera for better inspection of the moving parts of the aircraft during testing. Lastly, implementing the custom controller developed in the previous thesis ([3]) on the aircraft would offer comprehensive control over the intricacies of the transition logic. This would enable the exploration of different strategies proposed in the previous work, potentially providing additional insights and improvements to further enhance the performance and reliability of the transition phase.

4.3 Backtransition phase

The versatility of VTOL aircraft is represented not only by their ability to transition into forward flight but also in their capability to revert from fixed-wing mode back to multirotor, known as the backtransition. This stage is as complex as the forward transition, especially since it occurs during the landing phase, so near the ground. This maneuver represents the conversion of the aircraft's high-speed momentum from its fixed-wing state into a stable hover as a multirotor and it involves different aspects:

- aerodynamics: the wings that provide lift during forward flight now contribute to drag during the backtransition, with the vertical motors resuming

responsibility to sustain the aircraft's full weight.

- Control systems: stability during backtransition is imperative. The system must transition control seamlessly from the wings to the rotors, ensuring no destabilizing influences.
- Operational context: unlike the forward transition that can commence at various altitudes, backtransitions are typically closer to landing zones, requiring additional safety considerations due to potential obstacles and terrain.

4.3.1 PX4 backtransition logic

Similar to the transition phase, the backtransition comprises three main segments. The first is the initiation of the maneuver, which usually occurs in a straight-level flight condition with reduced airspeed. The aircraft then enters the deceleration phase, where, in the simplest scenario, the front propellers shut down, and aerodynamic drag is exploited for deceleration. As the aircraft slows down, control authority gradually shifts from being completely allocated to the FW controller to being entirely allocated to the MR controller. Ultimately, PX4 considers the maneuver completed either when the horizontal speed has reached the multirotor cruise speed, or when the backtransition duration set by the user has passed.

PX4 also offers the option to engage air brakes and set their deflection to a predetermined value to facilitate the deceleration phase and reduce the required space and time. Moreover, for aircraft equipped with ESCs capable of reverting motors' rotation, PX4 also supports active breaking through FW motors thrust reversal, expected to provide the shortest possible backtransition [10].

Backtransition controller tuning in PX4

Considering the early stage of the flight test campaign and the absence of air brakes on the aircraft, the backtransition phase has been mainly tunes through two parameters:

- VT_B_TRANS_DUR: it sets the duration of the backtransition maneuver, from operation of the switch to complete stopping of the aircraft;
- VT_B_TRANS_RAMP: it sets the duration during which the MR motors ramp up to the commanded thrust during the backtransition stage.

Setting a proper combination of these two parameters is of paramount importance to the successful and flawless execution of the test. Setting a longer duration allows the vehicle more time to aerodynamically slow down and subsequently gradually ramp up the MR motors allowing a smoother maneuver compared to a shorter duration. The longer the duration, the more extended the distance covered while

gliding, with the risk of drift, given that the controller will have only altitude control active during the backtransition phase. The transition duration has to be set longer than the motors' ramp-up; the default values are set to 4 and 2 seconds, respectively. The maneuver works as follows:

1. activation of the backtransition switch with consequent shutdown of the FF motors;
2. constant altitude glide for 2 seconds while aerodynamic drag slows the aircraft down;
3. ramp-up of the MR motors for 2 seconds;
4. completion of the maneuver with the goal of achieving an immediate hover condition at the 4-second mark.

The critical nature of backtransition flight testing becomes evident when considering the potential consequences of shorter duration and ramp-up times. These factors can lead to a maneuver completion attempt with higher residual airspeed and a more aggressive vertical motors activation. In contrast, the ideal scenario envisions a precise, short and controlled stoppage of the aircraft at a low altitude, allowing a descent with minimal battery usage, maximizing the FW portion of the mission. Efficient execution of the backtransition is not only a matter of optimizing performance but is crucial for safety reasons. As discussed in Section 4.1, the voltage drop during multirotor operations poses challenges. A scenario with a low battery level, high airspeed, and excessive vertical motors throttle represents a potential worst-case situation and could lead to in-flight power cut-off, with severe consequences.

4.3.2 Backtransition flight testing

As soon as the transition phase flight testing began, the focus has been shared with the backtransition phase. Testing this phase implies exploring its dynamics and deepening the understanding of the controller's logic. Lastly, performance such as required distance, altitude variations and assumed attitude has been assessed.

Test execution

The common procedure of execution of a backtransition follows these steps:

1. reduce throttle and properly align the aircraft with the field;
2. achieve level flight at a sufficiently low airspeed;
3. operate the backtransition switch and center the sticks;

4. once the backtransition is complete, regain control of the aircraft, descend, and land in multirotor mode.

Despite the seemingly straightforward procedure, regaining control after the maneuver presented hidden challenges, as discussed in the following section. Two factors contribute to complicating matters:

- the backtransition serves also as an emergency maneuver to recover MR flight in critical scenarios during FW flight, *e.g.,* significant altitude loss in transition phase or during forward flight. The quick shift from flying as fixed-wing to flying as multirotor places significant load on the pilot.
- The controller's actions may lead to saturation of the vertical motors, particularly in altitude and position control modes, when countering external disturbances. This saturation results in the aircraft's inability to generate the necessary control moments for maneuvering. Conversely, manual control mode allows full control of the motors' throttle but significantly increases the pilot workload.

Test results

The analysis of backtransitions, whether initiated to conclude a mission or as emergency maneuvers, has been comprehensive. However, it is essential to note that backtransitions resulting from an aborted transition phase are not recognized by the controller, and the associated flag in the logged data is not triggered.
In the initial stages of the flight testing campaign, the emphasis was on quickly recovering MR flight in response to unexpected aircraft behavior, prioritizing recovery speed over smoothness. This approach was reflected in the parameter values, set to VT_B_TRANS_DUR = 2 and VT_B_TRANS_RAMP = 1. In practical terms, upon activation of the backtransition switch, the controller rapidly shut down the front motors and, after one second, started ramping up the vertical motors. Within one more second, the maneuver would be completed, attempting to bring the aircraft to a complete stop. As anticipated, this brief duration minimized the distance required for vertical motor activation, especially the vertical distance, crucial during emergency situations. However, the trade-off involved assuming steeper attitudes and placing heavier loads on the structure, conditions temporarily accepted to prevent potential crashes.
Figure 4.16 illustrates an emergency recovery performed with the aforementioned parameters' setting. The dashed vertical lines indicate the beginning and ending of the backtransition phase. In the depicted scenario, after an altitude loss of approximately 6 m during a transition test, the backtransition was activated. The vertical motors' PWM immediately ramped up to saturation while pitch angle increased from -32 to 29 deg, resulting in an intense deceleration and a visible flexion of the large wing, indicating excessive structural load. From the

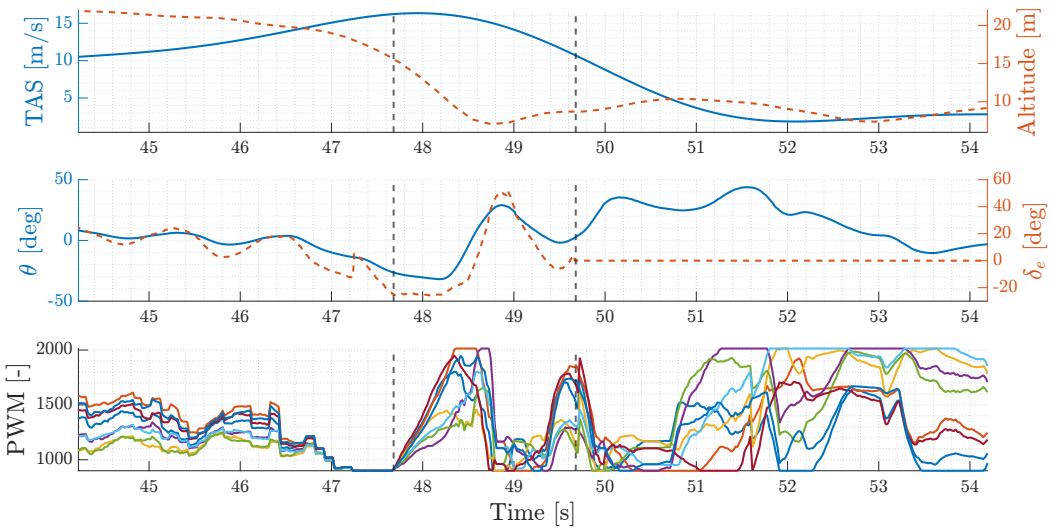

Figure 4.16: Emergency backtransition executed with 2 seconds duration and 1 second ramp-up

instant of activation, an additional 9 m of altitude has been lost before recovery, with the elevator reaching a deflection of 50 deg and a maximum pitch angle before complete stop of 43.8 deg.

To address the structural load concerns and improve overall maneuver performance, the motors' ramp-up was extended to 2 seconds, while keeping the duration the same. The results of implementing these changes are illustrated in Figure 4.17.

In this updated configuration, the pitch behaviour significantly improved, reaching a maximum of 16 deg; the altitude exhibited a slight increase during deceleration. With both parameters set to 2 seconds, the vertical motors' PWM started increasing immediately upon activation of the phase. This, combined with the pitch-up attitude, effectively slowed the aircraft from 14.6 m/s to 10 m/s. The complete stop was achieved in approximately 50 m over a time period of 4 seconds. This performance was deemed satisfactory and notably reduced structural loads.

In the later stages of the flight test campaign, the parameters were reverted to their default values of 4 seconds duration and 3 seconds ramp-up, and additional tests were conducted. The objective was to assess the improvement margin concerning altitude variation and pitch angle. The results of this combination of parameters, consistent across tests, are shown in Figure 4.18. Surprisingly, this setting did not yield significant differences from the previous combination: the more progressive vertical motors' ramp-up allowed a better deceleration phase, slowing the aircraft from 15.4 m/s to less than 5 m/s in the 4 seconds duration, achieving a full stop in approximately the same distance. However, the pitch angle reached 21 deg during deceleration and 29.8 deg at stoppage, higher values than those obtained with the shorter duration and ramp-up. Even though the longer times allowed a

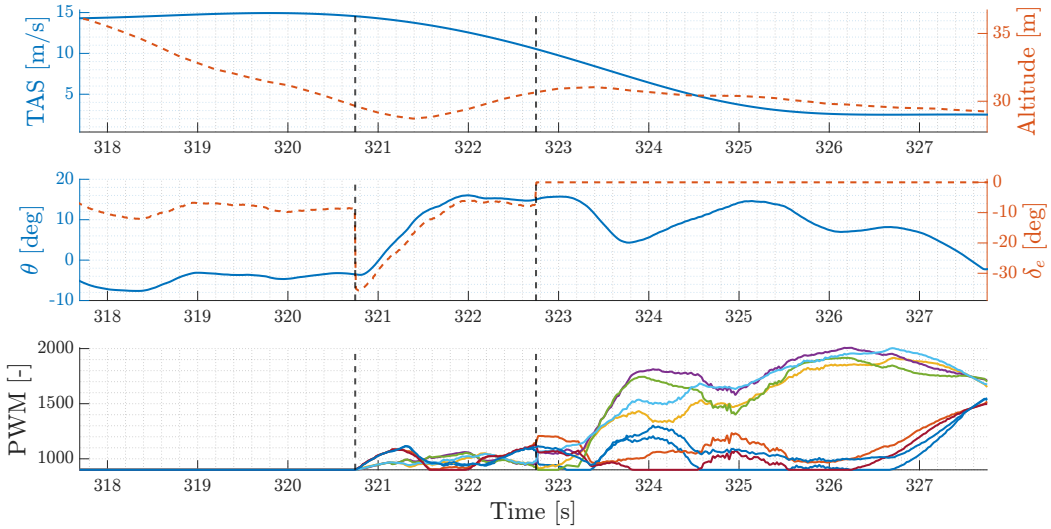

Figure 4.17: Improved backtransition executed with 2 seconds duration and 2 seconds ramp-up

more controlled rotation about the pitch axis, these higher pitch angles should be considered in the overall assessment.
In conclusion, the backtransition phase is characterized by a double pitch-up behaviour. The first pitch-up aims to slow the aircraft down by utilizing the thrust generated by the vertical motors and aerodynamic drag during the set duration. The second pitch-up is directed at completely stopping the aircraft once the duration has passed and residual airspeed is present.
Table 4.5 provides a concise summary of the results obtained with the different combinations of parameters, facilitating a straightforward comparison. The combination of a 2-second duration and 2-second ramp-up achieved the lowest pitch angle. However, the default settings exhibited the most uniform PWM behavior, allowing for a gradual attitude adjustment and deceleration. Despite the different settings, the complete stop of the aircraft consistently occurred slightly beyond the maneuver's duration, requiring approximately 50 meters of ground distance. Further testing could explore the maneuver's execution with entry airspeeds closer to the minimum, potentially enabling smoother and shorter deceleration and a more precise stopping position, thereby reducing the pilot's workload.

Additional observations

While not strictly part of the backtransition phase, the descent of the aircraft immediately following the maneuver presented its own peculiarities, particularly related to the vertical speed during descent. Given the large wing surface of the

[1]Calculated as the difference between the maximum and the minimum altitudes achieved before complete stop.

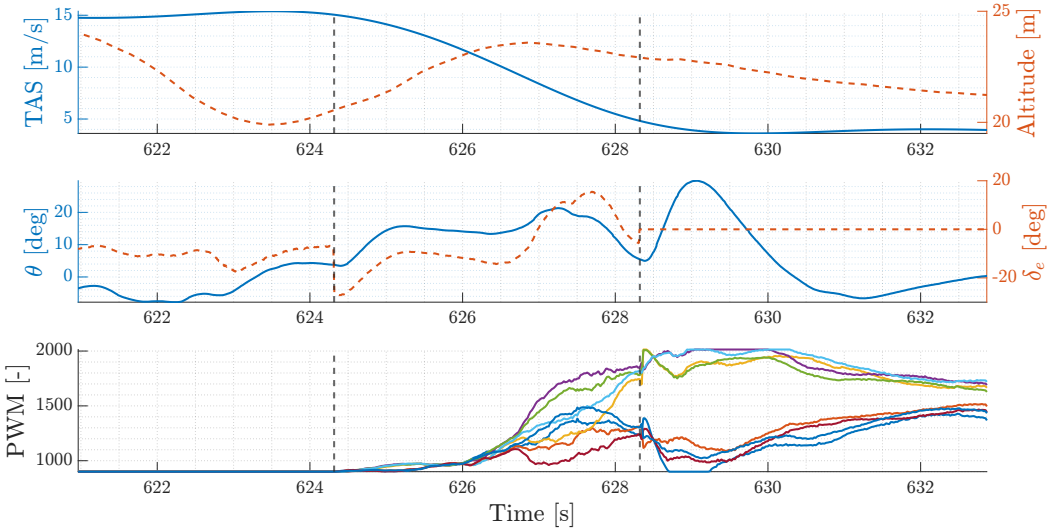

Figure 4.18: Backtransition executed with the default parameters, 4 seconds duration and 3 seconds ramp-up

Parameters	V_{TAS} [m/s]	Distance [m]	θ_{max} [deg]	ΔH_{max}[1] [m]
DUR = 2 RAMP = 1	16.3	46	43.8	-9
DUR = 2 RAMP = 2	14.6	50	16	+2.4
DUR = 4 RAMP = 3	15.3	48	29.8	+3.4

Table 4.5: Backtransition performance summary with different parameter combinations

aircraft, the vertical speed during descent becomes a critical parameter for safe and controlled execution; excessive speed, especially in the presence of wind and gusts, can result in a "falling-leaf" behaviour characterized by reduced maneuverability and uncontrolled attitude, as illustrated in Figure 4.19.

After the backtransition phase (denoted by the two vertical dashed lines on the left-hand side of the plots in Figure 4.19), the aircraft is observed descending at a rate of approximately 2 m/s, oscillating in both pitch and roll between -20 and 20 deg.

Throughout the descent phase, the PWM of the vertical motors remains constantly saturated, resembling the behaviour detailed in Section 4.1 associated with the MR controller's yaw control action. This situation limits maneuverability for the pilot, intermittently leaving the motors unresponsive. As the aircraft gets closer to the ground, the vertical velocity increases, and intense oscillations occur due to

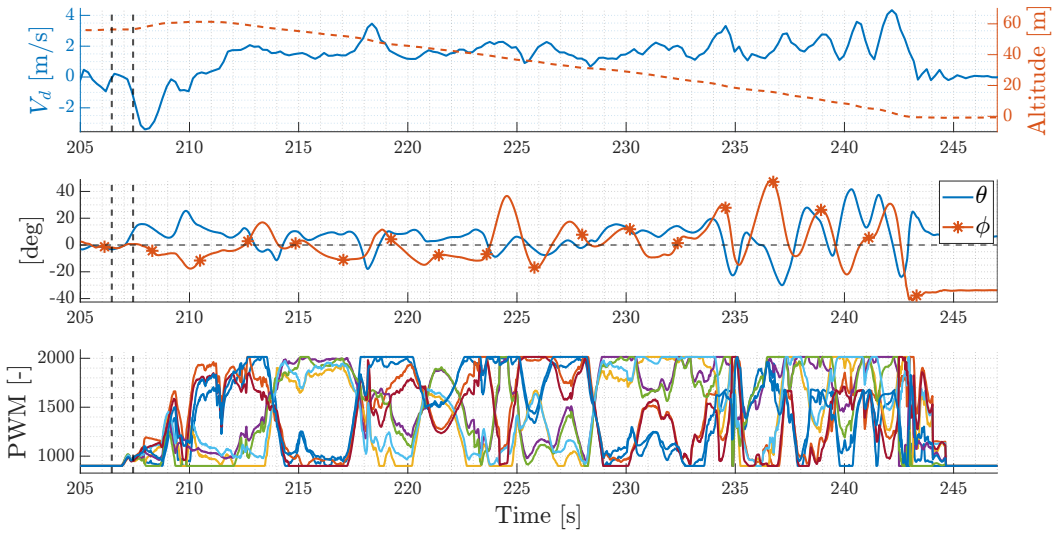

Figure 4.19: Falling-leaf behaviour encountered during fast descent

the instability of the attitude. Bank angles reach up to 48 deg, and pitch angles reach up to 41 deg. Eventually, the pilot manages to regain complete control of the aircraft and safely land it without any damage to the components.
Subsequent testing and consolidated experience led to the determination of an optimal descent rate between 1 and 1.5 m/s, allowing for straight and safe landings. This observation emphasizes the importance of carefully managing descent parameters for stable and controlled landings.

Chapter 5

Fixed-wing flight testing

Following the initial tests on the multirotor configuration of the VTOL, this chapter delves into the comprehensive evaluation of the fixed-wing flight characteristics. Through a series of focused tests, key aspects are explored such as wind estimation, drag polar, stall speed, and acceleration performance. Each section provides a meticulous examination of the test objectives, execution, data processing, and results, shedding light on the aerodynamic behavior of the experimental eVTOL in fixed-wing flight configurations. The insights gained from these tests form a crucial foundation for understanding the overall flight performance and guide further refinements in the design and testing process.

5.1 Wind estimation

Throughout a flight test campaign, the estimation of wind velocity and direction is a crucial element. This estimation serves a dual purpose: assessing the feasibility of tests under prevailing weather conditions and optimizing the execution of those tests by minimizing or maximizing crosswind effects, depending on specific objectives. Information about air and wind conditions is often sourced also from meteorological ground stations, offering redundancy and continuous data updates over time. Given the unavailability of a portable meteorological ground station, the necessity to perform the estimation through an in-flight test arose and the chosen method was the one referred to as "GPS Method", presented by the FAA in AC23-8C [33]. The GPS Method relies on a GPS unit to determine ground speed, from which wind velocity and direction are calculated. It also provides the true airspeed, which, in other contexts, is the primary objective of the test. It is worth noting that true airspeed calibration is essential for larger aircraft; however, smaller drones, such as the VTOL aircraft under examination, undergo a simplified calibration procedure during startup on the ground, eliminating the need for in-flight calibration.

5.1.1 Test objective and execution

The primary objective of the GPS Method test, as previously mentioned, is the determination of wind conditions. This information plays a pivotal role in the accurate execution of subsequent flight tests. The procedure of the GPS Method is as follows:

1. stabilize the aircraft in steady level flight at the desired test speed and record indicated airspeed and altitude;
2. record both ground track GTr and ground speed GS once these values stabilize;
3. initiate a 60 to 120-degree turn in either direction while maintaining the same airspeed and altitude. Record new ground track and ground speed data once stable on the new heading;
4. repeat the turning procedure with another 60 to 120-degree turn in the same direction, recording a third set of ground track and ground speed data;
5. resume regular flight.

This systematic approach ensures the derivation of accurate wind velocity and direction data.

5.1.2 Data processing

The success of this method relies on certain assumptions: the true airspeed remains constant during all legs of the flight, and the wind does not change during the execution of the test. The recorded data is then processed using a simple spreadsheet, which takes as inputs the ground speed and track for each flight leg and the indicated airspeed shared by all legs. First, for each of the legs flown as illustrated in Figure 5.1, the ground speed GS_i is decomposed in its east and north components, respectively X_i and Y_i, with $i = 1, 2, 3$:

$$\begin{aligned} X_i &= GS_i \sin(360 - GTr_i)\,, \\ Y_i &= GS_i \cos(360 - GTr_i)\,. \end{aligned}$$

These calculations lead to the determination of two pairs of intermediate terms, M_1, B_1 and M_2, B_2:

$$\begin{aligned} M_1 &= -\frac{X_2 - X_1}{Y_2 - Y_1}\,, \\ B_1 &= \frac{Y_1 + Y_2}{2} - M_1 \frac{X_1 + X_2}{2}\,, \end{aligned}$$

and

$$M_2 = -\frac{X_3 - X_1}{Y_3 - Y_1}\,,$$
$$B_2 = \frac{Y_1 + Y_3}{2} - M_2\frac{X_1 + X_3}{2}\,.$$

The final steps involve the calculation of two wind components, W_x and W_y:

$$W_x = \frac{B_1 - B_2}{M_2 - M_1}\,,$$
$$W_y = M_1 W_x + B_1\,.$$

Ultimately, the wind speed, wind direction and true airspeed are determined as:

$$V_{wind} = \sqrt{W_x^2 + W_y^2}\,,$$
$$W_{dir} = mod(540 - \arctan\left(\frac{W_x}{W_y}\right), 360)\,,$$
$$V_{TAS} = \sqrt{(X_1 - W_x)^2 + (Y_1 - W_y)^2}\,.$$

The module operation between two numbers, denoted as $mod(a, b)$, returns the remainder of the division of a by b; in this context, it is used to constrain the result of the wind direction to a range of 360 degrees.

5.1.3 Results

Once flights were consistently completed successfully, the wind estimation test was conducted during the first flight of each day at the field. These estimations provided an initial assessment of the prevailing wind conditions. Figure 5.1 illustrates the trajectory of one of the tests. Table 5.1 presents samples of data recorded during two of these tests and the results obtained by applying the procedure discussed in Section 5.1.2. These results have primarily been used to assess the quality of subsequent test points by analyzing the aircraft's heading relative to the determined wind direction. It is crucial to note that the wind conditions during the campaign were highly variable, ranging from days with calm weather, as observed during the second test in Table 5.1 with just 0.6 m/s of wind, to days with stronger winds and rapidly changing directions.

5.2 Stall speed estimation

In the field of aeronautics, a comprehensive understanding of the stall phenomenon holds paramount importance. A stall occurs when an aircraft's wing temporarily

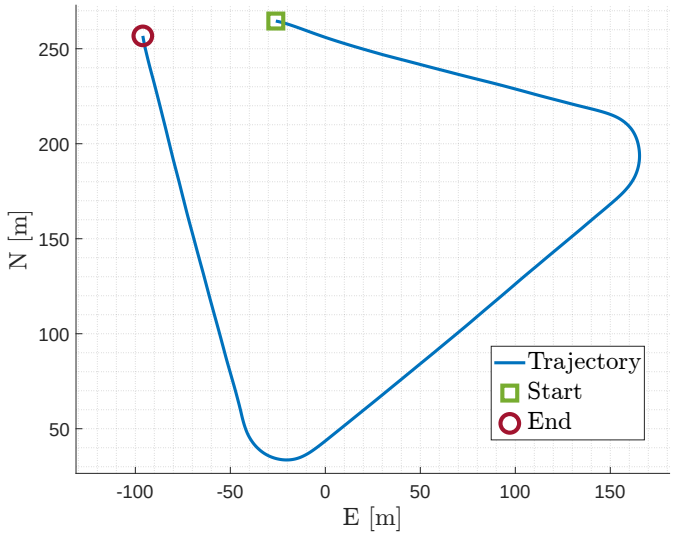

Figure 5.1: Trajectory of October 5th wind estimation test

Parameter	July 27th	October 5th
IAS [m/s]	18.2	15.1
GS_1 [m/s]	16.2	15.4
GTr_1 [deg]	115	100
GS_2 [m/s]	18.6	14.4
GTr_2 [deg]	1	226
GS_3 [m/s]	18.3	14.5
GTr_3 [deg]	166	336
TAS [m/s]	19.2	14.8
V_{wind} [m/s]	3.3	0.6
W_{dir} [deg]	183	354

Table 5.1: Example of wind estimation tests data and results

loses its capacity to generate sufficient lift, resulting in a loss of control and a potential descent in altitude. This phenomenon is a critical aspect of flight testing, as it enables the development of effective recovery procedures to ensure the safe and efficient operation of an aircraft within its flight envelope. As a result, identifying the stall characteristics must be established early in any flight test program.

Determining the stall speed is a challenging task due to the difficulties in precisely measuring position errors at high angles of attack that affect the airspeed measure, and in pinpointing the precise moment when a stall occurs during flight. Furthermore, the installation on the controller of custom flight modes for automatic testing was not an available option at the time of the current work, forcing the team to opt for a manual execution using the manual with permanent stabi-

lization control mode. This introduced a significant challenge to the pilot, who had to maintain the aircraft leveled and at constant altitude solely relying on visual cues and the data available through telemetry, as detailed in Section 1.4.2.

5.2.1 Test objectives and execution

The primary objective of this test is to determine the stall speed of the aircraft and gain insights into its behaviour during a stall, as well as its recovery characteristics. This is achieved through the following testing procedure:

1. align the aircraft properly with the field, accounting for wind direction to minimize sideslip angle;
2. trim the aircraft at 1.5 times the predicted stall speed;
3. set the throttle to 0 and maintain level flight using elevator commands exclusively;
4. allow the aircraft to decelerate and enter a stall;
5. during the stall and descent, attempt to regain level flight using elevator commands, if possible;
6. increase throttle and resume the regular flight.

To define the stalling speed, at least five tests have to be performed to ensure a large enough statistical sample and valid data [34].

5.2.2 Data processing

The initial phase of post-processing involves identifying the stall event. This event can be either aerodynamic, characterized by sudden variations in attitude angles, typically pitch or roll, or mechanical, marked by the elevator reaching its deflection limit. Test points that lack a noticeable break in attitude and do not reach the mechanical limit of the elevator are discarded. Another reason for rejecting a test point is a significant variation in altitude during its execution. This is important because the rate at which the aircraft decelerates into the stall event plays a crucial role. In light of these criteria, Figure 5.2 illustrates one of the valid tests, with the stall event highlighted at the moment of a pitch angle break.
The stall speed, denoted as V_{stall}, is pinpointed at the precise moment of the event, and the corresponding time is recorded. Subsequently, the airspeed equal to $1.1 \times V_{stall}$ is identified, with the associated time also recorded. The entry rate is calculated as $e.r. = -0.1V_{stall}/\Delta t$, where Δt is the time span between the

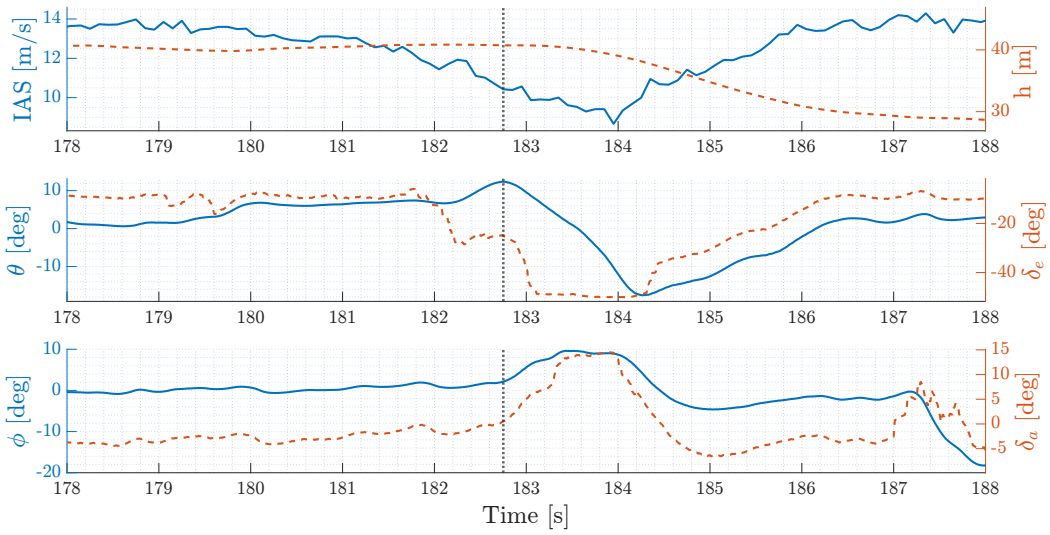

Figure 5.2: Example of a valid stall test execution; the vertical dotted line indicates the stall event

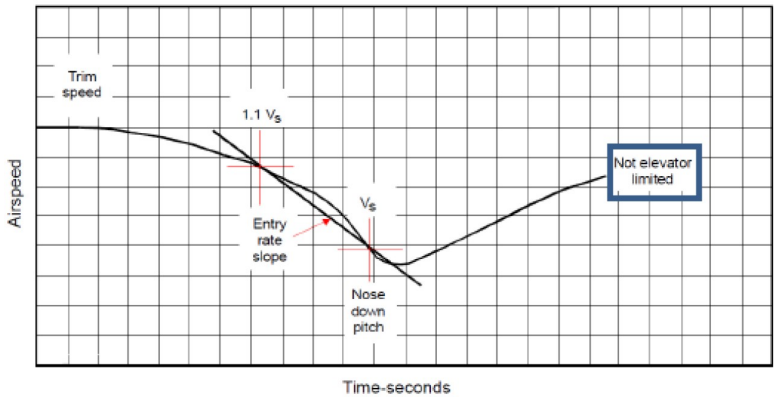

Figure 5.3: Entry rate determination for a stall test (source [8])

stalling event and the occurrence of an airspeed equal to $1.1 \times V_{stall}$. Figure 5.3 graphically represents this procedure.
Lastly, a linear regression of deceleration against airspeed is performed, yielding the stall speed as the airspeed corresponding to the standard entry rate of -1 kt/s^2 (-0.514 m/s^2). No further data reduction is necessary since the aircraft's weight remains constant throughout the test and does not require correction.

5.2.3 Results

Throughout all the tests, the observed stalling behavior consistently displayed aerodynamic characteristics, specifically marked by a pitch break followed by an increase in roll angle concurrent with the loss of altitude. This pattern is illus-

trated in Figure 5.2, providing a visual reference. No alternative stall dynamics were identified. This is primarily due to the aircraft's single configuration, which differs from the varied take-off, landing, and cruise configurations typically found in conventional aircraft equipped with landing gears and/or high-lift devices. The results of the conducted tests and their entry rates are summarized in Table 5.2.

Test	V_{stall} [m/s]	Entry rate [m/s^2]
A	10.4	-1.30
B	9.5	-4.77
C	9.3	-1.44
D	9.9	-3.30
E	10.4	-2.98
F	10.6	-4.60

Table 5.2: Stall test points results

The linear regression of the data is shown in Figure 5.4. The maximum lift coefficient associated with the obtained stall speed is calculated from the vertical equilibrium between lift and weight as

$$C_{L_{max}} = \frac{2W}{\rho V_S^2 S}\,.$$

The results of the tests are promising when compared to the original design values; during preliminary design, the maximum lift coefficient was set equal to $C_{L_{max}} = 1.17$ with an associated stall speed of $V_S = 11$ m/s for a $MTOM = 4.4$ kg ([1]). Despite the significant increase in weight to the current $MTOM = 6$ kg, the upgrades discussed in Chapter 2, resulted in a lower stall speed equal to $V_S = 9.9$ m/s with a maximum lift coefficient of $C_{L_{max}} = 1.255$.

5.3 Drag polar estimation

The drag polar, a fundamental component of an aircraft's aerodynamic characteristics, establishes a relationship between the drag coefficient, C_D, and the lift coefficient, C_L. This relationship serves as a critical tool for comprehending and optimizing the aircraft's performance across its operational range. Various methods exist for determining drag through flight testing, such as the speed power method, glide flights, and incremental power method [34]. The chosen method for this study is the trimmed level-flights method, in which the aircraft is trimmed at a specific airspeed while maintaining a constant altitude and constant throttle setting. This method relies on the equilibrium between thrust and drag during level and unaccelerated flight. Therefore, being able to precisely determine the thrust produced by the propellers in any given flight condition is paramount for

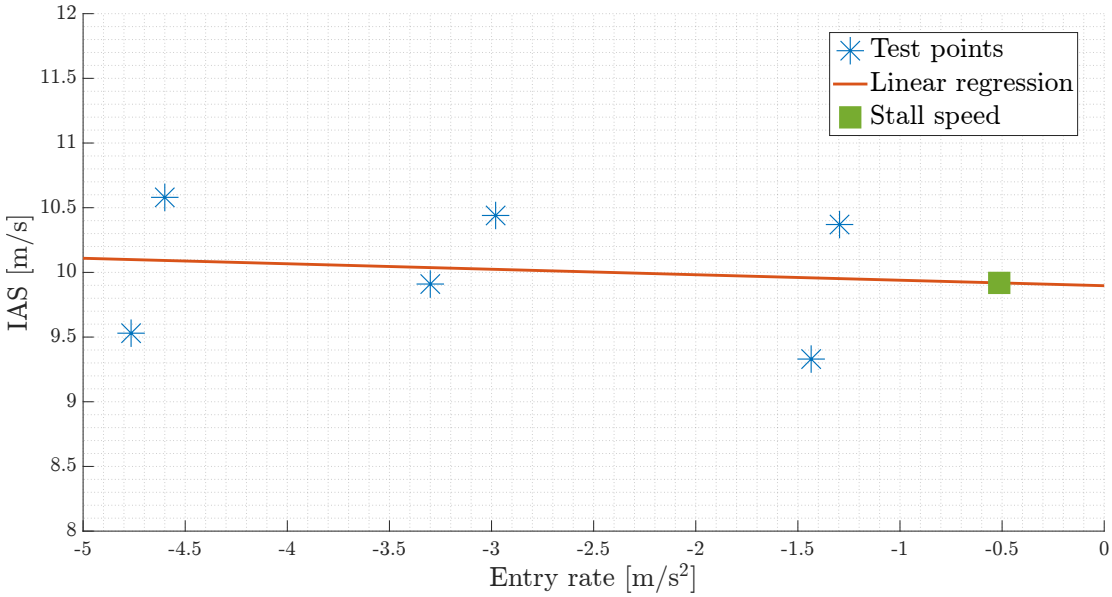

Figure 5.4: Linear regression of stall tests data

the method to work and minimize the estimation error. This condition is fulfilled through the wind tunnel tests previously discussed in Chapter 3.

5.3.1 Test objectives and execution

The primary goal of trimmed flight tests is to establish the drag polar curve by estimating lift and drag coefficients at various airspeeds, spanning from just above stall speed to the maximum speed. Additionally, the drag polar curve provides key performance parameters, including the aircraft's parasitic drag coefficient, C_{D_0}, and the lift induced factor, K, enabling the determination of other associated performance, such as maximum efficiency and velocity of minimum drag. The strength of the chosen method, main reason for which it was chosen over the other options, lies in its relatively straightforward execution and the minimal need for sophisticated instrumentation; however, the challenge is hidden in the accurate determination of the thrust produced, considering the intricate aerodynamics of propellers and the multitude of factors influencing their efficiency.
The test execution involves the following steps:

1. align the aircraft with the field to maximize the distance traveled and minimize crosswind effects;

2. set the desired throttle value and stabilize the aircraft at constant altitude and airspeed;

3. maintain the flight condition for as long as possible, then initiate a turn, and repeat at the predetermined throttle values.

Ideally, the test should be repeated multiple times for each throttle value, ranging from the minimum required for stable flight to maximum throttle, with increments of 5%. Due to the tests being executed with manual control mode active, setting precise throttle values was challenging. The pilot relied on his expertise to establish the test points defined in the pre-flight briefing and stabilize the aircraft for the required duration.

Validity constraints

To enhance data reliability, each test point underwent evaluation based on specific validity constraints, resulting in the selection of tests with the highest reliability. The constraints, outlined without a specific order, are:

- constant throttle value;
- airspeed excursion bound within 10% of the mean value;
- altitude variation limited to ±5 m from the mean value;
- minimum test duration of at least 10 seconds[1];
- maximum roll angle constrained within ±10 deg.

The application of the mentioned constraints to the 66 test points performed led to the exclusion of 22, primarily due to the constraints related to duration and maximum airspeed excursion.

5.3.2 Conventional equations

Once reliable test points are identified, the common procedure involves making specific assumptions to simplify the general horizontal and vertical equilibrium equations, facilitating the immediate calculation of lift and drag coefficients [34]. These assumptions are:

- level flight, $\gamma = 0$;
- steady flight, $V = constant$;
- no sideslip angle, $\beta = 0$;
- small angle of attack, $\alpha << 1$;
- high lift-to-drag ratio, $L >> D$.

[1]Constraint relaxed to a minimum duration of 5 seconds during the analysis to include more points.

Subsequently, the lift and drag coefficients can be calculated as:

$$C_L = \frac{2\,Mg}{\rho V^2 S}\,; \tag{5.1}$$

$$C_D = \frac{2\,T}{\rho V^2 S}\,. \tag{5.2}$$

In these equations, ρ is the air density, V is the true airspeed, M denotes the aircraft mass, and T indicates the produced thrust.

5.3.3 Corrected equations

Given that the aircraft under study exhibited higher susceptibility to external disturbances and altitude variations compared to larger aircraft, in pursuit of enhancing the precision of coefficients estimation and, consequently, the accuracy of calculated performance, several assumptions have been discarded, retaining only the high lift-to-drag ratio and the absence of sideslip.

Flight path angle correction

This correction addresses variations in altitude; although all the valid test points adhered to the previously discussed validity constraint, taking into consideration the altitude fluctuations has been deemed necessary, acknowledging the deviation from the constant altitude assumption. Being the flight path angle γ different from zero during part of the tests, the aircraft weight had to be decomposed into two components; consequently Equations (5.1) and (5.2) become:

$$\begin{aligned} C_L &= \frac{2}{\rho V^2 S} Mg\cos\gamma\,, \\ C_D &= \frac{2}{\rho V^2 S}\left(T - Mg\sin\gamma\right)\,. \end{aligned}$$

The flight path angle is not directly available in the recorded onboard data. However, its derivation is straightforward when the vertical velocity of the aircraft, V_v, and its airspeed, V, are known. Assuming still air, γ can be calculated as

$$\gamma = \arcsin\left(\frac{V_v}{V}\right)\,.$$

Angle of attack correction

In the analysis of level flights, it is often assumed that the angle of attack is small enough to be neglected. Dropping this assumption allows to account for the fact that the thrust vector is not always perfectly aligned with the wind speed vector.

Similar to the flight path angle, the angle of attack is not directly available in recorded data due to the absence of an AoA sensor onboard. However, it can be derived from the pitch angle and the flight path angle as:

$$\alpha = \theta - \gamma \, .$$

This correction introduces a component of the thrust T in the lift coefficient equation and impacts the one already present in the drag coefficient equation; the obtained equations are the following:

$$C_L = \frac{2}{\rho V^2 S} \left(Mg \cos\gamma - T \sin\alpha \right) \, , \tag{5.3}$$

$$C_D = \frac{2}{\rho V^2 S} \left(T \cos\alpha - Mg \sin\gamma \right) \, . \tag{5.4}$$

Accelerations correction

The final and most crucial correction affecting the coefficients calculation involves the longitudinal and normal accelerations of the aircraft. The longitudinal acceleration, denoted as $a_x^{\mathcal{S}}$, is computed as the x-axis acceleration derived from transforming the IMU-measured accelerations from the body reference frame to the stability reference frame. Similarly, the normal acceleration, denoted as $a_z^{\mathcal{S}}$, is obtained as the z-axis acceleration using the same transformation. By incorporating these two acceleration terms into Equations (5.3) and (5.4), the lift and drag coefficients are calculated as follows:

$$C_L = \frac{2}{\rho V^2 S} \left(Mg \cos\gamma - T \sin\alpha - Ma_z^{\mathcal{S}} \right) \, , \tag{5.5}$$

$$C_D = \frac{2}{\rho V^2 S} \left(T \cos\alpha - Mg \sin\gamma - Ma_x^{\mathcal{S}} \right) \, . \tag{5.6}$$

Equations (5.5) and (5.6) account for all the elements in the vertical and horizontal forces equilibrium; in this study, for the previously mentioned purposes, these are used instead of the simplified versions presented in Equations (5.1) and (5.2).

5.3.4 Data processing

The first step in data processing is to filter the data, as presented in Section 1.4.3; then the coefficients can be calculated using Equations (5.5) and (5.6). For larger aircraft, data is usually hand-recorded, given that tests last as long as several minutes and parameters do not vary quickly over the duration, eliminating the necessity for automatic data recording devices [34]. This manual recording method leads to each parameter assuming one single value during a test; the final result of this is a drag polar curve composed of several points, each one associated with a

test. The numerical equivalent of this procedure, considering the large amount of data automatically recorded, is the averaging of the parameters over the duration of each test point.

Taking into account the variability of the data, the shorter duration of the tests and the effort of the current study to provide deeper insights about the aircraft's performance despite the many limitations encountered, the averaging step has been discarded; reducing all of the information captured from the application of Equations (5.5) and (5.6) to averaged values would nullify the effort and produce results with excessive uncertainty. The result of this choice is the cloud of points that can be observed in Figure 5.5. To facilitate the analysis, each test has been color-mapped based on the day of execution.

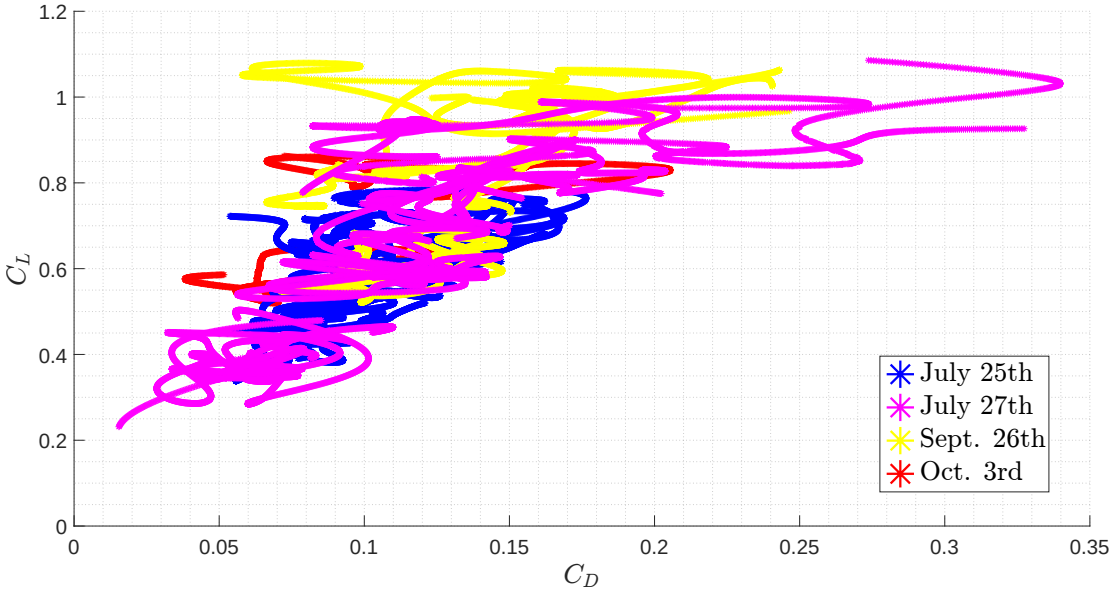

Figure 5.5: All drag polar points color-mapped by the day of execution

Notably, flight tests were mainly conducted in two periods: at the end of July, specifically on the 25th and 27th, and between the end of September and the first days of October, namely September 26th and October 3rd. Flights performed in September and october were intended to obtain data related to low airspeed flight, being these speed regime not well represented in july dataset. This observation becomes relevant when two different trends can be observed in the plotted points.

in the low airspeed region: flights performed in September present value of drag coefficient which are lower with respect to July flights

This unexpected discrepancy has been thoroughly investigated, and some plausible causes have been identified; causes of aerodynamic nature have been ruled out since the aircraft flew with the same configuration in all the tests and did not undergo modifications.

Outside air temperature condition

The initial focus of the investigation was on the potential impact of outside air temperature on air density, Mach number, and Reynolds number. A notable deviation in the outside air temperature from the temperature in the wind tunnel's test chamber could affect the accuracy of thrust estimation in the polynomial model discussed in Section 3.3.2. This, in turn, directly influences the quality of the calculated drag coefficient.
While the impact of temperature on thrust has been previously studied and was initially considered negligible due to the limited temperature difference between the field and wind tunnel tests, a more comprehensive examination was conducted. Considering the +6°C difference registered from July's tests compared to the wind tunnel's temperature, a 1% reduction in the thrust coefficient caused by Reynolds number, obtained through the procedure detailed in Section 3.5, along with an approximately 2% reduction in air density, were taken into account to correct the thrust estimation. Similarly, for the -3°C difference observed in the September and October cases compared to the wind tunnel, a 0.5% increase for the thrust coefficient and a 1% increase for air density were applied. However, applying this correction did not yield a significant improvement in aligning the results from the two periods. This further confirms the conclusion that such a small temperature difference is negligible for the purposes of the current work.

Stabilization issues

Some stabilization issues have been encountered during the flight testing, especially when trimming the aircraft at low airspeeds. This problem is related also to the fact that the drone was piloted in manual mode without any automatic flight mode that allows an effective and easy stabilization.
While flying at low airspeed, also, the susceptibility of the aircraft at external disturbancies made it more difficult to execute properly the test. In addition, the limited flight test range available presented some challenges in the stabilization of the aircraft at a particular speed.
Looking at Figure 5.5, it can be observed that points in the high C_L region (*i.e.,* flight at low airspeed near the stall one) are sparse. This behaviour is mainly attributed to the stabilization problem mentioned above, also considering that this region of airspeed is near the stall one. In fact, in some of the tests performed and discarded according to the constraints in Section 5.3.1, the aircraft entered into a stall while performing trimmed flights at low airspeed.

Datasets and polynomial fitting

In light of the different trends that showed up in the data, the analysis incorporated two distinct datasets:

- data collected during valid tests from July;
- entire database of valid trimmed flight tests performed during the campaign.

Following the procedure presented in [16], each set of C_D and C_L data underwent a second-order polynomial fitting, represented by the equation:

$$C_{D,\text{par}} = C_{D_0,\text{par}} + HC_L + K_{\text{par}}C_L^2 \,.$$

This polynomial form can be reformulated for better interpretation as:

$$C_{D,\text{par}} = C_{D,\text{min}} + K(C_L - C_{L_{C_{D,\text{min}}}})^2 \,. \tag{5.7}$$

Here, $C_{D,\text{min}}$ denotes the minimum achievable drag coefficient, represented by the vertex point of the drag polar curve; correspondingly, $C_{L_{C_{D,\text{min}}}}$ denotes the lift coefficient at which minimum drag occurs. This model has been preferred to the conventional parabolic drag polar approximation defined as:

$$C_{D,lin} = C_{D_0} + KC_L^2 \,. \tag{5.8}$$

This preference arises because Equation (5.7) provides a more accurate representation of the aerodynamic characteristics of the aircraft. The incorporation of the minimum drag coefficient $C_{D,\text{min}}$ is crucial, as it acknowledges that drag is not solely dependent on lift, and its minimum value does not necessarily occur when no lift is being produced, (*i.e.,* when $C_L = 0$, as Equation (5.8) asserts, with C_{D_0} representing the aircraft's parasitic drag.

5.3.5 Results

The outcome of the second-order fitting applied to the datasets is illustrated in Figure 5.6.

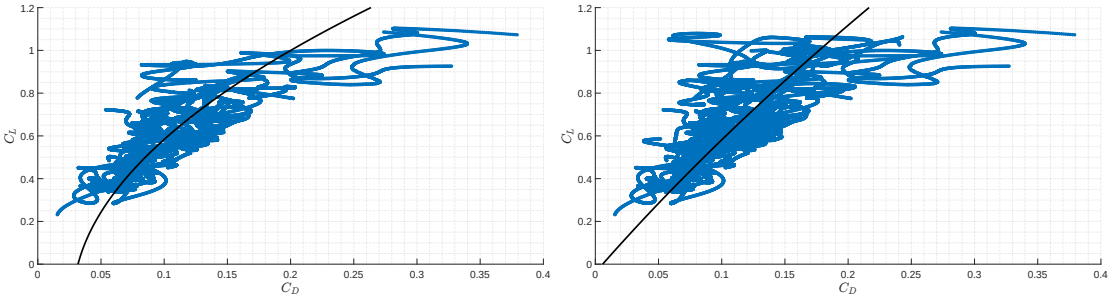

(a) Test points from July

(b) Test points from the entire database

Figure 5.6: Drag polar second-order polynomial fitting of the two datasets

A comparison between the numerical predictions from OpenVSP, as obtained in Section 2.3, and the fitting curves for the two datasets is illustrated in Figure 5.7.

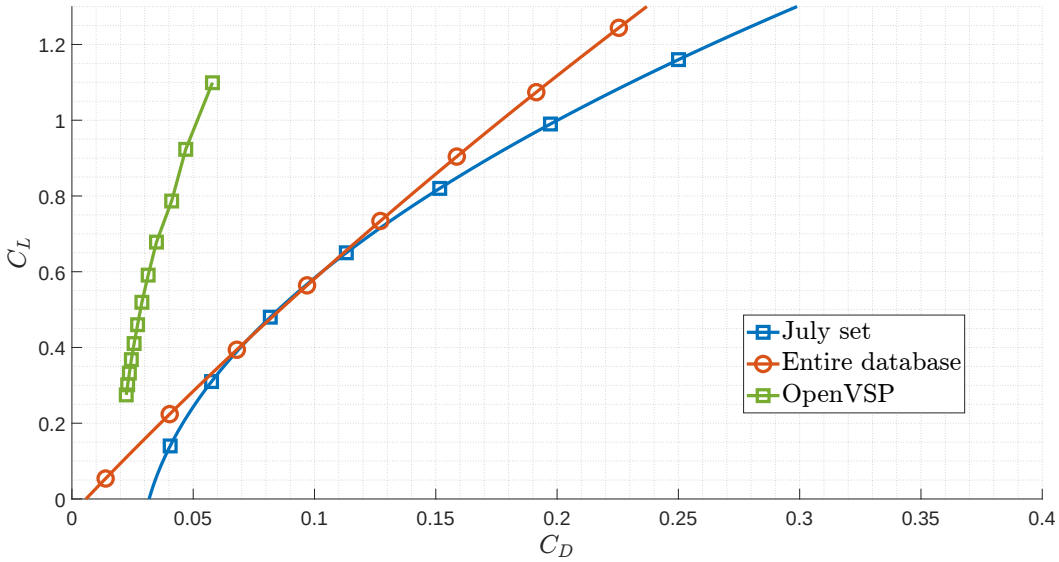

Figure 5.7: Drag polar comparison: fitting of the datasets vs. OpenVSP prediction

The first observation is the substantial deviation in drag coefficient values of the experimental results compared to the numerical predictions. This difference is presumed to partially arise from the omission of the eight vertical motors and their propellers in the OpenVSP model, as discussed in Section 2.3. Insights from various studies, such as [35] and [36], underscore the significant impact of a VTOL subsystem on a fixed-wing configuration. This influence results in a significant increase in drag, exceeding 30% compared to a clean configuration, and is accompanied by a reduction in the maximum lift-to-drag ratio reaching up to 40% [35]. The magnitude of this effect depends on dynamic variables such as pitch angle, airspeed, propeller diameter, propeller pitch, and their stopping position after the transition from vertical to forward flight. Contribution to this increase in drag is the absence of a feature in the mounted ESCs to control the propellers' stopped position. This limitation prevents the alignment of propellers parallel to the airflow during forward flight to minimize additional drag.

Furthermore, a significant portion of the increased drag is presumed to derive from the fuselage's design: the fuselage exhibits some aerodynamic inefficiency being characterized by flat vertical carbon-fiber plates in the front and rear portions supporting the motor booms, as depicted in Figure 4.6a, and a wide flat base designed to house the 3D printed board holding the electronic components, the fuselage exhibits aerodynamic inefficiency. For future developments, an upgrade to the vertical motors' ESCs, alongside a redesign of the fuselage's shape, is strongly suggested to optimize aerodynamic efficiency and overall performance. A summary of the coefficients obtained from the different datasets is presented in Table 5.3 and compared to the original design predictions.

Then, it can observed that the addition of September and October test points

	$C_{D,\min}$	$C_{L_{C_{D,\min}}}$	C_{D_0}	K
July dataset	0.02778	-0.181	0.03182	0.12360
Entire database	-	-	0.00579	0.02202
OpenVSP	-	-	0.02830	-
Original design ([1])	-	-	0.02300	0.04600

Table 5.3: Comparison of drag polar main parameters; '-' denotes not available data

to the database caused a reduction in the curvature of the fitting model. This behaviour is consistent with the previously discussed discrepancy in drag coefficient values, and invalidates the dataset composed of the entire database; from Table 5.3, this dataset exhibits an improbable parasitic drag coefficient of 0.00579. Consequently, only July's dataset is considered for comparison with the predicted coefficients.
The flight test data estimate a parasitic drag coefficient of 0.03182, 12.4% higher than the OpenVSP prediction of 0.0283; considering all the observations previously made about the aspects that the numerical method fails to account for, the prediction of C_{D_0} is quite accurate and can be further refined with improvements to the model. However, following the trend of the curves, with increasing lift coefficient the experimental curve deviates significantly from the predictions. This can be related to the lift-induced drag factor K, which is estimated to be equal to 0.1236. Unfortunately OpenVSP does not provide a specific value for this factor but only the trend of the curve, which graphically proves the misprediction, as visible in Figure 5.7. For the sake of comparison, the experimental value can be seen being approximately three times greater than the original design value, which is equal to 0.046, exposing deep differences between the predicted and the actual drag characteristics of the aircraft.
Considering the values of C_{D_0} of July dataset and openVSP numerical analysis, it can be stated that OpenVSP can be considered as tool for initial estimates of the drag characteristics; however, the differences shown highlight the necessity to enhance the model to better account for additional drag-producing components or to deploy a more capable aerodynamic software.

Additional results

In analyzing the dataset from July's flights, several key insights emerged, providing a comprehensive understanding of the aircraft's aerodynamic performance. The derivative of the lift coefficient with respect to the angle of attack was determined by calculating the slope of the linear regression applied to the associated data. The resulting value from flight testing was found to be $C_{L_\alpha} = 4.298$ 1/rad, slightly lower than the corresponding OpenVSP prediction of 4.927 1/rad. Figure 5.8 visually presents the comparison, showcasing the test points, the linear regression line,

and the OpenVSP prediction. Notably, the collected data lies to the right of the numerical prediction, indicating that the aircraft requires higher angles of attack to generate the same lift compared to the simulation results. In cruise conditions, the OpenVSP prediction suggested an angle of attack of -2 deg. However, the experimental data range spans approximately from -2 to 6 deg, with the linear regression yielding a value of 1.8 deg. Despite these higher values, the collected data demonstrated a satisfactory correlation with the prediction.

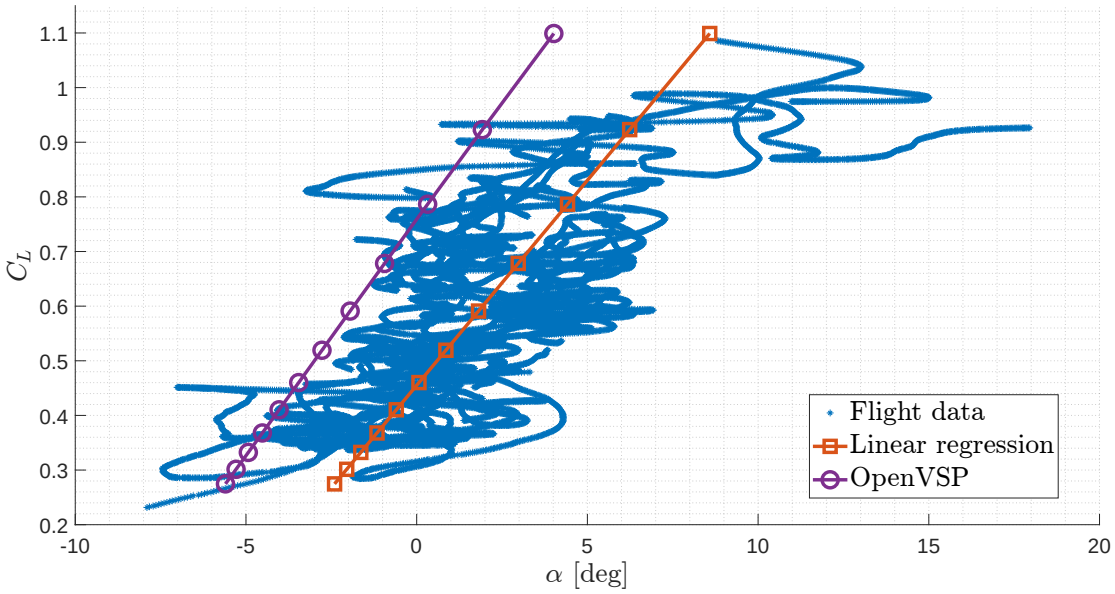

Figure 5.8: Comparison of experimental C_{L_α} vs. OpenVSP prediction

Subsequently, the assessment of the elevator's deflection against airspeed, as depicted in Figure 5.9, revealed a consistently negative deflection ranging from approximately -18 deg at an airspeed just above stall speed to a maximum of -5 deg over the flight envelope. A notable observation from both the numerical prediction and the experimental data is the limited utilization of the deflection range compared to the effective range of the servo-motors. Specifically, less than 15 deg of the available 110 deg range (ranging from -50 to 60 deg, as measured in [3]) have been exploited. This behavior aligns with the numerical prediction's suggestion that the elevator was significantly oversized, a known factor from previous theses [2]. Moreover, such a small deflection range imposes stringent requirements on the angular position accuracy of the servomotors to effectively trim the aircraft under all conditions.

Examining the cruise speed of 15 m/s, the expectation is for the elevator to be in a neutral position, with the trim condition granted by the horizontal tail's incidence angle (see Chapter 2). However, both the numerical prediction and flight data deviate from this expectation, showing 1.2 deg and a deflection range from -6 to -12 deg, respectively. These findings underscore the necessity for an

optimized resizing of the elevator, following the modifications discussed in Section 2.2. Lastly, the tail's incidence angle should be revised, specifically reduced, to compensate for the permanently negative deflection of the elevator, even at cruise speed. Addressing these aspects is crucial for achieving effective trim conditions and enhancing overall flight performance.
The stabilization issues presented above can be seen also in Figure 5.9: the elevator deflection in the ranges from 13 to 15 m/s and from 18 to 20 m/s are much more scattered with respect to the central part (airspeed from 15 to 18 m/s); it is due to the fact that the aircraft was difficult to stabilize at a precise airspeed, so the elevator was moved frequently during each test point.

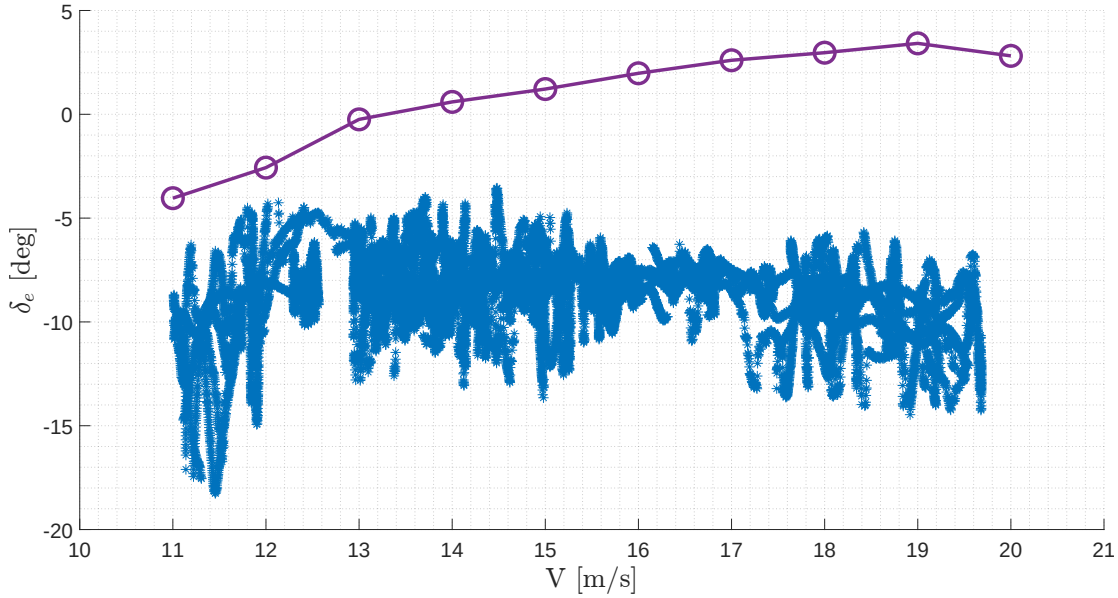

Figure 5.9: Experimental elevator deflection vs. airspeed compared to OpenVSP prediction

In conclusion, the obtained results provide a comprehensive overview of the aircraft's aerodynamic performance, serving as a foundation for future testing and iterative design processes. The drag estimation has been noted to be highly optimistic, significantly underestimating the lift-induced component of drag, which proved to be predominant from the collected data. The appearance of two different trends from the tests has been investigated and the problem is considered to be due to the difficulties in stabilizing the aircraft in certain conditions. However, during the current work, it has not been possible to pinpoint the specific causes for it, despite the different assumptions made. Further testing in a larger field and with the aid of custom control modes for test execution is suggested to obtain better data, mainly in the low speed region of the flight regime. Additionally, the execution of all tests during a short period of time is recommended to minimize variations in weather conditions and reduce thrust estimation uncertainty.

5.4 Acceleration performance

Accurately determining an aircraft's climb performance is paramount for various reasons, including safety, obstacle clearance, the definition of operational and maneuvering capabilities, and compliance with specific performance criteria required for certification. Traditionally, this assessment has been associated with the steady climb test, also known as "sawtooth climbs." However, this method involves full-throttle climbs of 3 to 5 minutes at various airspeeds and altitudes, demanding substantial time and flight space. Given the constraints of the available flying field and the absence of a control mode that allows for a fixed pitch angle during each climb, the sawtooth climb test is deemed suboptimal. As an alternative, an energetic approach, known as the Rutowski energy method [34], has been considered.

Energy approach

The Rutowski energy method is founded on the concept of the total energy possessed by an aircraft. This total energy combines potential energy associated with altitude and kinetic energy associated with airspeed, represented as:

$$E = Wh + \frac{WV^2}{2g},$$

where W is the aircraft weight, h is the altitude, V is the airspeed, and g is the acceleration due to gravity. Normalizing this equation by the take-off gross weight to allow for comparisons across different aircraft, the specific energy, denoted as E_S, is obtained as:

$$E_S = h + \frac{V^2}{2g}, \tag{5.9}$$

where $E_S = E/W$ [m]. Specific energy, or energy height, can be visualized as the maximum altitude attainable if all the aircraft's energy were converted into potential energy or as the maximum speed achievable if it were converted into kinetic energy. With this definition in mind, performance assessment involves evaluating the aircraft's ability to change its energy level within a specified timeframe. Differentiating Equation (5.9) with respect to time leads to:

$$\frac{dE_S}{dt} = \frac{dh}{dt} + \frac{V}{g}\left(\frac{dV}{dt}\right). \tag{5.10}$$

The left-hand side of this equation represents the specific excess power (SEP), a key parameter. Knowledge of SEP values allows the determination of either the rate of climb or the aircraft's acceleration capabilities. This approach also takes into account changes in weight during climbs or accelerations and often provides more precise results than conventional methods.

In flight testing, the challenge is to obtain accurate SEP values for a specific aircraft. It can be challenging to achieve a steady rate of climb, even in modern jet fighters, due to changes in true airspeed with increasing altitude. Consequently, level accelerations are a practical flight test method to leverage the energy approach and address this challenge. The concept involves maintaining $\frac{dh}{dt}$ at or near zero during the test by flying at a constant altitude. The aircraft's ability to accelerate is then measured and converted into values of SEP or the rate of climb (ROC) at the altitude under consideration.

5.4.1 Test objectives and execution

The primary objective of the level acceleration test is to obtain the climb performance parameters for the aircraft, including the specific excess power curve, the best rate of climb speed, and the best angle of climb speed. While originally designed for jet-propelled aircraft, this method can also be effectively applied to propeller-driven aircraft. The test procedure is as follows:

1. properly align the aircraft with the field to maximize the distance traveled;
2. reduce the aircraft's speed to slightly above stall speed and stabilize it at the test altitude;
3. apply maximum throttle and maintain a constant altitude by adjusting the aircraft's pitch downward as airspeed increases;
4. reach the maximum level flight airspeed for a few seconds;
5. reduce throttle and resume regular flight.

Despite the apparent simplicity of this test, its application to the specific drone in question presented unique challenges. As mentioned earlier, the active control mode was manual with permanent stabilization, which meant that the pilot had full control over every aspect of the aircraft, with the controller assisting in maintaining level attitude. Given the intense and prolonged accelerations involved, maintaining a constant altitude by visual reference, with only the support of telemetry data, presented a significant challenge to the pilot. Nevertheless, the pilot successfully executed several tests.

5.4.2 Data processing

Validity constraints

The validity of each test has been assessed based on three main conditions:

- ensuring steady acceleration with sufficient stabilization time at the airspeeds at the beginning and end of the test;

- keeping the altitude variation within ±5 m with respect to the initial value;
- bounding the acceleration normal to the trajectory between ±2 m/s^2.

Properly stabilizing the aircraft at an airspeed just above stall and subsequently stabilizing it again upon reaching the maximum airspeed required more space than was available at the field. This necessitated initiating acceleration shortly after reaching the minimum speed and then commencing deceleration as soon as telemetry indicated no further airspeed increase. The normal acceleration bound, which is conventionally set at a maximum of $\pm 0.1g$ for larger aircraft (equivalent to approximately ±1 m/s^2), was relaxed for the relatively small drone: due to its significant susceptibility to gusts, the constraint was adjusted to $\pm 0.2g$, equivalent to ±2 m/s^2. Nevertheless, several tests had to be discarded due to prolonged excursions beyond the acceptable acceleration limits, particularly during the phase when the aircraft reached its maximum airspeed and experienced significant vibrations. An example of a rejected test is illustrated in Figure 5.10.

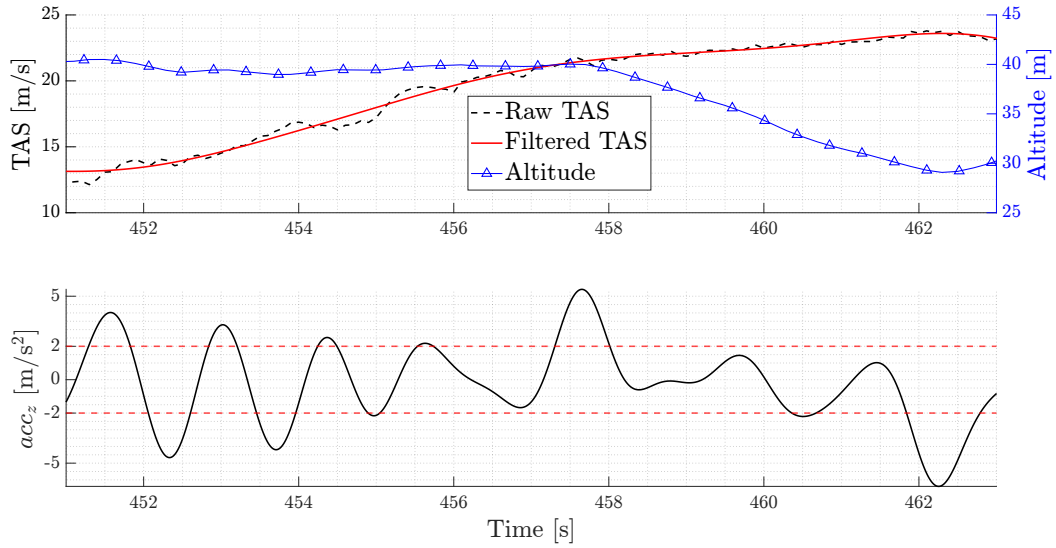

Figure 5.10: Example of a rejected level acceleration test, red dashed horizontal lines represent the normal acceleration boundary

Data reduction

Following the methodology outlined in [34], data reduction involves computing $\frac{dV}{dt}$ at evenly spaced airspeed increments. In case of deviations, $\frac{dh}{dt}$ is also determined for these airspeeds. Similar to the process used while obtaining the polar curve, $\frac{dV}{dt}$ is derived as the x-axis acceleration obtained by transforming IMU-measured accelerations from the body reference frame to the stability reference frame. Altitude variation is directly calculated from GPS data, where the aircraft velocities in the North-East-Down (NED) reference frame provide down velocity v_d:

$$\frac{dh}{dt} = -v_d^{\mathcal{N}} .$$

With these elements in place, after applying the data filtering detailed in Section 1.4.3, the specific excess power (SEP) can be determined as defined in Equation (5.10).

SEP curve fitting

Once the SEP is calculated from the available data, a fitting model is necessary to obtain a curve from which extract valuable performance. Rational models [37], alternatively known as rational functions, serve as a crucial tool for this purpose. The general expression is presented in Equation (5.11):

$$y = \frac{\sum_{i=1}^{n+1} p_i \, x^{n+1-i}}{x^m + \sum_{i=1}^{m} q_i \, x^{m-1}} , \tag{5.11}$$

where n is the degree of the numerator polynomial, and m is the degree of the denominator polynomial. Matlab's Curve Fitting Toolbox™ supports rational models with $0 \leq n \leq 5$ and $1 \leq m \leq 5$. The coefficient associated with x^m is always equal to 1, ensuring uniqueness in both the numerator and denominator when the polynomial degrees are the same. Rational models offer the advantage of flexibility when dealing with data that has a complex structure, as is the case with the SEP curve, which could not be adequately fitted using standard polynomials. However, it is important to note that rational models can become unstable when the denominator approaches zero.

5.4.3 Results

After filtering out the tests that did not meet the defined conditions, five level accelerations were kept and analyzed. Among these five, a few exhibited brief portions in which the normal acceleration limit was slightly exceeded; however, given their proper execution and adherence to the stabilization and altitude constraints, they were still considered acceptable. Table 5.4 summarizes these tests, along with their duration and maximum achieved airspeed. Notably, the average duration of an acceleration test was 11 seconds with a maximum achieved airspeed of 21.7 m/s, value that is perfectly aligned with the original preliminary design value of 22 m/s discussed in [1].

Climb performance

The analysis of the acceleration tests outlined in Table 5.4 resulted in the SEP curves depicted in Figure 5.11. It is worth noting that the challenges in meeting the stabilization at lower airspeed before the execution of the test had a slight

Test	V_{max} [m/s]	Duration [s]
A	19.6	11.0
B	19.4	10.6
C	20.8	12.3
D	21.7	12.5
E	21.4	8.2

Table 5.4: Valid level acceleration tests

impact on the curves: this is evident as three of the tests start their SEP curves at 11.5 m/s, while the other two commence between 12 and 12.5 m/s. The difference of less than 1 m/s did not affect the calculated performance. A minor manual correction was applied to align the two curves with those on their left for the purpose of fitting the data more smoothly.

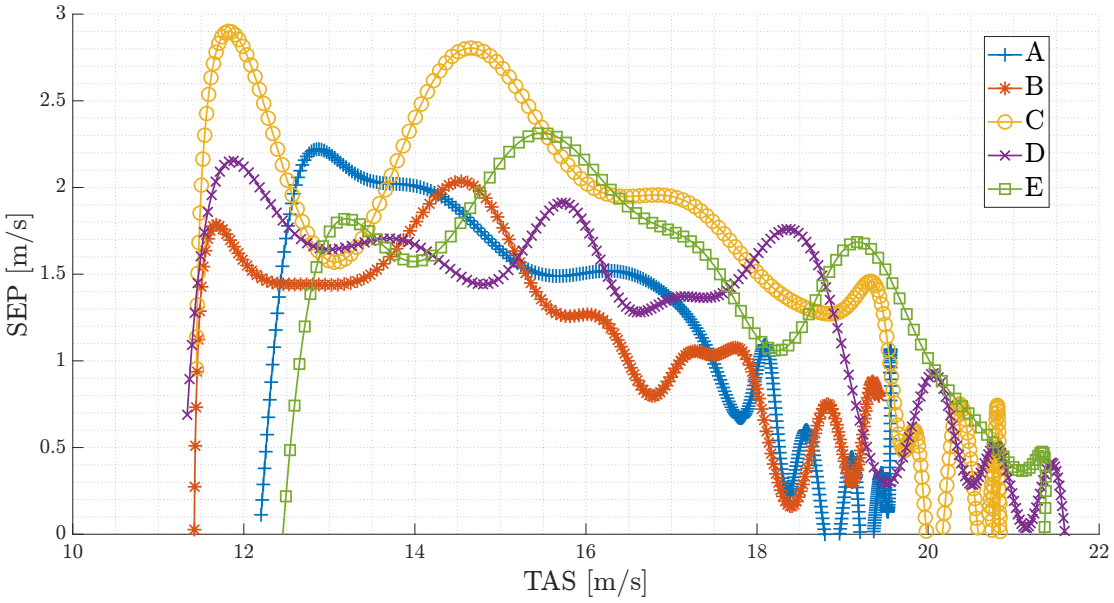

Figure 5.11: Specific excess power curves

After the alignment, Matlab's Curve Fitting Toolbox™ was employed to fit the data and derive a unique curve from which performance parameters could be extracted. Through a trial-and-error approach, a rational model with a second-order numerator and a first-order denominator in the form

$$SEP = \frac{p_1 V^2 + p_2 V + p_3}{V + q_1}$$

was determined as the most suitable model for the data. The coefficients for this rational model are presented in Table 5.5.

Coefficient	Value
p_1	-0.3369
p_2	10.77
p_3	-78.85
q_1	-11.1

Table 5.5: SEP rational model fitting coefficients

The final fitting curve and the associated best angle of climb and best rate of climb performance are illustrated in Figure 5.12.

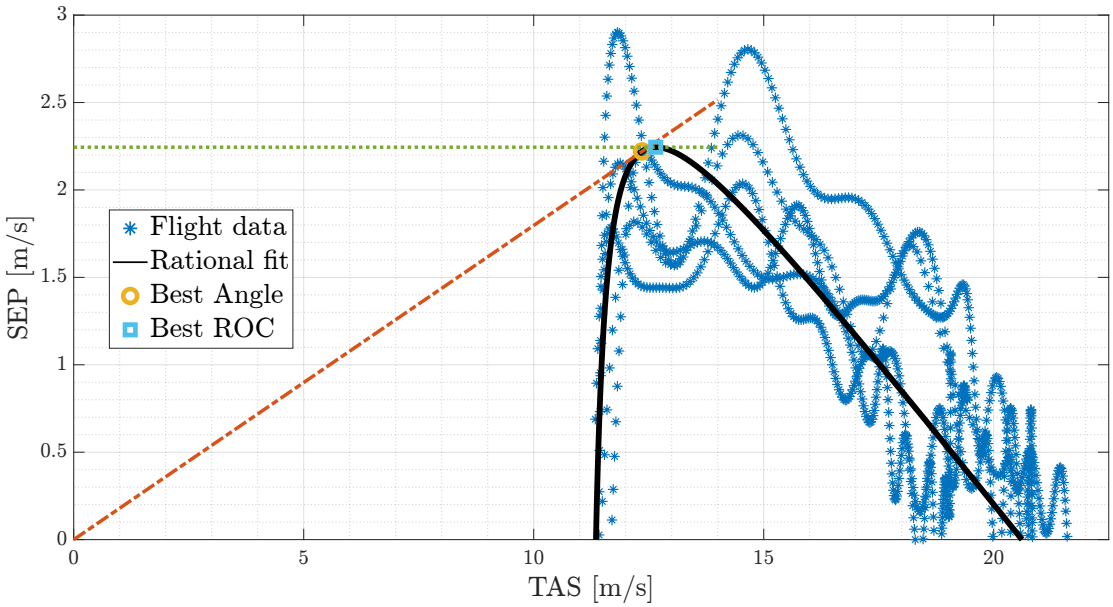

Figure 5.12: SEP fitting curve and associated performance

The best angle of climb airspeed is significant for optimizing obstacle clearance during take-off, even though this concern may not apply to VTOL aircraft. Nevertheless, the airspeed has been determined to be 12.35 m/s. Conversely, the best rate of climb airspeed represents the optimal airspeed for gaining altitude in the shortest time. In this context, it has been determined to be 12.65 m/s, with a maximum SEP equal to 2.45 m/s.

Acceleration characteristic behaviour

One intriguing discovery emerging from these tests is a distinctive behavior exhibited by this VTOL aircraft, which can be attributed to the positioning of its front motors. In Figure 5.11, a noticeable reduction in the SEP can be observed after the initial peak, followed by an increase and a subsequent gradual decrease to zero. This behavior is particularly pronounced in test C, while in the other

tests, the reduction is less pronounced and leads to a flat portion of the curve within airspeeds ranging from 12 to 14 m/s. To provide a visual representation of this phenomenon, Figure 5.13 depicts the pitching effect during test C.

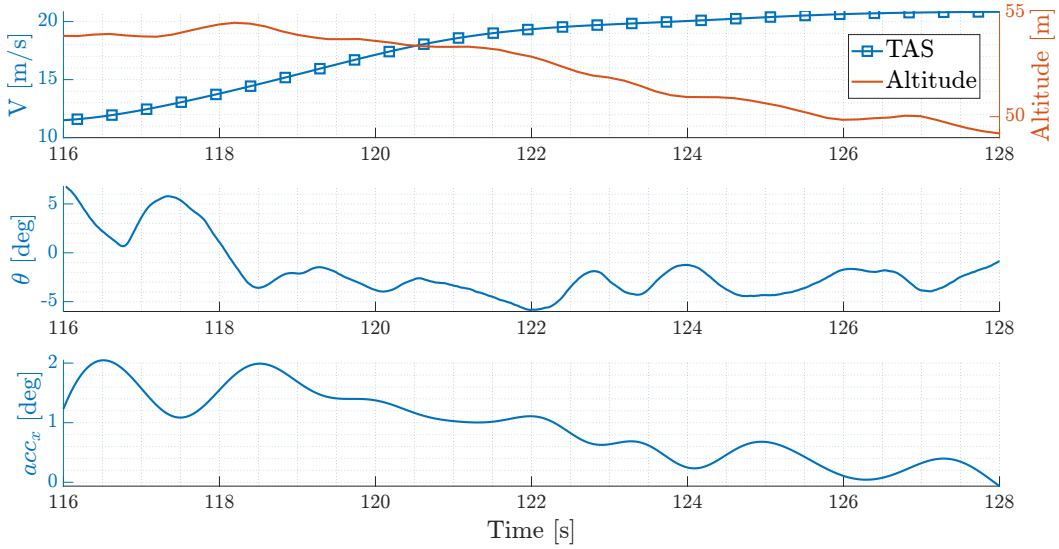

Figure 5.13: Pitching behaviour during test C

The observed pitching effect stems from the front motors' mounting position, which is slightly above the horizontal plane of the aircraft's CG. During full-throttle acceleration, this elevated mounting location induces a pitching moment that causes the aircraft's nose to pitch downward. The onboard controller's stabilized mode intervenes to maintain straight and level flight conditions, counteracting this pitching motion. As a result, an oscillation in the aircraft's pitching attitude is introduced, directly impacting the initial acceleration, and consequently, this behavior is reflected in the SEP curve as well. This finding is of significant importance and should be considered in future iterations of the design. Modifications to the mounting supports can be explored to align the thrust vector with the CG, mitigating this oscillatory behavior.

Conclusions

In this thesis, hardware upgrades and a flight testing campaign have been carried out on an eVTOL drone entirely designed and built at *Politecnico di Milano*. Several limitations, some of which were highlighted in previous theses, necessitated the enhancement of the drone's systems.
From an aerodynamic perspective, both the wing and tail have been resized to match the increased maximum take-off mass of the aircraft. In this process, a structural redesign was also performed, resulting in a much stiffer wing and a lighter tail. This allowed to overcome aeroelastic issues faced during the experimental campaign.
Simultaneously, the limits of forward propulsion was evident: the propellers initially mounted for forward flight were unable to provide sufficient thrust for acceleration. Through research and wind tunnel testing, these propellers were substituted with better performing ones. The wind tunnel data has been utilized to develop a model for accurate thrust estimation, which has been used in the data analysis of the following flight test campaign.
The next step undertaken is a specific flight test campaign outdoor, conducted both in multirotor and in fixed-wing modes. The tests performed encompassed transition and backtransition tests, outdoor hover endurance tests, stall speed determination, drag polar estimation, and specific excess power performance determination.
The transition and backtransition phases have been progressively explored and deep understanding of the aircraft's dynamic during these maneuvers has been achieved. Further exploration of the controller blending, *i.e.,* the airspeed at which both multicopter and fixed-wing controllers output start to blend together, and its effect on the transition is advised given the unexpected action of the elevator that has been encountered.
The fixed wing testing allowed to identify the stall speed of the aircraft, its aerodynamic characteristics and the excess power performance; these key aspects have been compared with the preliminary design values and the numerical predictions obtained in the first stages of the thesis.

Among the results, the most critical one was the parabolic drag polar of the aircraft: data obtained in two different periods of flight testing (namely, July and September) presented some discrepancies in the drag coefficient; at the moment

these discrepancies are attributed to difficulties in the stabilization of the aircraft in the near stall airspeed region. Further testing and comparison are recommended for future work.
Key considerations for future developments include:

- enhancement of the currently employed model for numerical aerodynamic simulation in OpenVSP to achieve a better estimation of the drag characteristics of the aircraft. Optionally, the adoption of more advanced software should be explored;
- upgrading the batteries to 6S models, with a consequent upgrade of the propulsive system, to reduce consumption and enhance overall performance (mainly in multicopter mode);
- improving the flight testing procedure with the addition of custom flight modes in PX4 autopilot to automate the execution of test maneuvers and performing the experiments at a larger airfield to allow for better stabilization during the tests.

Bibliography

[1] N. Battaini. Design and dynamic modeling of a VTOL UAV. Master's thesis, Politecnico di Milano, 2020.

[2] N. Martello. Modelling and integration of an eVTOL UAV. Master's thesis, Politecnico di Milano, 2021.

[3] E. Martinelli. Modelling, control, integration and testing of an eVTOL drone. Master's thesis, Politecnico di Milano, 2022.

[4] Mohammad H. Sadraey. *Aircraft design: a systems engineering approach*. Aerospace Series. John Wiley & Sons, Ltd, 2013.

[5] S. Gudmundsson. *General aviation aircraft design: applied methods and procedures*. Butterworth-Heinemann, 2014.

[6] A. J. Keane, A. Sobester, and J. P. Scanlan. *Small unmanned fixed-wing aircraft design: a practical approach*. Aerospace Series. John Wiley & Sons, Ltd, 2017.

[7] Aeronautics Guide Website. URL: `https://www.aircraftsystemstech.com/p/propeller-aerodynamic-process-airplane.html`.

[8] F. Bus. Fixed-wing UAV performance flight testing. Master's thesis, Politecnico di Milano, 2015.

[9] Accelerate Learning Website. URL: `https://blog.acceleratelearning.com/drone-science-how-quadrotors-work`.

[10] PX4 Autopilot User Guide Website. URL: `https://docs.px4.io/v1.12/en/`.

[11] DJI Website. URL: `https://www.dji.com`.

[12] Wikipedia - Piaggio P.1HH Hammerhead. URL: `https://it.wikipedia.org/wiki/Piaggio_P.1HH_HammerHead`.

[13] S. O. H. Madgwick. An efficient orientation filter for inertial and inertial/magnetic sensor arrays. Tech. rep. University of Bristol, April 2010.

[14] QGroundControl Website. URL: http://qgroundcontrol.com.

[15] Holybro Website. URL: https://holybro.com.

[16] S. Oldani. Comprehensive Flight Testing and Data Analysis for a New Ultralight Aircraft. Master's thesis, Politecnico di Milano, 2017.

[17] MathWorks Website. URL: https://it.mathworks.com.

[18] OpenVSP Website. URL: https://openvsp.org.

[19] MIL F 8785 C. Military Specification: Flying Qualities of Piloted Airplanes. United States Department of Defense, 1980.

[20] XFOIL Website. URL: https://web.mit.edu/drela/Public/web/xfoil/.

[21] HobbyKing Website. URL: https://hobbyking.com.

[22] Gemfan Hobby website. URL: https://www.gemfanhobby.com.

[23] KDE Direct Website. URL: https://www.kdedirect.com.

[24] Arduino Website. URL: https://www.arduino.cc.

[25] APC Propellers Website. URL: https://www.apcprop.com.

[26] UIUC Propeller Data Site Website. URL: https://m-selig.ae.illinois.edu/props/propDB.html.

[27] M. Cerny and C. Breitsamter. Investigation of small-scale propellers under non-axial inflow conditions. *Aerospace Science and Technology*, 106:106048, 2020.

[28] D. E. Gamble. Automated dynamic propeller testing at low Reynolds numbers. Bachelor's thesis, Oklahoma State University, 2009.

[29] Fly-ART Website. URL: http://ascl.daer.polimi.it/ongoing-activities/experimental-activities.

[30] ASCL Website. URL: http://ascl.daer.polimi.it.

[31] OptiTrack - Motion Capture Systems Website. URL: https://optitrack.com.

[32] Motive - Optical motion capture software Website. URL: https://optitrack.com/software/motive/.

[33] Federal Aviation Administration (FAA). Flight test guide for certification of part 23 airplanes, AC23-8C. U.S. Department of Transportation, 2011.

[34] Ralph D. Kimberlin. *Flight Testing of Fixed-Wing Aircraft*. AIAA education series. American Institute of Aeronautics e Astronautics, 2003.

[35] O. Westcott, S. Krishna, R. Entwistle, and M. Ferraro. Aerodynamic performance of aircraft wings with stationary vertical lift propellers. *Aerospace Science and Technology*, 141:108552, 2023.

[36] A. Wang and T. Chan. Estimation of Drag for a QuadPlane Hybrid Unmanned Aerial Vehicle. 2017 AIAA Student Conference Region VII-AU, 2017.

[37] MathWorks - Rational Models. URL: `https://it.mathworks.com/help/curvefit/rational.html`.